

---

[All ETDs from UAB](#)

[UAB Theses & Dissertations](#)

---

2014

## Advancement Of The In-Situ Polymerization Process For Glass Fiber/Nylon-6 Laminates With Nanographite Platelets

Peter William Barfknecht  
*University of Alabama at Birmingham*

Follow this and additional works at: <https://digitalcommons.library.uab.edu/etd-collection>

---

### Recommended Citation

Barfknecht, Peter William, "Advancement Of The In-Situ Polymerization Process For Glass Fiber/Nylon-6 Laminates With Nanographite Platelets" (2014). *All ETDs from UAB*. 1105.  
<https://digitalcommons.library.uab.edu/etd-collection/1105>

This content has been accepted for inclusion by an authorized administrator of the UAB Digital Commons, and is provided as a free open access item. All inquiries regarding this item or the UAB Digital Commons should be directed to the [UAB Libraries Office of Scholarly Communication](#).

ADVANCEMENT OF THE *IN-SITU* POLYMERIZATION PROCESS FOR GLASS  
FIBER/NYLON-6 LAMINATES WITH NANOGRAFITE PLATELETS

by

PETER W. BARFKNECHT

BRIAN S. PILLAY, COMMITTEE CHAIR  
DERRICK R. DEAN  
HAIBIN NING  
UDAY K. VAIDYA  
PETER WALSH  
MARK WEAVER

A DISSERTATION

Submitted to the graduate faculty of The University of Alabama at Birmingham,  
in partial fulfillment of the requirements for the degree of  
Doctor of Philosophy

BIRMINGHAM, ALABAMA

2014

Copyright by  
Peter W. Barfknecht  
2014

ADVANCEMENT OF THE *IN-SITU* POLYMERIZATION PROCESS FOR GLASS  
FIBER/NYLON-6 LAMINATES

PETER W. BARFKNECHT

MATERIALS SCIENCE & ENGINEERING

ABSTRACT

The *in-situ* polymerization process of anionic *polyamide-6* (APA-6) presents the opportunity for a new class of composite materials with excellent performance and wide applicability in the automotive, energy, transportation, and aerospace industries. Despite the inherent advantages of the process, industrial adoption is virtually nonexistent. The following work advances the APA-6 process in three distinct ways. First, the applicability of graphite-based nanoparticles to improve the processability and final performance of the material was evaluated. Nanographite platelets (NGPs) were selectively incorporated into a woven glass fiber/APA-6 laminate via a spraying technique. The polymerization kinetics were unaffected by the presence of NGPs. Mechanical properties were largely unaffected by NGPs except the matrix-dominated laminate short-beam strength which was increased by 25.6 % with a 0.5 wt. % NGP concentration. Second, an alternative chemical process enabling a “single stream” infusion strategy was demonstrated which could greatly improve the automation of the APA-6 process. A soluble diisocyanate initiator (SDI) was synthesized and deposited onto woven glass fabric. A composite laminate was successfully produced using a single, inert solution of monomer and activator. However, an initiator wash-out problem was identified in the process. Surface-initiated polymerization of APA-6 was successfully demonstrated using a specialized silane sizing that contained APA-6 initiation chemistry.

Finally, nanographite oxide platelets (NGOPs) were produced using a planetary ball-milling process from graphite flake and *carbon dioxide*. A kinetic model was applied to optimize the ball-mill design for simultaneous nanographite exfoliation and carboxylation. The ball-mill was shown to be capable of producing NGOPs with lateral dimensions of  $< 1 \mu\text{m}$  and thicknesses  $\ll 1 \mu\text{m}$ . A reaction to functionalize the NGOPs with *4,4'-methylene diphenyl diisocyanate* (MDI) and  *$\epsilon$ -caprolactam* was tested and characterized. Although the presence of diisocyanate-based initiation species was inferred via Fourier-transform infrared spectroscopy (FTIR) and thermogravimetric analysis (TGA), the reaction between the isocyanate and the carboxyl groups was not verified. The FNGPs were unable to initiate surface polymerization of APA-6, possibly due to steric hindrance of the initiator adsorbed to the FNGP surfaces.

Keywords: *in-situ* polymerization, APA-6, multiscale, nanographite, functionalization, processing

## DEDICATION

To my friends and partners who have made this journey unforgettable.

To my family for their unconditional and unlimited love and support.

And to Alejandra whose love and companionship I shall cherish for all time.

## ACKNOWLEDGEMENTS

It is impossible to properly thank everyone who made this work possible. First, I may never fully comprehend the totality of the support and guidance of my advisors through these years, Drs. Brian Pillay, Uday K. Vaidya, and Haibin Ning. You shall always have my respectful gratitude. Thanks to Drs. Derrick Dean and Peter Walsh for your much appreciated contributions to this work. I am indebted for the knowledge and experience you have sent my way. Thanks to Dr. Mark Weaver for his time and attention on this endeavor.

A special thank you goes out to Dr. Gary Gray and Justin Martin from the UAB Department of Chemistry for use of facilities and technical expertise in chemical reactions and analysis. Without their help, this work would not have been possible.

The advice and encouragement of the UAB Engineering faculty and staff has been beyond helpful in these past years, especially: Justin Koch for countless hours of help and advice, Vernon Merchant for helping me fix whatever I had broken, Cynthia Barham for her wisdom and assistance, Andy Grabany for keeping my spirits high, and Balaji Thattai Parthasarathy for his instruction and experience.

All the past and present graduate students and friends who shared the past 5 years with me have given more than can be expressed, especially: Alejandra Constante, Dhruv Bansal, Eric Kerr-Anderson, Dan Kaliberov, Ahmed Hassen, Catlin Cade, John R. Smith, Khongor Jamiyanaa, Ben Geiger-Willis, Ricardo Aristizabal, and all the rest of the MSE students.

The financial assistance from Rounds 7 & 8 of the Alabama EPSCoR program was essential to make this work happen. Additional support from PPG Industries, Inc. was greatly appreciated.

## TABLE OF CONTENTS

	<i>Page</i>
ABSTRACT.....	iii
DEDICATION.....	v
ACKNOWLEDGEMENTS.....	vi
LIST OF TABLES.....	x
LIST OF FIGURES.....	xi
LIST OF ABBREVIATIONS.....	xvii
INTRODUCTION.....	1
Development of the Co-activated Anionic Polyamide-6 Reaction.....	3
Related Research of <i>in-situ</i> polymerized APA-6 Composites.....	5
Kinetics of the APA-6 Reaction.....	7
Review of Literature for Multiscale Enhancement of APA-6.....	9
Research Goals and Organization.....	10
Goal 1: Enhancement of APA-6 Laminates with Nanographite Platelets.....	10
Goal 2: Feasibility of a Single-Stream APA-6 Processes.....	11
Goal 3: Scalable Production of Functionalized Nanographite Platelets.....	11
MATERIALS AND METHODS.....	12
Composite Sample Processing.....	12
Chemical Synthesis and Treatments.....	14
Functionalized Nanographite Production.....	15
Characterization Techniques.....	17
Microscopy.....	17
Nuclear Magnetic Resonance (NMR) <sup>1</sup> H Spectroscopy.....	17
Thermogravimetric Analysis (TGA):.....	18
Differential Scanning Calorimetry (DSC):.....	18
Rheology.....	18
Fourier-transform Infrared Spectroscopy (FTIR):.....	19
X-ray Diffractometry (XRD):.....	19
Thermal Conductivity.....	20
Mechanical Testing.....	20
Three-Point Bend.....	20

Continuous-Excitation Vibration Analysis .....	21
MECHANICAL PERFORMANCE OF GLASS FIBER REINFORCED <i>IN-SITU</i> POLYMERIZED NYLON-6 LAMINATES WITH NANOGRAFITE PLATELETS .	22
SINGLE-STREAM PROCESSING TECHNIQUE FOR <i>IN-SITU</i> POLYMERIZATION OF GLASS FIBER/POLYAMIDE-6 LAMINATES .....	56
FUNCTIONALIZED NANOGRAFITE OXIDE PLATELETS FOR ANIONIC POLYAMIDE-6 INITIATION FROM BALL-MILLED GRAPHITE.....	79
OVERALL CONCLUSIONS.....	118
FUTURE WORK.....	120
GENERAL REFERENCES.....	123

## LIST OF TABLES

<i>Table</i>	<i>Page</i>
<b>MECHANICAL PERFORMANCE OF GLASS FIBER REINFORCED IN-SITU POLYMERIZED NYLON-6 LAMINATES WITH NANOGRAPHITE PLATELETS</b>	
1. A summary of TGA and DSC thermal data for APA-6/NGP cast samples.....	44
<b>SINGLE-STREAM PROCESSING TECHNIQUE FOR <i>IN-SITU</i> POLYMERIZATION OF GLASS FIBER/POLYAMIDE-6 LAMINATES</b>	
1. Useful data to calculate concentrations required for a target APA-6 molecular weight of 53,000 g mol <sup>-1</sup> .....	62
<b>FUNCTIONALIZED NANOGRAPHITE OXIDE PLATELETS FOR ANIONIC POLYAMIDE-6 INITIATION FROM BALL-MILLED GRAPHITE</b>	
1. Geometrical scaling factors from Hertzian contact adapted from Maurice and Courtney <sup>10</sup> .....	95
2. A summary of parameters for comparison between planetary mills used to make nanographite oxide.....	100

## LIST OF FIGURES

<i>Figure</i>	<i>Page</i>
INTRODUCTION	
1. The anion activation reaction of $\epsilon$ -caprolactam with a sodium salt. ....	3
2. The self-initiation reaction is shown above. After the generation of the initiation moiety, the free anion is regenerated. ....	4
3. The initiation and propagation reactions are shown above. (a.) The anion reacts with the initiator. The initial ring-opening reaction transfers the free radical to the newly-opened polymer chain. (b.) The anion reacts with a monomer molecule thereby regenerating the free anion. (c.) The free anion reinitiates the ring-opening reaction. The propagation reactions (b. & c.) continue $n$ times until all available monomer is consumed. ....	4
4. A numerical integration of the kinetic and dynamic viscosity equations using parameters from references <sup>18, 19</sup> & <sup>5</sup> illustrates the extended period of low viscosity known as the “induction time”.....	9
5. The customized resin transfer mold for APA-6.....	14
6. The custom-designed planetary ball-mill is shown with rotation directions marked with arrows.....	16
MECHANICAL PERFORMANCE OF GLASS FIBER REINFORCED IN-SITU POLYMERIZED NYLON-6 LAMINATES WITH NANOGRAFITE PLATELETS	
1. The initiation and propagation reactions are shown above. (a.) The anion reacts with the initiator. The initial ring-opening reaction transfers the free radical to the newly-opened polymer chain. (b.) The anion reacts with a monomer molecule thereby regenerating the free anion. (c.) The free anion re-initiates the ring-opening reaction. The propagation reactions (b. & c.) continue $n$ times until all available monomer is consumed. ....	25
2. A graphical representation of the induction time is shown from a numerical integration of Malkin’s <sup>15, 16</sup> empirical kinetic model and Sibal’s <sup>12</sup> viscosity model for a theoretical APA-6 reaction. ....	27

3. The hypothetical effect of NGP concentration on the induction time. Labels next to the data points indicate the weight fraction concentration of NGP in % $\epsilon$ -caprolactam. The effective catalyst concentration of the NGP was based on the manufacturer-reported atomic oxygen content of 0.5 %. A numerical fit of the data $y=11.0x^2-21.1x+10.4$ ( $R^2=1$ ) shows the slight nonlinearity of adding a third reagent. ....	28
4. (Left) The mixed dry powder samples with NGP concentrations of 0.0, 0.05, 0.1, 1.0 and 2.0 wt. % are shown from left to right. (Right) A detailed view of the 0.05 wt. % sample pellet is shown with the slight inhomogeneity due to coarse grinding of the powder. The images are not to scale. ....	30
5. Complex viscosity $\eta'$ measured during an isothermal time sweep experiment. The induction time was taken as the time at which the viscosity was above 10 Pa-s. ....	31
6. Typical behavior observed by DSC of an isothermal cure of APA-6 with temperature (solid) and exothermic heat flow on a logarithmic scale (dashed). The concentration of NGP in this case was 2.0 wt. %. The induction time was taken as the elapsed time between the end of the 40 °C equilibration and the steep onset of the exothermic heat release (labeled points), which was approximately 9 minutes 40 seconds in this case. ...	32
7. A four sample 8-layer glass fabric preform with weight concentrations with respect to matrix ranging from (back-left) 1.0 %, (back-right) 1.5 %, (front-right) 2.0 %, and (front-left) 0 % .....	34
8. A typical baseband frequency response from continuous excitation vibration analysis of a beam sample. Labels indicate from left to right the harmonic resonant peaks. Each peak is accompanied by an anti-resonant valley at a slightly higher frequency. The final peak near 23000 Hz. is caused by the metal disc threaded into the accelerometer for sample attachment. ....	38
9. A transmitted-light polarization micrograph of a neat APA-6 film (a.) and a film with 0.1 wt. % NGPs (b.). Both samples exhibit a granular spherulite structure. Nanocomposite samples showed a finer spherulite structure, which agrees with literature. <sup>17, 26</sup> .....	40
10. The results of the induction time measurements as measured by rheology $\diamond$ and DSC $\blacksquare$ . The overall average shown as a dashed line was approximately 500 s. ....	41
11. Temperature of 10 % mass loss and maximum loss rate as determine by TGA. ....	43
12. TGA curves from both phases: graphite rich (black), graphite poor (grey), and neat (blue *). ....	43
13. Crystallinity as measured by DSC, adjusted for NGP concentration and normalized by neat APA-6. ....	45
14. Temperatures of melting (black) and cooling (blue) as determined by local maxima of DSC peaks. ....	45

15. The X-ray diffraction pattern obtained from an NGP/APA-6 sample. The two primary peaks correspond to the $\alpha$ -crystal structure of APA-6. <sup>21</sup> A small peak at 26.750 corresponds to the NGP 002 graphite peak. <sup>29</sup> The position of the metastable $\gamma$ -crystal structure of APA-6 is marked with an arrow. No $\gamma$ peak was observed. ....	46
16. A GSED image of a 2.0 wt. % NGP laminate. The sample was cut in the $y$ - $z$ plane and polished. Infusion was uniform as can be observed from the lack of voids in the image.....	47
17. Damping ratio comparison for neat and multiscale 0°/90° laminate samples. ....	48
18. (Left) Short beam shear strength with nominal matrix NGP concentration. (Right) Short beam shear strength with respect to glass fiber volume fraction. The improvement in short-beam strength was determined to be solely dependent on NGP concentration and independent of volume fraction variation caused by thickness variations between the samples.....	49
19. Flexural strength results. Variability tended to decrease with NGP concentration. However, with only 5 samples tested of each, no statistical difference can be concluded. On the right, the flexural strength is shown with respect to volume fraction. ....	50
20. Flexural modulus showed no correlation with NGP concentration. However, when comparing the modulus with calculated fiber volume fraction from Equation (6), the dominant effect of volume fraction is evident. ....	50
21. Thermal conductivity results as measured by the Fox50 instrument.....	51
SINGLE-STREAM PROCESSING TECHNIQUE FOR <i>IN-SITU</i> POLYMERIZATION OF GLASS FIBER/POLYAMIDE-6 LAMINATES	
1. The "co-activated" anionic initiation and propagation reaction steps. An anion reacts with the initiator followed by a ring-opening step. The regenerated anion reacts with the $\epsilon$ -caprolactam monomer and the ring-opening process continues. ....	60
2. The APA-6 initiating silane molecule showing functionality for both glass fiber and APA (CAS: 106996-32-1). ....	61
3. FTIR spectra of the solution over 28 hours of reaction showing a complete disappearance of the NCO peak at wavenumber 2269 $\text{cm}^{-1}$ . A new C=O peak appeared at 1713 $\text{cm}^{-1}$ when the NCO reacted with the $\epsilon$ -caprolactam.....	64
4. (Left) Precipitate formed from the solution by transferring the concentrated products into <i>methanol</i> and filtering. (Right) Precipitate following crystallization from saturated solution in <i>methanol</i> . Images are not to scale .....	65

5. Crystallized SDI (solid) and as-produced SDI (dashed) DSC curves shown offset. The crystalline SDI exhibited a melting peak coinciding with the $\epsilon$ -caprolactam de-blocking reaction which occurred at 184 °C. The as-produced SDI was amorphous and only showed a de-blocking reaction at 185 °C. The typical pre-drying temperature range associated with the APA-6 reaction of 150 – 160 °C was confirmed to be safe for the SDI. ....	66
6. Proton nuclear magnetic resonance (NMR) output of the as-produced precipitate. The integration label below each peak corresponds with the number of protons of each bond type that matches the assumed structure exactly. The sum of the normalized integration adds to 32, which is the number of protons in the SDI structure. Excess unreacted $\epsilon$ -caprolactam, for example, would have offset the lactam integration from 12 protons. Thus, the crystallized product was determined to be mostly pure. ....	67
7. Thermogravimetric determination of minimum temperature required to completely remove organic sizing from test E-glass fabric.....	68
8. Appearance of glass fiber fabric after incorporation of the soluble diisocyanate initiator (SDI). The glass fabric was approximately 12 inches per side. ....	69
9. The as-produced un-sized SDI single-stream panel. Brown line discolorations were caused by sizing residue left over from the fabric pre-treatment. The otherwise non-uniform coloration was likely a result of an inhomogeneous concentration of SDI after infusion. The panel was filled from the center outward. ....	71
10. Remaining mass after soaking in distilled water (open circle). Approximate matrix polymer conversion (filled circle) with respect to position from the centerline of the panel along the 0° direction was calculated assuming a fiber content of 60 wt. %.....	72
11. A DSC curve of a sample from the perimeter of the un-sized SDI panel. A large endothermic peak characteristic of APA-6 is shown near 225 °C. For incomplete polymerization, residual monomer would appear around 68 °C and/or the endothermic melting peak would become broad. The analysis confirms that near the perimeter of the panel, polymerization was successful. ....	73
12. (a.) E-glass fibers are shown in the as-pyrolyzed condition. (b.) The pyrolyzed fiber is shown after MOSCL silanization. (c.) The fibers after surface-initiated polymerization of APA-6 are shown with an area of interest within the white dashed rectangle. (d.) An expanded view of the fiber from within the rectangle in (c.). The fiber surface shows evidence of polymerization occurring at several locations rather than a continuous monolayer of polymer.....	75

FUNCTIONALIZED NANOGRAFPHITE OXIDE PLATELETS FOR ANIONIC  
POLYAMIDE-6 INITIATION FROM BALL-MILLED GRAPHITE

1. A schematic of the primary dimensions required for kinetic modeling of a planetary ball mill. ....	83
---	----

2. The path of the milling sphere while in contact with the milling vial wall is shown as dashed circles. At the point of take-off, the sphere, shown as shaded grey, follows the direct path along the black dashed line until its impact with the vial. ....	84
3. The radial-transverse coordinate axes ( <b>R</b> , <b>T</b> ) and the vial-local coordinate axes ( <b>x</b> , <b>y</b> ) are shown in comparison to the global ( <b>X</b> , <b>Y</b> ) coordinates.....	86
4. The free motion time period (left) and the return motion time period (right), with the sphere travel path shown as dashed circles.....	88
5. A comparison of the path of a single milling sphere for different rotation speed ratios. The left column shows the continuous loop motion that would be observed for the ( <b>R</b> , <b>T</b> ) coordinate system viewer. The right column shows the dynamic path of a single milling sphere in dark grey dashed circles as viewed in the local ( <b>x</b> , <b>y</b> ) coordinate system. The light dashed circles are shown for reference to represent the portion of the vial wall occupied by fixed, apparently-motionless, spheres at a given instant in time.....	90
6. The relevant vectors, coordinates, and angles required to determine the relative velocity of impact between a milling sphere and the vial wall. ....	93
7. The prototypical reaction of a diisocyanate with the NGOP carboxyl functional groups is shown. ....	97
8. Activated monomer and FNGPs are placed into a solution of molten <i>ε-caprolactam</i> . (a.) The isocyanate functional group reacts with a <i>ε-caprolactam</i> molecule producing the initiator species required for APA-6 polymerization. (b.) An activated <i>ε-caprolactam</i> anion reacts with the initiator at the C=O group of the lactam ring. (c.) The lactam ring opens while simultaneously regenerating the anion from another monomer molecule. Step (c.) repeats n-times until the monomer is consumed or the chain is terminated.....	98
9. (left) A section view of the planetary ball mill design. The milling vial is shown inside its casing. A steel counterbalance mass is shown opposite. The two masses are connected at the top with a turnbuckle linkage to prevent significant radial deflection. (right) A photograph of the actual build is shown with the open milling jar on the right. ....	100
10. The as-received GR flake. Approximate platelet size was on the order of 10-100 μm with thicknesses of several μm. ....	105
11. (left) NGOPs after 2 hours of milling. Variation in platelet size is shown with maximum lateral dimensions of approximately 5-10 μm. (right) A detailed view from the marked area shows partially exfoliated platelets with lateral dimensions < 1 μm and thicknesses << 1 μm. ....	106
12. The X-ray diffraction pattern obtained from the NGOPs. The only peak observed was the 002 peak of graphite. No evidence of intercalation of the graphene layers was observed. ....	107

13. The full spectrum integration of NGOP. The dominant peaks at 12.129 and 12.237 ppm represent carboxylic protons. The peak at 7.229 ppm corresponds to the solvent <i>chloroform</i> . The third peak at 5.551 ppm was likely an amide group formed from a side reaction with nitrogen. ....	108
14. Detailed views of the <sup>1</sup> H NMR spectrum carboxyl peaks from (a.) NGOP and (b.) FNGP. The appearance of a third peak at 12.173 ppm could possibly indicate a covalent bond between the isocyanate and carboxyl groups for the FNGPs. Alternately, the diisocyanate initiator could be adsorbed to the FNGP surface and weakly interacting with the carboxyl groups without a covalent bond. ....	109
15. Thermogravimetric analysis of the pure diisocyanate initiator. Two distinct degradation temperatures at 216 °C and 306 °C are shown. The first transition corresponds to the de-blocking in which the <i>ε-caprolactam</i> is released from the NCO groups.....	110
16. The thermal degradation of NGPOs (grey dash-dot) and FNGPs (green dash) are shown in comparison to the source bulk graphite flake (black solid). Two separate degradation temperatures are observed at 201 °C and 314 °C for the FNGPs, which correlate with the degradations of the pure SDI. The main degradation temperature of 385 °C of the NGOPs was not observed explicitly for the functionalized platelets. ....	111
17. The FTIR spectra in total reflectance mode of pure diisocyanate initiator (black) and FNGPs (grey), as 5 point moving averages. Shifted vertically for clarity.....	112
18. The melting endotherm of the control FNGP/APA-6 cast sample. A monomer melt endotherm was not observed, indicating uninhibited polymerization. ....	113
19. (a.) A micrograph of FNGPs dispersed uniformly in activated monomer, after 30 minutes of heating with no evidence of polymerization. The colors are caused by the crystalline structure of <i>ε-caprolactam</i> after cooling. Dark spots are the FNGPs shown with some clumps. (b.) The control sample of FNGPs dispersed in co-activated monomer solution shows a granular spherulite structure with agglomerated FNGPs. No evidence of inhibited polymerization could be observed. ....	114

## LIST OF ABBREVIATIONS

APA-6	Anionic <i>polyamide-6</i>
ATR	Attenuated Total Reflection
BSE	Back-Scatter Electron
CNC	Computer Numerical Control
DP	Degree of Polymerization
DSC	Differential Scanning Calorimetry
FFT	Fast-Fourier Transform
FNGPs	Functionalized Nanographite Platelets
FTIR	Fourier Transform Infrared
GO	Graphene Oxide
GSED	Gaseous Secondary Electron Detector
MOSCL	<i>N</i> -[5-(trimethoxysilyl)-2-aza-1-oxopentyl]caprolactam
MWCNTs	Multi-Wall Carbon Nanotubes

NCO	Nitrogen Carbon Oxygen (Isocyanate)
NGOPs	Nanographite Oxide Platelets
NGPs	Nanographite Platelets
NMR	Nuclear Magnetic Resonance
OH	Oxygen Hydrogen (Hydroxyl)
PA-6	<i>polyamide-6</i>
RRIM	Rapid Reaction Injection Molding
RTM	Resin Transfer Mold
SDI	<i>N,N'-(Methylenedi-p-phenylene)bis[hexahydro-2-oxo-1H-azepine-1-carboxamide]</i>
SE	Secondary Electron
SEM	Scanning Electron Microscopy
TDI	<i>toluene 2,4-diisocyanate</i>
TGA	Thermogravimetric Analysis
TMS	<i>Tetramethylsilane</i>
VARTM	Vacuum-Assisted Resin Transfer Molding
XRD	X-Ray Diffraction

## 1 INTRODUCTION

Fiber-reinforced thermoplastic composites are used extensively by automotive, mass transit and aerospace sectors. Current examples of industrial applications are typically limited to short-fiber composites formed by injection or compression molding processes. To fully utilize the mechanical properties of fiber reinforcements, continuous aligned tapes or other pre-impregnated layers can be stacked and consolidated in an expensive and slow autoclave process. Liquid molded composites of comparable performance with a thermoset matrix require less complicated tooling and process equipment. The liquid infusion technique can be employed for thermoplastics by significantly reducing either the viscosity of the resin or the flow distance. The *in-situ* polymerization technique for composite processing takes advantage of the very low monomer viscosity to enable liquid infusion of thermoplastic matrices. Liquid molding of thermoplastic composites is a novel technology with tremendous potential, yet the technique has only achieved limited industrial adoption. Currently documented industrial applications include continuous carbon fiber reinforced polyamide-12 tapes<sup>1</sup> and glass fiber reinforced polyamide-6 brake pedals.<sup>2</sup> The following key aspects of the *in-situ* polymerization reaction of polyamides represent the topics of greatest need for research to enable the full potential of the process.

Polymerization is critically dependent on reaching the proper temperature, thus heat transfer is an important factor. For thick laminates of thermally insulating fibers,

such as woven glass fabric, enhancement of through-thickness thermal conductivity is a requirement to remove current processing restrictions. One possible strategy is to introduce thermally-conductive nanoparticles into the polyamide matrix to increase the thermal conductivity of the laminate during processing.

Second, simplification of the anionic *polyamide-6* (APA-6) process is required for viable automation and reduced cycle times. The polymerization reaction to produce liquid molded nylon laminates is anionic in nature and presents some challenges. First, moisture from ambient air can contaminate the monomer stream and effectively prevent the reaction. Secondly, since the reaction occurs rapidly, the mixed monomer solutions must be injected and purged quickly, unless an alternative paradigm can be developed. A possible strategy is to separate the chemical species required for polymerization so that a single, inert stream of monomer may be used for infusion.

For a process that takes advantage of multiscale enhancement on an industrial scale, the primary challenge is the assurance of an economically feasible source of the nanoparticles. The process must produce the nanoparticles with the required chemical functionality and in an easily-scalable manner. Mechanical milling of bulk graphite in the presence of reactive gases such as *carbon dioxide* to produce functionalized nanographite platelets is one such process.

These three challenges outlined above represent the three primary research topics covered in this work. The following background information is presented to elaborate on the chemical and physical mechanisms of the APA-6 process.

### Development of the Co-activated Anionic Polyamide-6 Reaction

Anionic polyamide-6 (APA-6) is produced by an anionic polymerization reaction in which the monomer,  $\epsilon$ -caprolactam, undergoes a ring-opening chain polymerization to produce the polymer *polyamide-6* (PA-6) known commonly as nylon-6. The modern “co-activated” reaction includes an activator and an initiator to produce the APA-6 polymer. The reaction was developed from a similar reaction route first patented in the US by Joyce and Ritter in 1941, named here as the “alkaline” polymerization reaction for clarity.<sup>3</sup> The reaction is carried out by combining the  $\epsilon$ -caprolactam monomer with a small quantity of an alkali or alkali earth metal, approximately 0.5 mol. %, and heating at 250 °C for 90 minutes. The anion activation reaction is illustrated in Figure 1. The alkali metal, typically sodium, converts a quantity of the monomer into anions. The anions, enabled by the relatively high temperature, undergo a self-initiation reaction, shown in Figure 2. Once the initiator species is present, the regenerated anion reacts with the initiator as shown in Figure 3. The polymerization process thus becomes self-sustaining and will continue until the  $\epsilon$ -caprolactam monomer is consumed. The rate-limiting reaction step for this process is the self-initiation step of Figure 2.

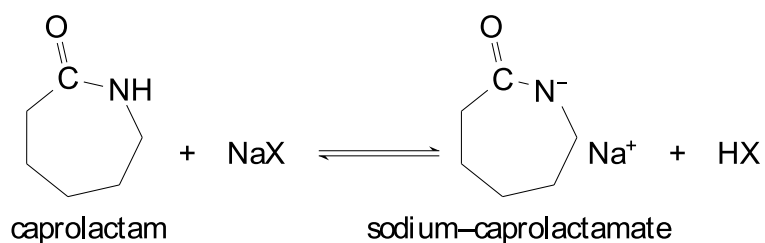


Figure 1. The anion activation reaction of  $\epsilon$ -caprolactam with a sodium salt.

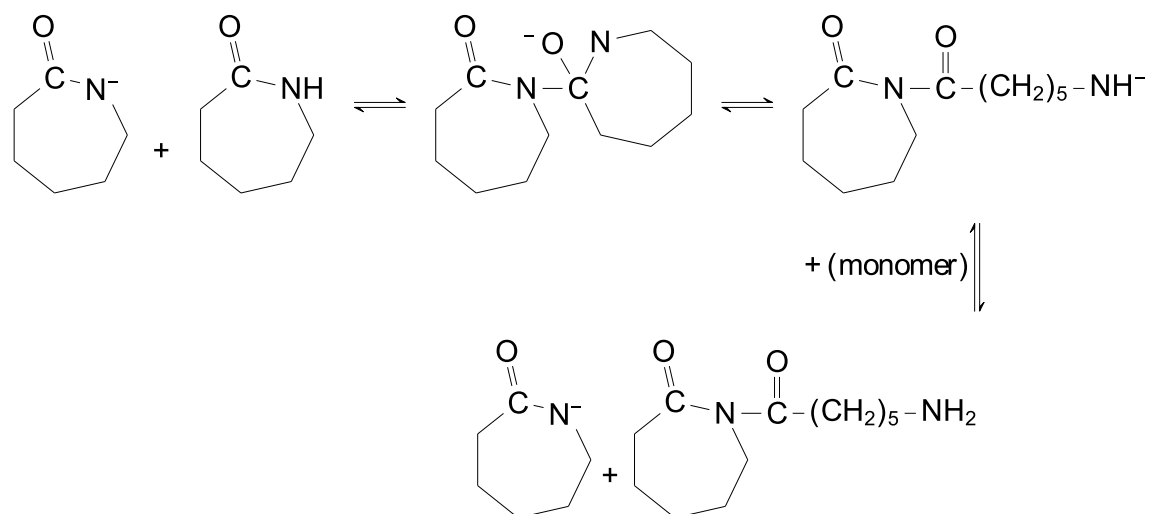


Figure 2. The self-initiation reaction is shown above. After the generation of the initiation moiety, the free anion is regenerated.

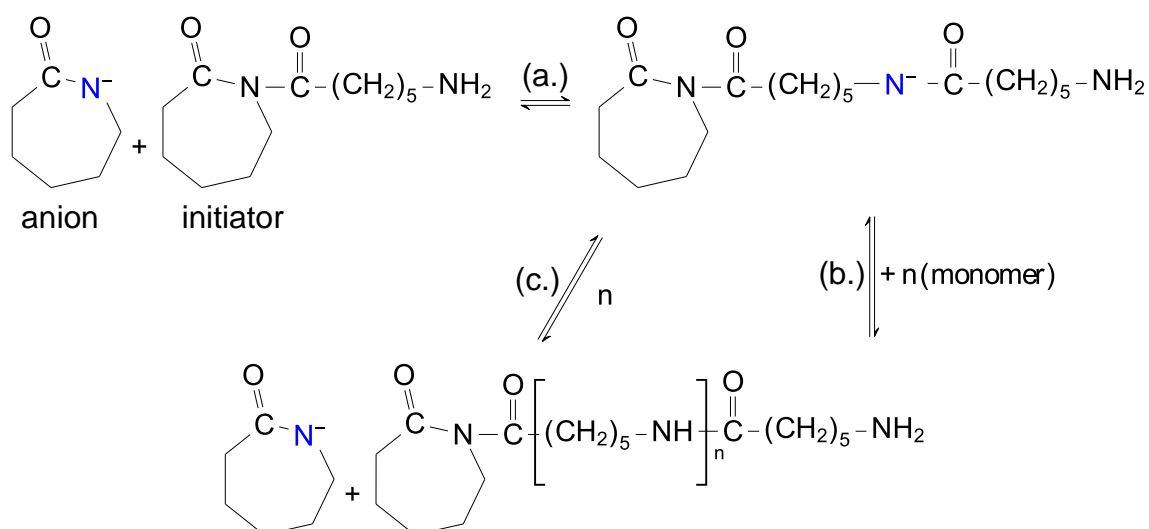


Figure 3. The initiation and propagation reactions are shown above. (a.) The anion reacts with the initiator. The initial ring-opening reaction transfers the free radical to the newly-opened polymer chain. (b.) The anion reacts with a monomer molecule thereby regenerating the free anion. (c.) The free anion reinitiates the ring-opening reaction. The propagation reactions (b. & c.) continue  $n$  times until all available monomer is consumed.

Research on the alkaline polymerization of PA-6 advanced to alternative methods to overcome the limitations of the rate-limiting self-initiation reaction step shown in Figure 2. In 1958, a ‘co-catalytic’ technique was discovered by Šebenda and Králiček as reviewed by Wichterle.<sup>4</sup> The polymerization was carried out similarly to Joyce’s alkaline

method, but since the initiation moiety was introduced from an external source, the reaction could be conducted at much lower temperatures. The polymerization reaction could occur at temperatures well below the final polymer melt temperature and at rates an order of magnitude higher than the self-initiated process. Additionally, since the polymerization reaction was carried out near the maximal crystallization temperatures of PA-6, the final polymer had high crystallinity and a higher polymer conversion of ca. 98 % compared to 95 % for the alkali activated process alone.<sup>5</sup> A wide variety of initiators and monomers with varied reaction rates were applicable to the co-catalytic polymerization reaction as summarized by Hall<sup>6</sup>.

#### Related Research of *in-situ* polymerized APA-6 Composites

The application of the APA-6 process to *in-situ* polymerized composite materials has been sparingly researched since the 1980s. The first noted work was done by Goettler and Neff in 1986.<sup>7</sup> The composites produced were reinforced with glass beads, mats, and unidirectional cross-stitched laminates. The specimens were produced by first pre-heating the reinforcement inside a tool at 190 °C. Second, the molten  $\epsilon$ -caprolactam monomer solution consisting of  $\gamma$ -aminopropyl silane coupling agent, acetyl caprolactam initiator, and sodium caprolactam activator at 130 °C was poured into the mold. Complete polymerization occurred within 10 minutes. Goettler and Neff noted that the solution viscosity was on the order of a few centipoise which facilitated fast infusion. Also, the addition of the coupling agent prevented interface de-wetting thereby increasing toughness and elongation by preventing brittle fracture.

The next notable research effort was done by Otaigbe from 1988-1992.<sup>8-11</sup> The APA-6 process was adapted to rapid reactive injection molding (RRIM). Otaigbe used a center-fill vacuum infusion process to impregnate random glass mats in a matched tool. The use of *γ-aminopropyl silane*, as in Goettler's research, gave maximal composite performance.

A gap in the literature exists until the early 2000s when van Rijswijk<sup>12-15</sup> began work with woven glass fabric and the vacuum-assisted resin transfer molding (VARTM) technique. The goal of this research was to replace glass fiber reinforced thermoset composites for offshore wind turbines. A necessary result of the research was to demonstrate the scalability of the APA-6 infusion process for large structures. The research found that the correct choice of activator could increase the processing scale by lengthening the processing window known as the induction time.<sup>5</sup> Two molten *ε-caprolactam* monomer solutions separately containing the initiator and the “slow” activator were combined immediately prior to infusion. The laminate preform was pre-heated to above the critical polymerization temperature of 150 °C and infused with the mixed monomer solution. The infusion window was extended to approximately 15 minutes, allowing for large flow distances and relatively thick laminates to be produced.

An alternative strategy to demonstrate the scalability of the *in-situ* polymerized APA-6 infusion technique for thin woven-carbon laminates was published by Pillay in 2005.<sup>16</sup> The standard “fast” activator was combined with the initiator and monomer at a relatively low temperature of 100 °C. The VARTM infusion was carried out at 100 °C, below the critical polymerization temperature. Once infused, the laminate was quickly

heated to above 150 °C. Polymerization occurred within 3 minutes, with high polymer conversion and crystallinity.

### Kinetics of the APA-6 Reaction

The polymerization propagation step occurs immediately once the  $\epsilon$ -caprolactam monomer, activator, and initiator are combined and reach a critical temperature of approximately 150 °C. Therefore, at any given time, the monomer solution contains growing polymer chains dissolved in a monomer matrix. For temperatures that are too low, the solubility of the polymer drops and the polymer precipitates from the solution thereby inactivating the process.<sup>4,13</sup> If the temperature is above critical, the reaction proceeds with each polymer chain growing at a near equal rate. The end result is a fairly narrow molecular weight distribution. The initial concentration of initiator species dictates the final average molecular weight, adding to the control of the APA-6 process.<sup>17</sup>

Perhaps the most important processability factor of a resin system for liquid infusion processes is the viscosity of the fluid. To fill the empty volumes around fiber tows and to penetrate within the tow to completely wet-out the fibers, the viscosity must remain low for a sufficient period of time.<sup>5</sup> The dynamic viscosity,  $\eta$  of the solution has been shown by Sibal<sup>5</sup> to follow a logarithmic relationship for fractional conversion  $\beta$  up to 0.7 as expressed:

$$\eta = \eta_0 \ln(\alpha\beta), \quad (1)$$

where  $\alpha$  is an experimentally-determined proportionality constant. The fractional conversion  $\beta$  ranges from 0 to 1 following the mol fraction of mers converted to polymer.

The APA-6 polymerization is autocatalytic in nature. An expression for the instantaneous rate of conversion with respect to time is shown as follows as developed by Malkin:<sup>18, 19</sup>

$$\frac{d\beta}{dt} = \frac{K[I][A]}{[M]_0} (1 - \beta) \left( 1 + \frac{m}{([A][I])^{\frac{1}{2}}} \right) \exp - \frac{E}{R(\beta\Delta T + T_0)}. \quad (2)$$

The initial molar concentration of the initiator and activator [I] and [A], respectively are divided by the monomer concentration [M]<sub>0</sub>. The scaling factor *K* proportionally relates the initiation, propagation, and termination reaction constants and is determined experimentally. The factor *m* accounts for the autocatalytic nature of the reaction due to the gradual segregation of reagents between the growing polymer spherulites. Finally, an Arrhenius expression accounts for the adiabatic heat release during the reaction with the maximum temperature rise of ΔT. The initial temperature of the reaction is T<sub>0</sub>. The polymer propagation activation energy is *E*. A simple numerical integration of Equations (1) and (2) for a hypothetical reaction is illustrated in Figure 4. Factors such as the concentration of reactive species, initial monomer temperature, and the reactivity of the chemical species have a profound effect on the induction time and processability of APA-6 composites.

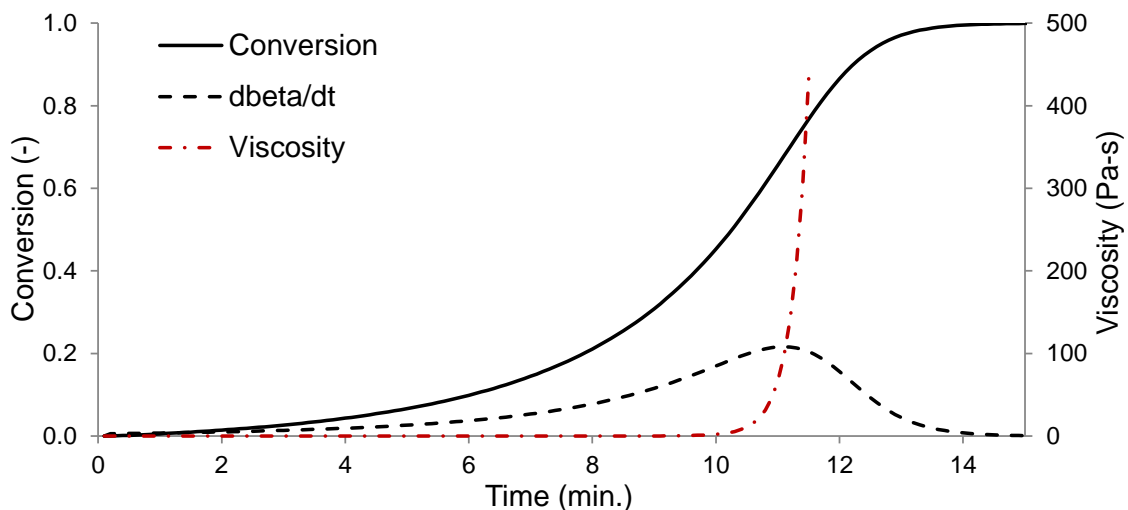


Figure 4. A numerical integration of the kinetic and dynamic viscosity equations using parameters from references <sup>18,19</sup> & <sup>5</sup> illustrates the extended period of low viscosity known as the “induction time”.

#### Review of Literature for Multiscale Enhancement of APA-6

Nanoparticles possess the capability to imbue a composite material with additional properties that may enhance the performance or even the processability of the material. Research involving APA-6 and carbon-based nanoparticles has been limited. Yang, Gao, Li and Andronov in 2007 published a functionalization strategy to effectively disperse multi-wall carbon nanotubes (MWCNTs) into an APA-6 matrix using the anionic *in-situ* polymerization method. The MWCNTs were functionalized to contain hydroxyl groups (OH). Next, *toluene 2,4-diisocyanate* (TDI) was reacted with the OH functionality. Upon introduction into a molten *ε-caprolactam* solution, the TDI reacted with the monomer, producing a common APA-6 initiation moiety. During subsequent polymerization, the growing polymer chains were able to overcome the strong Van der Waals forces which would otherwise cause agglomeration of the MWCNTs.<sup>20</sup> Similar

work was done by Yan and Yang in 2009 showing visibly improved dispersion for bulk cast nano-composite samples.<sup>21</sup>

Literature on graphite-filled APA-6 is almost nonexistent. Frunze in 1971 studied the effect of various forms of carbon black on the spherulite structure and properties of APA-6. Frunze showed that the toughness of the APA-6 improved with the presence of structure-forming nuclei. The mechanical properties of the polymer became more consistent due to the uniformity and refinement of the spherulite structure. A study of the effect of foliated graphite on the crystallization kinetics of APA-6 was done by Weng, Chen, and Wu in 2003 which showed similar heterogeneous nucleation capability of the nanoplatelets.<sup>22</sup> Neither study, however, functionalized the particles prior to processing.

### Research Goals and Organization

Each of the following 3 goals represents one of the 3 manuscripts that comprise this dissertation. Each of the papers represents a method to facilitate the *in-situ* APA-6 composite process for industrial scale-up by alleviating challenges with processing, handling, and production scale.

#### *Goal 1: Enhancement of APA-6 Laminates with Nanographite Platelets*

The APA-6 process design space is bounded in some aspects by thermal constraints. The strong temperature influence on the quality of the final polymer limits the acceptable temperature gradient within the material preform during infusion and polymerization. A thermally-insulating material such as glass fiber further constricts the

range of allowable thickness and pre-infusion temperatures. Through-thickness thermal conductivity has been identified as a key parameter in the processability of thick glass fiber/APA-6 laminates. An attempt was made to increase the through-thickness thermal conductivity of the laminate with the selective addition of nanographite platelets (NGPs) onto the fiber preform prior to infusion. In addition, the possible enhancement of mechanical performance of the laminate was investigated.

### *Goal 2: Feasibility of a Single-Stream APA-6 Processes*

A challenge to the adaptation of the APA-6 process to continuous and automated manufacturing arises from the sensitivity of the reaction to contamination. The prototypical process is carried out by combining two monomer streams separately containing the activator and initiator chemistry. Complicated and expensive metering, mixing, and purging equipment are required to viably process RRIM components with any frequency. By introducing one of the chemical species, the initiator, onto the reinforcement preform, the infusion process may be simplified to a single, continuous stream. This effort investigates two possible techniques, chemical and physical, to locate the initiator species onto the fiber preform.

### *Goal 3: Scalable Production of Functionalized Nanographite Platelets*

The maximum benefit of nanoparticle enhancement for thermoplastic composites is achieved when the particle is fully compatible with the matrix. Chemical functionality of nanoparticles derived from graphite and graphene are readily available. However, to

directly apply nanoparticle research to industrial scales, a viable and scalable process is required. The viability of a process to produce APA-6 functionalized nanographite platelets (FNGPs) from bulk graphite and carbon dioxide using a planetary ball mill was assessed.

## MATERIALS AND METHODS

### Composite Sample Processing

The resin system used for the following work was commercially available. The monomer was anionic polymerization grade  $\epsilon$ -caprolactam supplied as solid flakes with < 0.0015 wt. % moisture content. Two different chemical activator chemistries, *sodium caprolactamate* (Bruggolen® C10) and *caprolactam magnesium bromide* (Nyrin® C1) were also supplied as solid flakes. The initiator, (*hexamethylene-1,6-dicarbamoyl caprolactam*) (Bruggolen® C20P) with an isocyanate (NCO) content of 17 mol. % was supplied as pellets. All commercial APA-6 reactants were purchased from Brüggemann Chemical U.S., Inc.

Plain weave E-glass fabric with an areal density of  $676 \text{ g m}^{-2}$  was provided by PPG Industries Inc. The sizing chemistry was proprietary and specific to APA-6 designated as Hybon-4517. Nanographite platelets (NGPs) N008-100-P-10 were supplied as a dry powder from Angstrom Materials Inc. Chemical composition by weight of the NGPs was  $\geq 99 \%$  C,  $\leq 0.5 \%$  H,  $\leq 0.5 \%$  N,  $\leq 1.4 \%$  O, and  $\leq 0.5 \%$  ash. Platelet geometry was  $\leq 10 \mu\text{m}$  in lateral directions and 50–100 nm in thickness. The average number of stacked graphene layers was 75–150 per platelet. Specific surface area was

$15 \text{ m}^2 \text{ g}^{-1}$ . The solvent used to disperse the NGP was laboratory grade *acetone*, from Acros Organics.

The respective concentrations of commercial activator and initiator used to produce APA-6 were 1.5-7.0 wt. % and 2.5 wt. % on a per weight monomer basis. Handling and processing of the materials was always carried out under dry conditions within a glove box with relative humidity of  $< 10 \%$  or under an atmosphere of dry nitrogen. Cast samples were typically produced either by combining the materials while molten or solid. Polymerization was carried out within sealed glass vials in an air-circulating oven at temperatures above  $150 \text{ }^\circ\text{C}$ . Thin APA-6 films were prepared by grinding the solid reactants into a fine powder and polymerizing between glass slides on a hotplate. The degree of polymerization was nominally 234 based on a  $4.27 \text{ mmol}$ . concentration of NCO. Since the initiator was difunctional, the molecular weight was doubled resulting in a number average molecular weight of  $53,000 \text{ g mol}^{-1}$ .

The infusion and *in-situ* polymerization of glass fiber/APA-6 laminates was done using a custom matched-tool resin transfer mold (RTM) with a center fill port and vacuum assist, shown in Figure 5. The steel platens were each heated with a  $3000 \text{ W}$  embedded serpentine resistance heater. The preforms were dried within the sealed platens under vacuum. The monomer solution was prepared by melting the  $\epsilon$ -*caprolactam* and activator under dry nitrogen and heating to  $120 \text{ }^\circ\text{C}$ . The initiator was added immediately prior to infusion. The resin was first ‘pulled’ into the RTM with vacuum assistance followed by positive injection pressure. Polymerization was carried out at temperatures ca.  $160\text{--}175 \text{ }^\circ\text{C}$ .

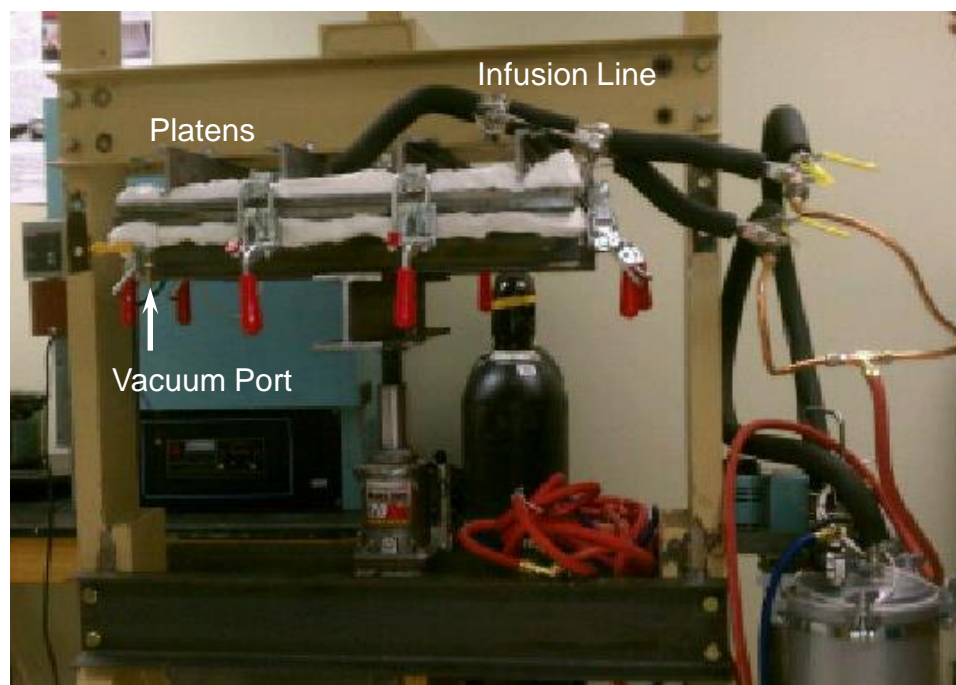


Figure 5. The customized resin transfer mold for APA-6.

Multiscale panels were prepared by first spraying the glass fabric preform with a dispersed solution of NGPs in *acetone* following a procedure adapted from Bansal et al.<sup>23</sup> The required quantity of platelets was dispersed in acetone using an ultrasonic bath. The solution was sprayed using a gravity-fed compressed-air spray gun. Once dried, the laminates were stacked and processed as outlined above.

#### Chemical Synthesis and Treatments

The *4,4'-methylene diphenyl diisocyanate* 98% (MDI) was supplied in solid form from Acros Organics. MDI and *toluene 2,4-diisocyanate* (TDI) are common initiator sources in APA-6 literature. MDI was chosen because it is solid at room temperature for easier and safer handling. The catalyst for functionalizing carboxylated nanoparticles was *magnesium perchlorate*  $Mg(ClO_4)_2$  from Fisher Chemical. The experimental fiber

sizing initiator was *N*-[5-(trimethoxysilyl)-2-aza-1-oxopentyl] caprolactam 95%, CAS 106996-32-1, abbreviated hereafter as (MOSCL), from Gelest Inc.. Lab purity *methanol* was acquired from Fisher Chemical. The solvent used for synthesis of the soluble diisocyanate initiator (SDI) was *toluene* 99.5 %, also from Fisher Chemical. The toluene was dried with 3A molecular sieves prior to use. All other materials were used as-received. Distilled water was produced using a common lab distiller.

The baseline reaction to produce the APA-6 initiator is commonly known as an isocyanate blocking reaction. The isocyanate NCO group is temporarily reacted with a secondary chemical to inactivate its reactivity until needed as is typical for polyurethane production.<sup>24</sup> The MDI was dispersed in anhydrous *toluene* and reacted with excess  $\epsilon$ -*caprolactam* at 80 °C under dry nitrogen until the NCO groups were consumed. For a reaction to chemically functionalize graphite oxide, for example, the isocyanate was first allowed to react with the nanoplatelets with the help of the *magnesium perchlorate* catalyst. Then, the remaining NCO groups were blocked with  $\epsilon$ -*caprolactam*. In both cases, the blocked isocyanate is chemically stable in ambient conditions and could be used directly as an APA-6 initiator.

### Functionalized Nanographite Production

Natural flake graphite (85-98 % carbon) CAS#7782-42-5 was supplied by Asbury Carbons. Standard grade dry ice was used to produce the *carbon dioxide* atmosphere within the milling vial. Concentrated *nitric acid* (65 % w/w) and laboratory grade *methanol* were supplied by Fisher Chemical.

A custom planetary ball-mill, shown in Figure 6, was constructed following design considerations outlined by Maurice et al.<sup>25</sup>, Lu et al.<sup>26</sup> and Chattopadhyay et al.<sup>27</sup> A procedure outlined by Jeon et al. to produce nanographite oxide platelets (NGOPs) was adapted for the work.<sup>28</sup> The stainless steel milling jar was loaded with 2.0 g of bulk graphite flakes, 50 hardened stainless steel spheres (9 mm diameter), and approximately 20 g of dry ice. The internal pressure of the jar was maintained at 1720 kPa (250 psi) using a spring-actuated pressure relief valve. The contents were milled at a sun disc speed of  $\Omega=600$  rpm for 6 hours.

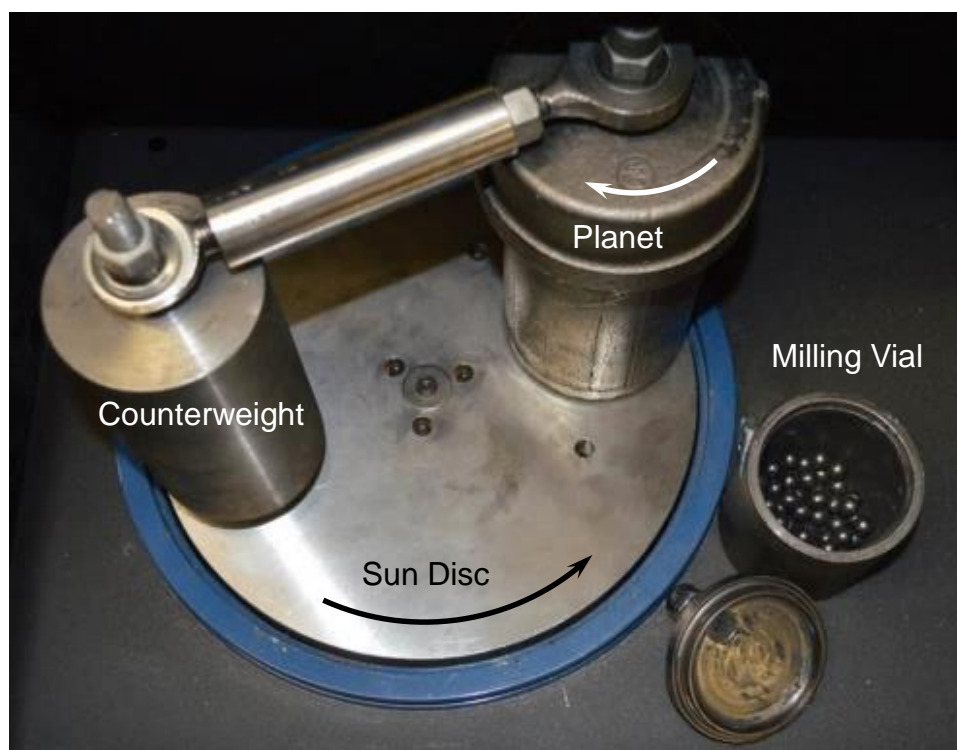


Figure 6. The custom-designed planetary ball-mill is shown with rotation directions marked with arrows.

The as-milled NGOPs contained iron contamination from the milling process. To remove the iron, the NGOPs were dispersed in 150 ml of *methanol* and 50 ml of concentrated 65 % w/w *nitric acid*. The acidified NGOPs were then washed with distilled water and dried in a furnace at 300 °C.

## Characterization Techniques

### *Microscopy*

Scanning electron microscopy (SEM) images were acquired with a Quanta FEG 650 SEM. Detailed morphological images such as platelet topography at high magnification were acquired using the secondary electron (SE) detector under high vacuum. For interface characteristics, such as the surface of a functionalized glass fiber, a gaseous secondary electron detector (GSED) was used at low pressures of water vapor. Observations of atomic elements present, such as metallic particle contamination of the NGOPs were done using a back-scatter electron detector (BSE).

Thin polymer film samples were characterized using a Zeiss Axoplan 2 microscope. The APA-6 spherulite morphology was observed using the through-transmission cross-polarized technique.

### *Nuclear Magnetic Resonance (NMR) <sup>1</sup>H Spectroscopy*

<sup>1</sup>H NMR spectra were recorded on a Bruker DRX-400 NMR spectrometer at room temperature, 300 K. The NMR spectra were used to measure the molar ratios of protons within a chemical species and the chemical bonds associated with each. For example, the chemical structure of the soluble *diisocyanate* initiator (SDI) was confirmed against the hypothesized structure.

### *Thermogravimetric Analysis (TGA):*

A TA Instruments Thermogravimetric Analyzer (TGA 2950) was used to determine the thermal stability of a sample material. For a typical experiment, a sample was heated at  $20\text{ }^{\circ}\text{C min}^{-1}$  under nitrogen. The sample mass was recorded with respect to temperature. Parameters such as degradation onset temperatures and residual mass were used to determine the chemical substances and quantities present in the sample.

### *Differential Scanning Calorimetry (DSC):*

A TA Instruments DSC equipped with a TA Q100 Controller and refrigerated cooling system was used for thermal property measurement of various samples. The technique measures heat flow into and out of a sample during thermal events such as chemical reactions and phase transformations. The induction time of APA-6 was measured by quickly heating a co-activated monomer solution to  $150\text{ }^{\circ}\text{C}$  and measuring the elapsed time before a sensible exothermic reaction. Other thermal properties such as the crystallinity of the APA-6 or the de-blocking temperature of SDI were determined by ramping the temperature of the sample at a rate of  $10\text{ }^{\circ}\text{C min}^{-1}$  and observing the heat absorbed by the sample. The standard heat of melting  $\Delta H_m$  for calculation of APA-6 crystallinity was  $230\text{ J g}^{-1}$  from the ATHAS database.<sup>29</sup>

### *Rheology*

Rheological measurements were made using a TA Instruments Advanced Rheometer and a TA AR2000 Controller. The viscosity of APA-6 was measured during

isothermal polymerization. Pre-mixed powder pellet samples were placed between flat aluminum plates. The sample was heated to 150 °C and subjected to rotational oscillations at constant temperature and frequency in a time sweep experiment. The force transmitted through the sample to a load sensor was used to calculate the storage modulus  $\eta'$ . The induction time was recorded as the elapsed time from the beginning of the time sweep until samples reached a measured complex viscosity of greater than 10 Pa s.

#### *Fourier-transform Infrared Spectroscopy (FTIR):*

Functional group analysis was done using a Bruker ALPHA FTIR Spectrometer in attenuated total reflectance (ATR) mode. The output spectrum displays peaks with respect to incident infrared light wavelength. The peaks correspond to vibrational modes of various chemical bonds that were used to identify chemical species present within a sample.

#### *X-ray Diffractometry (XRD):*

X-ray diffraction analysis was performed on a Siemens D500 PC Diffraction System. The source was Cu  $k_{\alpha}$  with a wavelength  $\lambda=1.54056$  nm. Crystallographic information of the APA-6 polymer and NGPs was determined by peaks in the x-ray intensity versus  $2\theta$  angle, corresponding to the satisfaction of Bragg's law of x-ray diffraction.<sup>30</sup>

### *Thermal Conductivity*

Circular discs with a diameter of 47 mm were cut from the APA-6 laminate samples using a computer numeric control (CNC) mill program. Thermal conductivity in the through-thickness direction was then measured using a LaserComp Fox50 heat flow meter. Instrument air pressure was 60 psi. A thermal gradient of 20 °C was maintained for a given temperature set point. For example, the top and bottom temperatures were maintained at 70 °C and 90 °C to obtain the sample thermal conductivity at 80 °C. Several set points were measured to give the through-thickness thermal conductivity for a temperature range from 30–100 °C.

### **Mechanical Testing**

#### *Three-Point Bend*

An Instron SATEC T series load frame was used for mechanical tests. Force was recorded using an Interface Manufacturing load cell Model 1210AF-5K with a capacity of 22.2 kN (5 kip). Flexure tests were performed on samples following ASTM D7264M-07 to evaluate the combined fiber and matrix performance.<sup>31</sup> Load was applied at a crosshead rate of 5 mm min<sup>-1</sup>. Short beam shear tests were performed according to ASTM D2344 to concentrate analysis on the performance of the matrix due to the increased influence of shear stress in the sample.<sup>32</sup> Cross-head speed was 1 mm min<sup>-1</sup>.

*Continuous-Excitation Vibration Analysis*

Measurement of the vibration damping response of samples was done in a free-free boundary condition. The samples were mounted on their geometric center with beeswax to a B&K Type 8001 accelerometer, which served as the input and output sensor simultaneously. A random input signal was induced by a B&K 4809 mini shaker and B&K Type 2706 amplifier with a range of 0–25.6 kHz. Vibration response was recorded with a B&K 3560-B-140 signal analyzer and translated into a frequency response using fast Fourier transformation (FFT). The measured parameter of the sample was the damping ratio  $\zeta$  determined by the -3 dB half-power bandwidth method.<sup>33</sup>

MECHANICAL PERFORMANCE OF GLASS FIBER REINFORCED *IN-SITU*  
POLYMERIZED NYLON-6 LAMINATES WITH NANOGRAFITE PLATELETS

by

PETER W. BARFKNECHT, BRIAN (SELVUM) PILLAY, AND UDAY K. VAIDYA

In preparation for *Journal of Thermoplastic Composite Materials*

Format adapted for dissertation

## ABSTRACT

Anionic polyamide-6 (APA-6) is a thermoplastic polymer that can be polymerized *in-situ* to produce composite laminates with excellent mechanical properties. One challenge to the application of the APA-6 process for liquid infusion of composites such as the rapid reaction injection molding (RRIM) process is the thermal conduction of the laminate. This study makes a first attempt to improve the thermal conductivity of woven glass fiber/APA-6 laminates through the introduction of nanographite platelets (NGPs). Additionally, the effect of the NGPs on the reaction kinetics, polymer thermal properties, and mechanical performance of the laminate are evaluated. A direct rheological method and an indirect thermal method to measure the induction time of APA-6 polymerization were demonstrated. No change in induction time was observed for the NGP concentration range from 0–2.0 wt. %. The results were in concurrence with a simple kinetic model. Cast NGP composite samples settled into distinct graphite-rich and graphite-poor phases. The graphite rich phase contained approximately 9 wt. % content of NGPs regardless of the initial concentration. No change in thermal properties was observed between the nanocomposite and neat samples. Spherulite refinement was observed for NGP nanocomposite films in concurrence with literature. Short-beam strength of the composite was enhanced by 25.6 % for a concentration of 0.5 wt. % NGPs. Both flexural performance and vibration damping were unaffected by NGP concentration. Through-thickness thermal conductivity showed no change until an NGP concentration of 2.0 wt. %. Additional study is required to determine the minimum concentration required for NGPs to form a continuous thermal conduction path in the thickness direction.

## INTRODUCTION

Continuous fiber reinforced thermoplastics are part of a growing sector of composites research with direct applicability to industry needs. With continuous reinforcement, mechanical performance is maximized. Continuous thermoplastic composites are also recyclable as a precursor material for processes such as extrusion compression molding.<sup>1</sup> The disadvantage of the majority of continuous fiber reinforced thermoplastics is that conventional processing techniques require several steps: (a) raw material production of the fiber (b) polymerization of the matrix (c) impregnation of precursor materials (d) cutting and placing of preforms, and (e) final melt processing/forming via hot stamping or autoclave consolidation. With *in-situ* polymerization, dry fibers and monomer are combined in a near-net shape configuration that greatly reduces the number of production steps. Only a handful of thermoplastics such as polybutylene terephthalate PBT<sup>2</sup> or anionic polymerized polyamides<sup>3-7</sup> have been considered as suitable candidates for *in-situ* infusion and polymerization of continuous fiber composites. With any emerging technology, several challenges must be overcome before the full potential is reached.

The co-activated anionic polymerization of polyamides is outlined as follows: the monomer solution consists of a lactam monomer, an activator to produce the anion free radical, and an initiator species to begin the anionic ring-opening polymerization process. A typical polymerization scheme is shown in Figure 1. The temperature and reactivity of the monomer solution must be optimized to give the appropriate processing window, known as the induction time.<sup>8</sup> For temperatures approaching the melting temperature of the final polymer, polymerization occurs rapidly. For temperatures below a critical

temperature, the polymerization reaction is inhibited resulting in incomplete polymerization.<sup>8,9</sup> Thus, the acceptable temperature gradients within the laminate caused by poor conductivity can be a limiting factor.<sup>10</sup> The chemical reactivity of the activator and initiator species also influences the length of the induction time.<sup>11-13</sup>

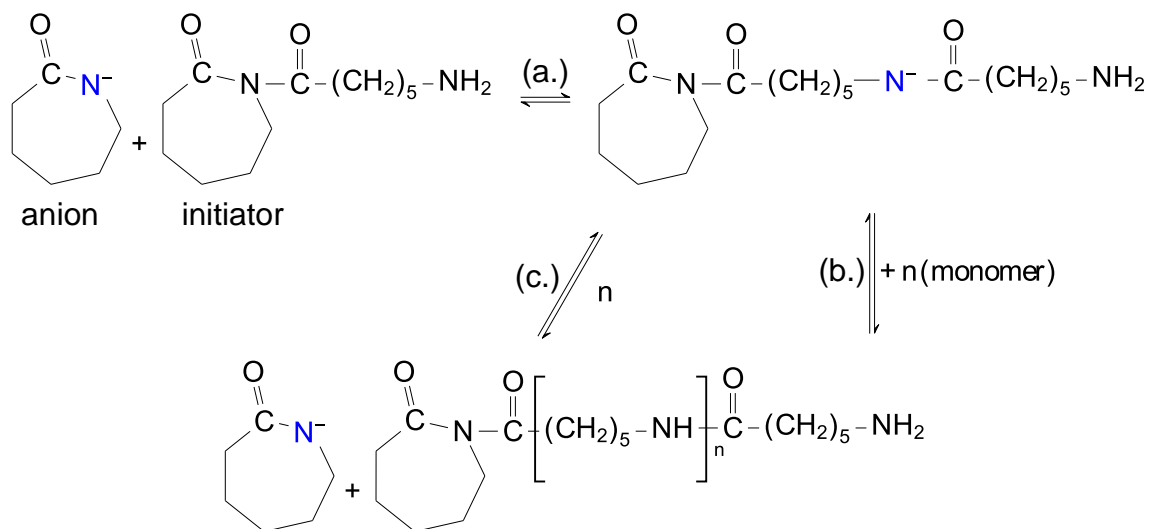


Figure 1. The initiation and propagation reactions are shown above. (a.) The anion reacts with the initiator. The initial ring-opening reaction transfers the free radical to the newly-opened polymer chain. (b.) The anion reacts with a monomer molecule thereby regenerating the free anion. (c.) The free anion re-initiates the ring-opening reaction. The propagation reactions (b. & c.) continue  $n$  times until all available monomer is consumed.

This work focuses on enhancing the thermal conductivity of the laminate through the addition of nanographite platelets (NGPs) and thereby improving the polymerization process capabilities of APA-6. The upper bound of in-plane thermal conductivity is on the order of  $5000 \text{ W m}^{-1} \text{ K}^{-1}$  for single-layer graphene<sup>14</sup> which is approximately 4 orders of magnitude higher than the baseline through-thickness thermal conductivity of glass fiber/APA-6 laminates evaluated in the study. The purpose of the work was to test the hypothesis that a concentration close to the percolation limit of NGP dispersed in the APA-6 matrix of the laminate would provide a noticeable improvement in thermal

conductivity. Additionally, the effect of NGP on the matrix polymer properties was evaluated.

### PHYSICAL SOURCE OF THE INDUCTION TIME

The induction time of the APA-6 reaction is the period of low monomer viscosity suitable for infusion. The end of the induction time is characterized by an exothermic heat release and a sudden increase in viscosity. The polymerization reaction is also autocatalytic in nature. An expression for the instantaneous rate of conversion  $d\beta/dt$  was developed by Malkin<sup>15, 16</sup> as shown in Equation (1).

$$\frac{d\beta}{dt} = \frac{K[I][A]}{[M]_0} (1 - \beta) \left( 1 + \frac{m}{([A][I])^{1/2}} \right) \exp - \frac{E}{R(\beta\Delta T_A + T_0)} \quad (1)$$

Under adiabatic conditions, the instantaneous conversion rate is a function of initial species concentrations of monomer, activator, and initiator:  $[M]_0$ ,  $[A]$  and  $[I]$ , respectively. A pre-exponential factor  $K$ , a self-catalytic factor  $m$ , and the activation energy of polymer propagation  $E$  are obtained experimentally. Finally, an Arrhenius expression including the universal gas constant  $R$ , accounts for the adiabatic temperature rise of the solution from the initial temperature  $T_0$ . The total adiabatic temperature rise at completion of the reaction  $\beta = 1$  is  $\Delta T_A$ . An empirical expression of the monomer solution viscosity  $\eta$  was presented by Sibal<sup>12</sup> as shown in Equation (2). As the dissolved polymer chains grow in length, the initial monomer solution viscosity  $\eta_0$  increases logarithmically with polymer conversion  $\beta$  scaled by an experimental dimensionless parameter  $\alpha \approx 17.5$ .

$$\eta/\eta_0 = \ln(\alpha\beta) \quad (2)$$

A combination of the instantaneous conversion rate and the solution viscosity is shown in Figure 2. The expression was numerically integrated over time steps of 6 s. The induction time shown in the figure is approximately 10 minutes. Parameters for the reaction,  $K = 7.7 \times 10^9 \text{ mol l}^{-1} \text{ min}^{-1}$ ,  $m = 0.93 \text{ mol l}^{-1}$ , and  $E = 16.8 \text{ kcal mol}^{-1}$  were taken from Malkin<sup>16</sup> for *N-acetylcaprolactam* initiator and *sodium-caprolactam* activator. Typical molar concentrations of  $0.0134 \text{ mol l}^{-1}$  and  $0.0267 \text{ mol l}^{-1}$  for the initiator and activator, respectively, were used. The initial temperature of the reaction was  $150 \text{ }^\circ\text{C}$ .

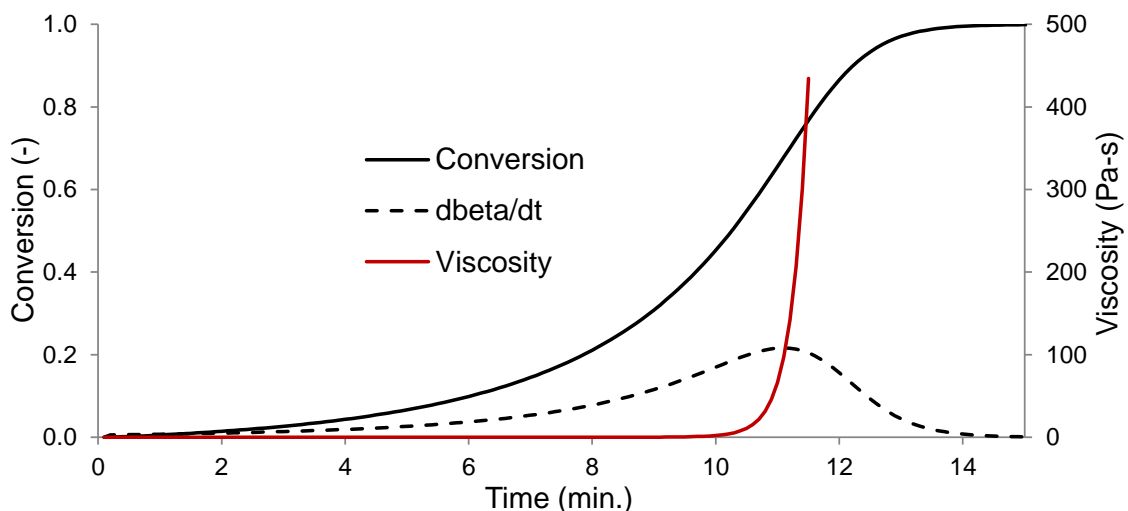


Figure 2. A graphical representation of the induction time is shown from a numerical integration of Malkin's<sup>15, 16</sup> empirical kinetic model and Sibal's<sup>12</sup> viscosity model for a theoretical APA-6 reaction.

### KINETIC EFFECT OF CARBON NANOPARTICLES

Carbon black has been shown to be chemically inert for the APA-6 reaction except as a spherulite nucleation site.<sup>17</sup> For the current study, it was hypothesized that the oxygen defects of the NGPs could provide an additional reactive factor as either an initiator or activator. Equation (1) would be modified to include a third reagent concentration [X] as is shown in Equation (3).

$$\frac{d\beta}{dt} = \frac{K[I][X][A]}{[M]_0} (1 - \beta) \left( 1 + \frac{m}{([A][X][I])^{1/2}} \right) \exp - \frac{E}{R(\beta\Delta T_A + T_0)} \quad (3)$$

A plot of induction time with NGP concentration is shown in Figure 3, assuming the induction time ended at a solution viscosity greater than 10 Pa-s. The expression assumed the NGP had no effect on other reaction constants such as the pre-exponential factor  $K$  or the activation energy  $E$ . Figure 3 shows that even with NGP weight content of 10 wt. % and with an assumed chemical activity equivalent to the other reagents, a negligible effect on the induction time was expected. For nanoparticles with higher oxygen defect content such as graphite oxide, or with specialized chemical functionality such as graphite oxide functionalized with an isocyanate<sup>18, 19</sup>, the effect on induction time could be more pronounced.

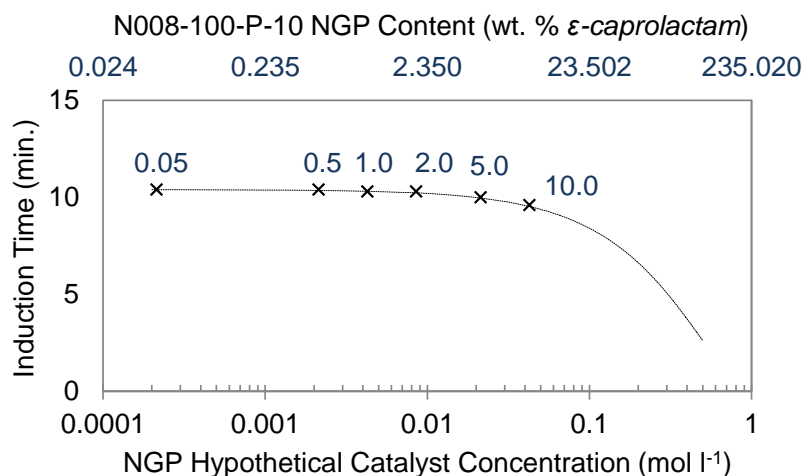


Figure 3. The hypothetical effect of NGP concentration on the induction time. Labels next to the data points indicate the weight fraction concentration of NGP in %  $\epsilon$ -caprolactam. The effective catalyst concentration of the NGP was based on the manufacturer-reported atomic oxygen content of 0.5 %. A numerical fit of the data  $y=11.0x^2-21.1x+10.4$  ( $R^2=1$ ) shows the slight nonlinearity of adding a third reagent.

## MATERIALS

Plain weave E-glass fabric with an areal density of  $676 \text{ g m}^{-2}$  was provided by PPG Industries Inc. The sizing chemistry was a proprietary formula specific to anionic polymerization of nylon-6 and was designated as Hybon-4517®. The anhydrous anionic polymerization grade monomer, *ε-caprolactam*, was received in 25 kg foil-lined bags from Brüggemann Chemical. The activator was *caprolactam magnesium bromide* (Nyrin® C1) from the same source. The initiator was (*hexamethylene-1,6-dicarbamoylcaprolactam*) (Bruggolen® C20), also from the same supplier. The polar nanographite platelets N008-100-P-10 were supplied as a dry powder from Angstrom Materials Inc. Chemical composition by weight of the NGPs was  $\geq 99 \%$  C,  $\leq 0.5 \%$  H,  $\leq 0.5 \%$  N,  $\leq 1.4 \%$  O, and  $\leq 0.5 \%$  ash. Platelet geometry was  $\leq 10 \mu\text{m}$  in lateral directions and 50–100 nm in thickness. The average number of stacked graphene layers was 75–150 per platelet. Specific surface area was  $15 \text{ m}^2 \text{ g}^{-1}$ . The solvent used to disperse the NGP was laboratory grade *acetone*, from Acros Organics.

## EXPERIMENTAL MEASUREMENT OF THE INDUCTION TIME

The induction time as a function of NGP concentration was measured both directly through rheological measurement of viscosity, and indirectly through differential scanning calorimetry (DSC). Dry *ε-caprolactam* flakes, Bruggolen C1 (7.0 wt. %) activator and Bruggolen C20 (2.5 wt. %) initiator were combined in a dry glove box at proportions relative to the monomer. The glove box was maintained at  $< 10 \%$  relative humidity using silica gel desiccant. The dry flakes and pellets were ground using a mortar and pestle. Portions of the mixture were added to glass vials. The appropriate content of NGP was added to each vial with respect to the mixture mass to obtain

samples at concentrations of 0.0, 0.05, 0.1, 1.0, and 2.0 wt. % as shown in Figure 4. The powders were mixed inside the sealed glass vials using a vortex mixer. Next, discs with a diameter of 18 mm and 2 – 4 mm in thickness of each concentration as shown in Figure 4 were prepared using a pellet press die. Due to slight inhomogeneity of the disc samples, the remaining powder was further homogenized by heating the sealed glass vials in a convection oven at 100 °C until the contents were completely molten. Then, the samples were promptly removed and vigorously mixed using the vortex mixer until the vial contents solidified. The homogenized samples were then used for the DSC analysis.



Figure 4. (Left) The mixed dry powder samples with NGP concentrations of 0.0, 0.05, 0.1, 1.0 and 2.0 wt. % are shown from left to right. (Right) A detailed view of the 0.05 wt. % sample pellet is shown with the slight inhomogeneity due to coarse grinding of the powder. The images are not to scale.

#### DIRECT VISCOSITY MEASUREMENT OF INDUCTION TIME

Rheological measurement of the induction time was done using a TA Instruments Advanced Rheometer and a TA AR2000 Controller. Flat, round aluminum plates 25 mm in diameter were used. The instrument was continuously purged with dry nitrogen gas to prevent contamination. The heater was set to 150 °C, and the instrument was allowed to stabilize in temperature. A portion of a sample pellet was placed between the plates. The gap distance was immediately closed to 200  $\mu\text{m}$ . The experiment procedure was an

isothermal time sweep. The plates were oscillated at a frequency of  $1.0 \text{ rad. s}^{-1}$  and at 0.5 % strain. The total time was recorded between sample insertion and the time at which the complex viscosity  $\eta'$  reached 10 Pa-s. A plot of viscosity over time as measured by the instrument is shown in Figure 5.

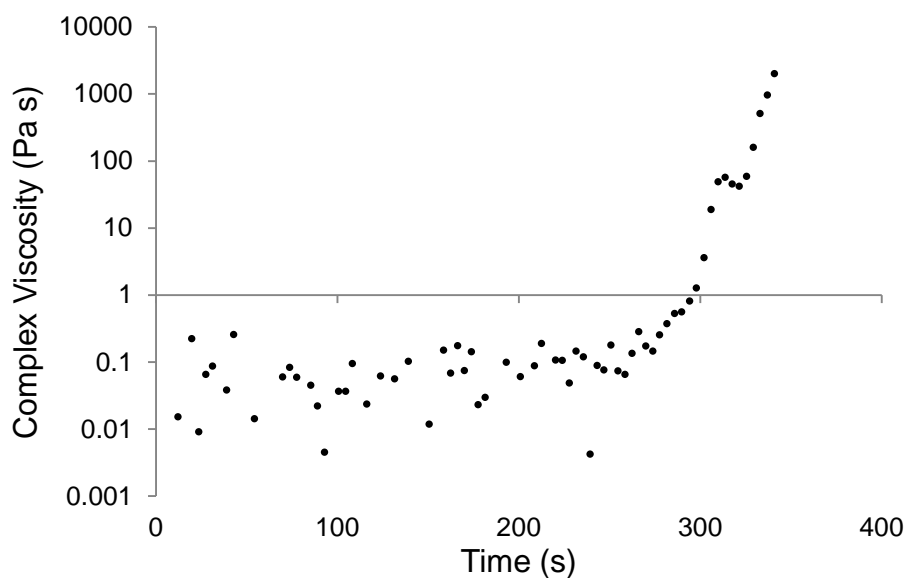


Figure 5. Complex viscosity  $\eta'$  measured during an isothermal time sweep experiment. The induction time was taken as the time at which the viscosity was above 10 Pa-s.

#### INDIRECT THERMAL MEASUREMENT OF INDUCTION TIME

DSC measurement of the induction time was done using a TA Instruments DSC equipped with a TA Q100 Controller and refrigerated cooling system. A small sample of homogenized monomer was placed into an aluminum hermetic pan and sealed while inside the dry glove box. The DSC procedure was an instantaneous jump in temperature to  $150 \text{ }^\circ\text{C}$  after equilibrating at  $40 \text{ }^\circ\text{C}$ . The time until a sensible exothermic reaction was observed was recorded as the induction time. Typical temperature and heat flow profiles are overlaid in Figure 6, clearly illustrating the sudden onset of polymerization shown as the steep rise in exothermic heat flow.

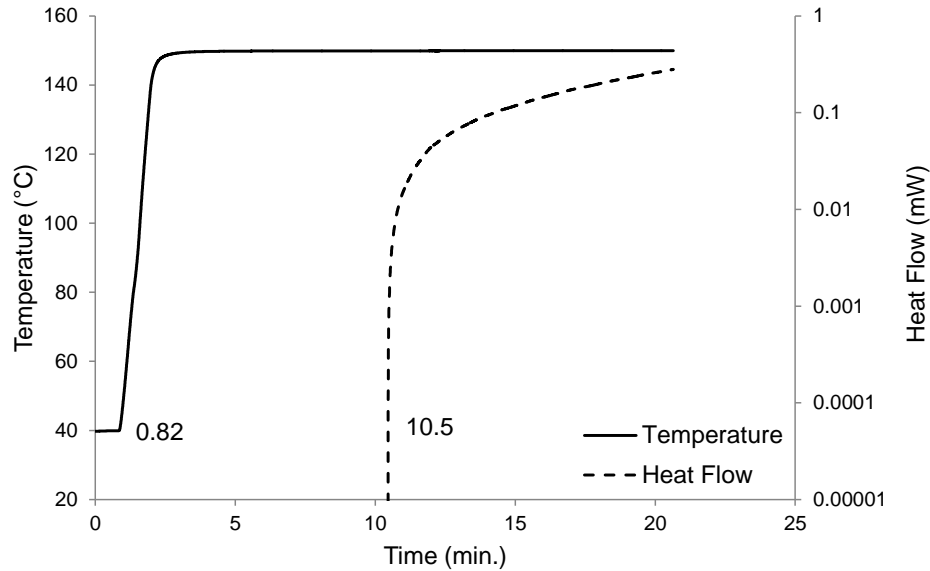


Figure 6. Typical behavior observed by DSC of an isothermal cure of APA-6 with temperature (solid) and exothermic heat flow on a logarithmic scale (dashed). The concentration of NGP in this case was 2.0 wt. %. The induction time was taken as the elapsed time between the end of the 40 °C equilibration and the steep onset of the exothermic heat release (labeled points), which was approximately 9 minutes 40 seconds in this case.

## PROCESSING OF MULTISCALE APA-6 LAMINATES

### SPRAYING OF NGPS

Even distribution of NGP was achieved by spraying platelets dispersed in a solvent onto dry fabric layers prior to infusion. Typical solvents for dispersing carbon nanoparticles such as *N,N*-dimethylformamide require long drying times and are toxic.<sup>20</sup> The polar nature of the nanoplatelets allowed for temporary dispersion in common *acetone*. The required amount of NGP was calculated as a weight fraction of the final composite APA-6 matrix assuming a target fiber weight fraction of 70 %.

$$m_{NGP} = \frac{1 - W_f}{W_f} m_{glass} (C_{NGP})_{matrix} \quad (4)$$

For example, if the mass of the glass layers  $m_{glass}$  was 1000 g and the desired weight concentration  $C_{NGP}$  of NGP with respect to the matrix was 1 %, assuming the

weight fraction of glass  $W_f$  was 0.7, 4.286 g of NGP in total was evenly distributed over all of the layers. A typical spraying procedure was as follows: 0.268 g of NGP was combined with 100 ml of acetone in a glass beaker and dispersed using a Cole-Parmer 8852 ultrasonic cleaner for 20 minutes. Glass fabric was sprayed with the solution on one side using a gravity-fed spray gun and compressed air. The layer was dried in air for 20 minutes until the next solution was prepared. The layer was then turned over and sprayed with another quantity of solution. Subsequent fabric layers were laid upon the previous and sprayed evenly on one side, dried, and turned over to spray the opposite side in a similar fashion. The layers were placed on top of the previously sprayed layers in order to capture platelets that had passed through the inter-tow spaces. Variability of concentration as well as some loss of NGP was unavoidable. Visible uniformity and careful spraying technique were the only means of quality control of the process. Further research could be done to improve uniformity.

#### INFUSION AND POLYMERIZATION

To minimize possibility of processing variability from one processing run to another, neat and multiscale sample panels were processed simultaneously. A typical layup for an 8 layer preform was done as shown in Figure 7. Infusion was from the top-center of the panel. Vacuum was applied on one corner from below with space to provide a vacuum path surrounding the entire preform.

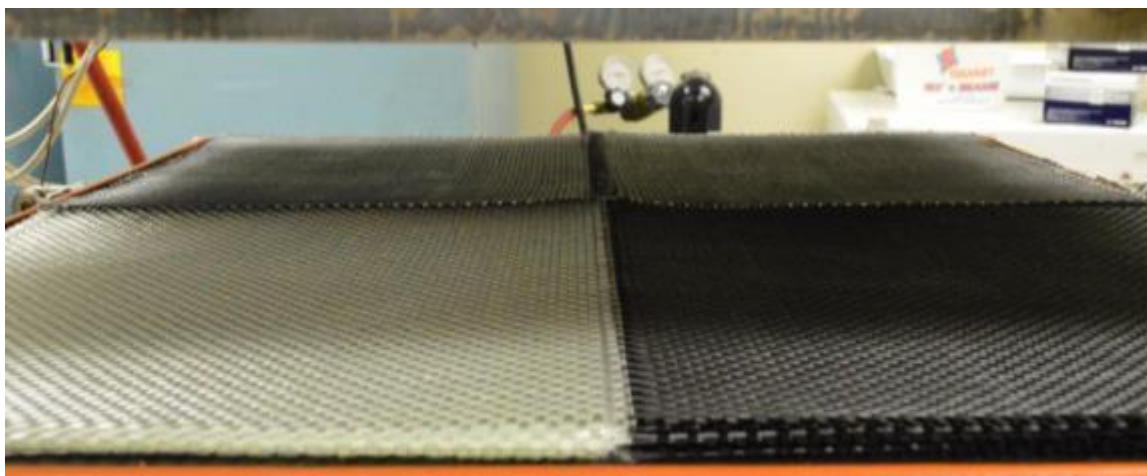


Figure 7. A four sample 8-layer glass fabric preform with weight concentrations with respect to matrix ranging from (back-left) 1.0 %, (back-right) 1.5 %, (front-right) 2.0 %, and (front-left) 0 %.

## MATRIX CHARACTERIZATION

### MICROSCOPY

The morphology of the nylon polymer, particularly the size and organization of spherulites, was investigated using the transmission cross-polarization technique with a Zeiss Axioplan 2 microscope. Neat and nanocomposite thin film samples were polymerized between glass slides in a dry glove box. The dry powder samples from the induction time sample stock were separately placed onto one glass slide and covered with another and placed onto a hotplate. The hotplate was set to 150 °C, and the films were cured within 2 minutes. Concentration by weight of NGP for the multiscale sample was 0.1 wt. %.

The effect of NGP on the overall wettability of the fibers was qualitatively evaluated using scanning electron microscopy (SEM). With the high concentration of NGP, there existed the possibility that the NGP could inhibit flow into the fiber tows. SEM images were acquired with a Quanta FEG 650 Scanning Electron Microscope under low vacuum. A low pressure of water vapor, approximately 80 Pa, was used to create a

conduction path ordinarily provided by Au-Pd coating. A gaseous secondary electron detector (GSED) was used. An accelerating voltage of 5kV was used for imaging.

#### DIFFERENTIAL SCANNING CALORIMETRY (DSC)

DSC measurement of the effect of NGP concentration on APA-6 polymer was done using a TA Instruments DSC equipped with a TA Q100 Controller and refrigerated cooling system. The crystallinity was measured with a standard ramp procedure from 40–320 °C at 10 °C min<sup>-1</sup>.

#### X-RAY DIFFRACTION (XRD)

X-ray diffraction analysis was performed on a Siemens D500 PC Diffraction System. The source was Cu k<sub>α</sub> with a wavelength  $\lambda=1.54056$  nm. Crystallographic information for APA-6 and NGOPs was determined by peaks in the x-ray intensity versus 2 $\theta$  angle, corresponding to satisfaction of Bragg's law of x-ray diffraction.<sup>21</sup> The scan was from 10°–30° with a 0.1° step and a 10 s. dwell time.

#### THERMOGRAVIMETRIC ANALYSIS (TGA)

A TA Instruments Thermogravimetric Analyzer (TGA 2950) was used to determine the effect of NGPs on the thermal stability of the APA-6 and to determine the equilibrium concentration in cast samples due to settling. Sample chips were ramped to 600 °C at 20 °C min<sup>-1</sup> in nitrogen. Temperature at 10% mass loss T<sub>90</sub> and the temperature at the maximum weight loss rate T<sub>max</sub> were recorded. The remaining mass fraction at 600 °C was recorded to estimate the equilibrium NGP concentration. A reference NGP sample was also run to adjust concentration calculations if necessary.

## LAMINATE CHARACTERIZATION

A careful survey of the thickness of the as-produced panels showed considerable variability. The thickness and the volume content of reinforcing fibers for an infused composite are proportional and thus needed to be considered during data analysis. Since compacting fabric spreads laterally, the thickness does not perfectly predict the volume fraction, but the difference was expected to be small. If the lateral expansion is ignored, the following derivation is applicable. Knowing the areal mass  $m_A$  of the fabric and the intrinsic density of the fiber material  $\rho_f$ , the solid thickness  $t_s$  of glass can be derived as follows:

$$t_s = \frac{m_A}{\rho_f} \quad (5)$$

To calculate the volume fraction of fiber  $V_f$  the solid thickness is used as a scaling factor:

$$V_f = t_s t_c^{-1} \quad (6)$$

The bounds of laminate thickness  $t_c$  in Equation (6) are from the solid thickness  $t_s$ , where the volume fraction reduces to unity, to infinity, where the volume fraction approaches zero. The expression was used to isolate mechanical property variation caused by NGP concentration from the effect of volume fraction variation.

## CONTINUOUS EXCITATION VIBRATION ANALYSIS

The dynamic vibration response of a composite material in the form of natural frequency and damping ratio is an effective tool to predict the acoustic damping performance of the material in service. For this work, the technique was evaluated as a method to characterize the interaction of the constituent components of the composite. Two types of damping, viscous and frictional (Coulomb), were probable for the

composite samples. Viscous damping arises from the viscoelastic nature of the matrix polymer. Coulomb or friction damping was hypothesized to be present in the composite caused by free surfaces sliding against one another.<sup>22</sup> This type of damping was expected to occur in a composite with de-wetted interfaces between the reinforcement and the matrix. For multiscale composites with nanoparticles incorporated into the matrix, a change in the damping characteristics of the material was expected if (a) the nanoplatelets were discontinuous with the matrix due to incompatible chemistry, or if (b) the concentration of nanoparticles was greater than the percolation limit, preventing adequate bonding with the matrix.<sup>23</sup> For the case of NGP dispersed in the matrix of a GF/APA-6 laminate, the hypothesis was that the damping capacity of the laminate would suddenly increase for concentrations above the percolation limit.

Measurement of the vibration damping response of samples was done in a free-free boundary condition. The samples were mounted on their geometric center with beeswax to a B&K Type 8001 accelerometer, which served as the input and output sensor simultaneously. A random input signal was induced by a B&K 4809 mini shaker and B&K Type 2706 amplifier with a range of 0 to 25.6 kHz. Vibration response was recorded with a B&K 3560-B-140 signal analyzer and converted into a frequency response using fast Fourier transformation (FFT).

Calculation of the damping ratio was done via the -3 dB half-power bandwidth method.<sup>22</sup> The damping ratio  $\zeta$  is calculated from the frequency response curves as follows:

$$\text{Damping Ratio } \zeta = \frac{\Delta f_{-3dB}}{f_n}, \quad (7)$$

where  $f_n$  is the frequency associated with a natural frequency mode of vibration of the sample and  $\Delta f_{-3dB}$  is the width of the peak at a reduced intensity of -3 dB from the peak.

A typical baseband curve is shown in Figure 8. Each of the peaks corresponds to a natural frequency of the sample vibrating in a particular mode. The peak with the lowest frequency is the first flexural mode of vibration at approximately 396 Hz. Immediately following the resonant peak is the anti-resonant peak pointing to the negative direction. The second resonant peak appears at 2396 Hz. and corresponds to the third mode of flexural vibration. For each of the resonant peaks, a more detailed ‘zoomed’ portion of the output was recorded to enhance resolution.

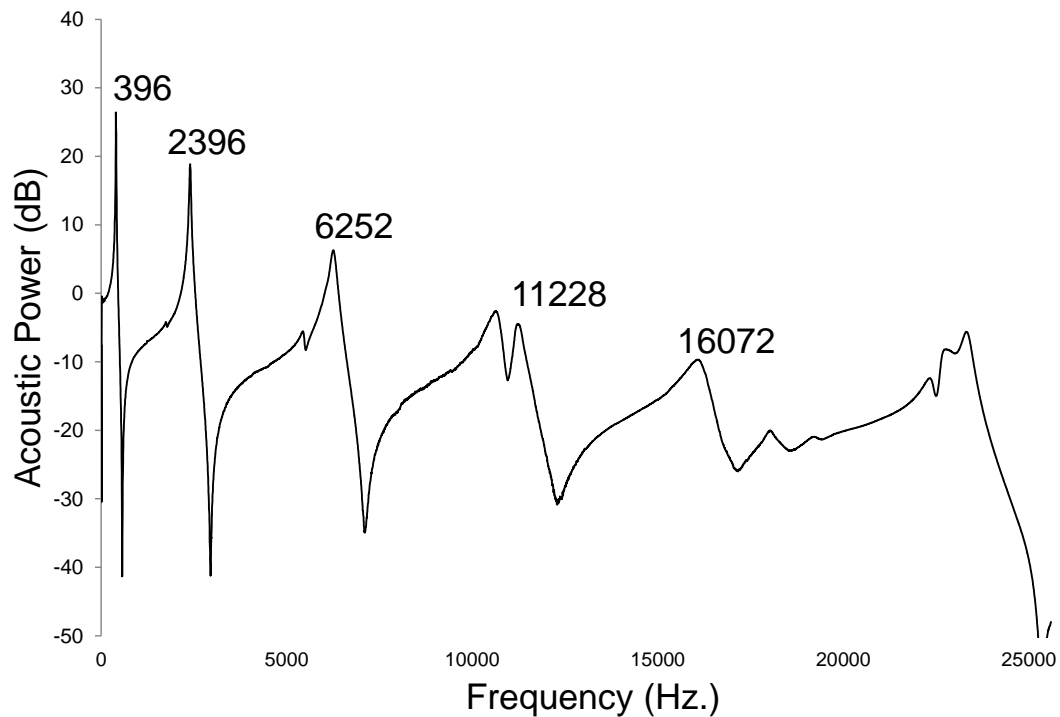


Figure 8. A typical baseband frequency response from continuous excitation vibration analysis of a beam sample. Labels indicate from left to right the harmonic resonant peaks. Each peak is accompanied by an anti-resonant valley at a slightly higher frequency. The final peak near 23000 Hz. is caused by the metal disc threaded into the accelerometer for sample attachment.

### THREE-POINT BEND TESTS

Flexure tests were performed on samples with a ratio of span to depth greater than 36:1 following ASTM D7264M-07.<sup>24</sup> A three-point bend fixture with 6 mm (0.25 in) steel cylinders and a span of 130 mm was placed into an Instron SATEC T Series load frame. Force was recorded using an Interface Manufacturing load cell Model 1210AF-5K with a capacity of 22.2 kN (5 kip). Load was applied at a crosshead rate of 5 mm min<sup>-1</sup>. Short beam shear tests were performed according to ASTM D2344 using the same fixture as flexure tests except the span was changed to 15 mm giving a span-to-depth ratio of approximately 6.<sup>25</sup> Cross-head speed was set at 1.0 mm min<sup>-1</sup>.

### THERMAL CONDUCTIVITY

Round discs with a diameter of 47 mm were cut from the panel using a computer numeric control mill program. Thermal conductivity in the through-thickness direction was then measured using a LaserComp Fox50 heat flow meter. Instrument air pressure was 60 psi. A thermal gradient of 20 °C was maintained for a given temperature set point. For example, the top and bottom temperatures were maintained at 70 °C and 90 °C to obtain the sample thermal conductivity at 80 °C. Several set points were measured to give the through-thickness thermal conductivity over a temperature range from 30–100 °C.

## RESULTS AND DISCUSSION

### MATRIX CHARACTERIZATION

The morphological characteristics of APA-6 affect the mechanical behavior of the bulk polymer. Frunze et al. demonstrated that the presence of heterogeneous particles such as carbon black and silica gel powder produced a homogeneous spherulite structure

of APA-6. For concentrations below the corresponding particle agglomeration limit, several nuclei species improved mechanical property consistency. Additionally, impact toughness was improved several times.<sup>26</sup>

Evidence of spherulite refinement is shown in Figure 9(b.). The micrographs were taken from samples that were polymerized using the same batch of ground monomer, activator, and initiator. The samples were also polymerized simultaneously under identical conditions. Although the NGP are clearly visible in Figure 9 (b) as dark regions of agglomerated platelets, the fine spherulite structure was less coarse throughout the sample. Yield strength and modulus were expected to be improved slightly for samples containing NGP due to the refined spherulite structure.<sup>26, 27</sup>

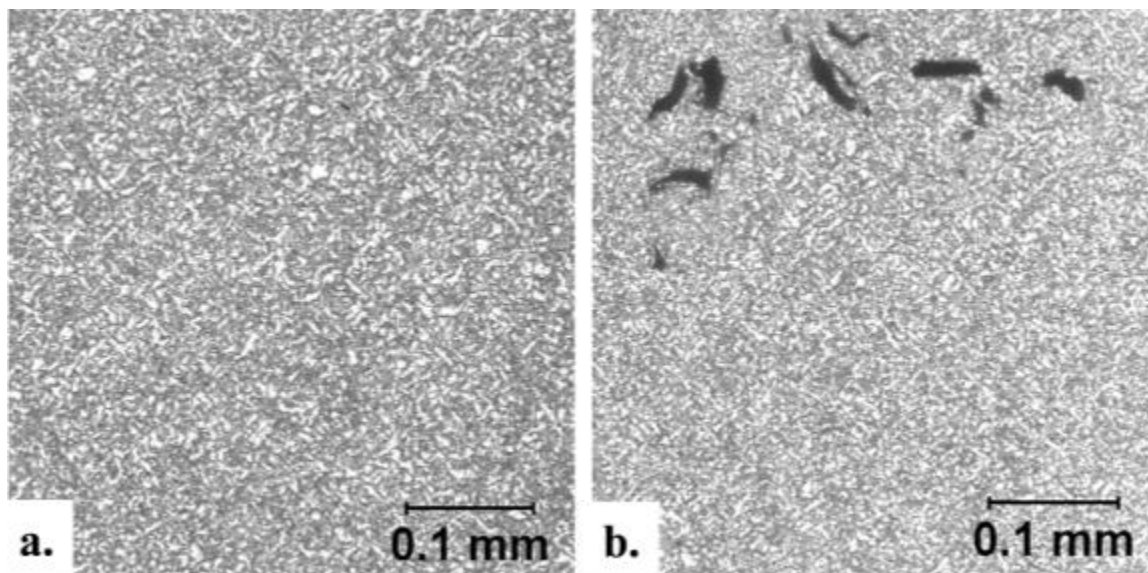


Figure 9. A transmitted-light polarization micrograph of a neat APA-6 film (a.) and a film with 0.1 wt. % NGPs (b.). Both samples exhibit a granular spherulite structure. Nanocomposite samples showed a finer spherulite structure, which agrees with literature.<sup>17, 26</sup>

#### INDUCTION TIME

For the rheological measurement of the induction time, it should be noted that the initial monomer viscosity was also essentially unaffected by the nominal concentration of

NGPs up to 2.0 wt. %. The result is in accordance with findings by Bansal which suggests that unlike MWCNTs, the NGPs with a high concentration could be added to a resin system without adversely affecting the processability.<sup>28</sup>

The results of the time-sweep experiments are shown in Figure 10. During the time sweep experiments, the monomer solution was able to evaporate from between the aluminum plates despite the small 200  $\mu\text{m}$  gap. Also, since the test samples were necessarily, briefly exposed to ambient laboratory air, the possibility of moisture contamination was probable. Moisture contamination would serve to inhibit the anion activity and effectively increase the induction time measured. Validation points taken with DSC are also shown in Figure 10. Since DSC samples were sealed and never exposed to laboratory air, the measurements served as a validation of the rheological technique.

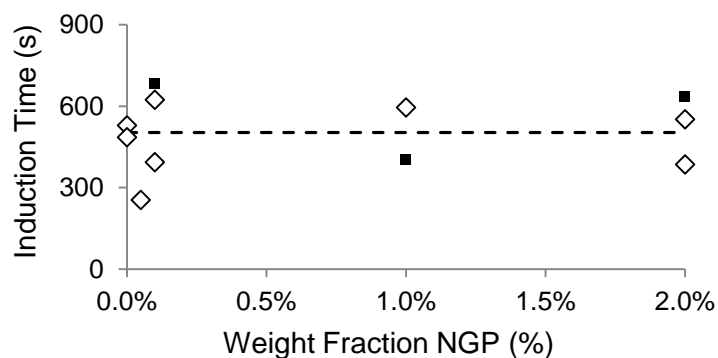


Figure 10. The results of the induction time measurements as measured by rheology ◇ and DSC ■. The overall average shown as a dashed line was approximately 500 s.

The two methods indicated similar average induction times of 570 s for DSC and 480 s for rheology. A possible source of error between the techniques was that the DSC controls temperature with greater precision than the Rheometer. Equation (3) shows that a slight increase in temperature results in an exponential change in the instantaneous

conversion rate. Both techniques, however, showed no measurable change in reaction rate with NGP concentration.

### THERMAL STABILITY AND NGP CONCENTRATION

The as-cast samples showed distinct domains of NGP concentration. At the bottom of the sample, a “graphite-rich” phase formed due to the settling of the platelets during polymerization. The remaining polymer, however, was visibly grey in color indicating a residual dispersed concentration of NGPs and was termed the “graphite-poor” phase. Thermogravimetric analysis was done to determine the effect of NGPs on thermal stability of the APA-6 polymer and to estimate the concentration of NGPs in each of the phases.

The temperatures of 10% mass loss and maximum loss rate,  $T_{90}$  and  $T_{max}$ , respectively are shown in Figure 11. For each concentration, the residual mass percent of the graphite-poor phase was subtracted from the residual mass of the corresponding graphite-rich phase. The total was adjusted by the residual fraction of the pure NGP sample at 600 °C,  $X_{pure}$ , per Equation (8) and is summarized in Table 1 as  $C_{NGP}$ . Since residual mass of the graphite-poor phase was comparable to that of neat APA-6 as illustrated in Figure 12, it was assumed that the contribution by mass of NGPs was negligible for further calculations for those samples.

$$C_{NGP} (wt. \%) = \frac{R_{rich_i} - R_{poor_i}}{X_{pure}}, \quad (8)$$

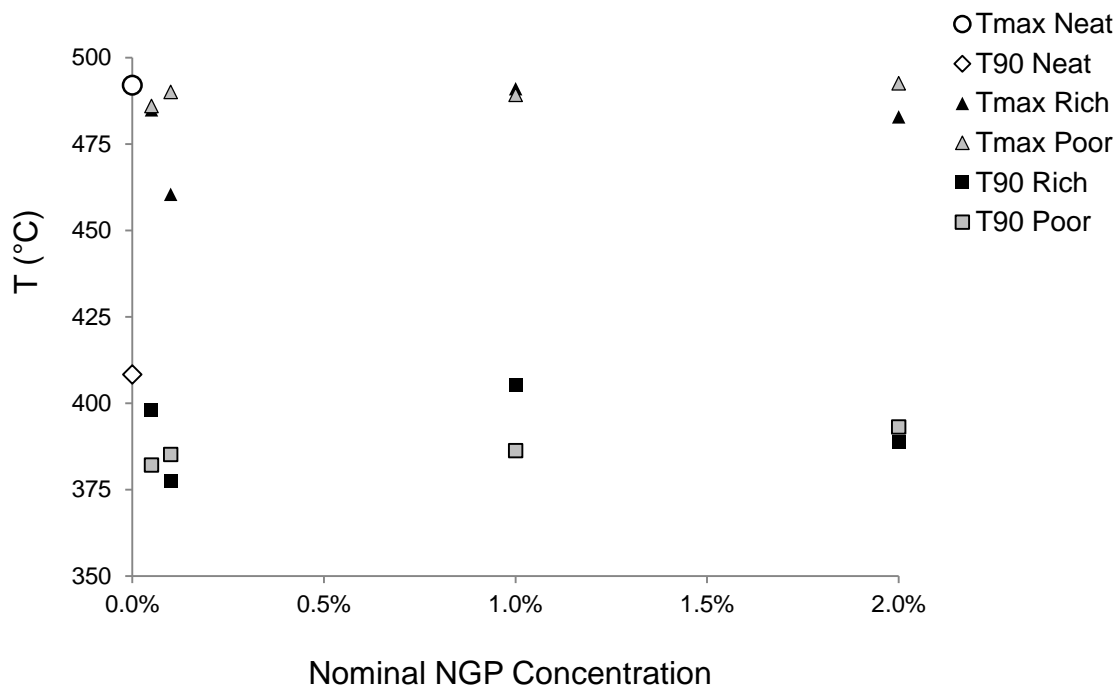


Figure 11. Temperature of 10 % mass loss and maximum loss rate as determine by TGA.

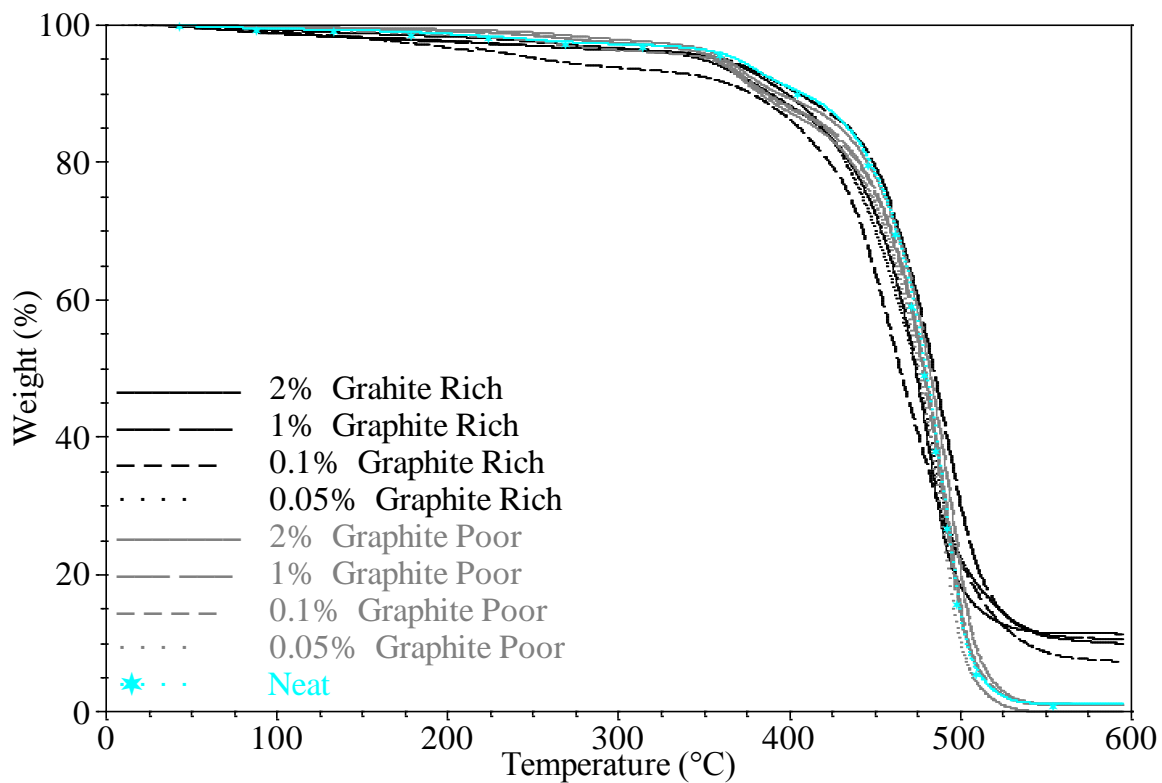


Figure 12. TGA curves from both phases: graphite rich (black), graphite poor (grey), and neat (blue \*).

Table 1. A summary of TGA and DSC thermal data for APA-6/NGP cast samples.

Sample	TGA				DSC Heat			DSC Cool	
	T <sub>90</sub> (°C)	T <sub>max</sub> (°C)	R (%)	C <sub>NGP</sub> (wt. %)	T <sub>m</sub> (°C)	ΔH <sub>m</sub> (J/g)	α* (%)	T <sub>c</sub> (°C)	ΔH <sub>c</sub> * (J/g)
Graphite Poor-2%	393	493	1.12	†	217	102	45	189	72.1
Graphite Poor-1%	386	489	0.96	†	208	84.7	37	187	75.2
Graphite Poor-0.1%	385	490	1.00	†	209	84.3	37	177	73.0
Graphite Poor-0.05%	382	486	0.00	†	214	77.8	34	173	70.3
Graphite Rich-2%	389	483	11.45	11	223	94.8	46	182	78.2
Graphite Rich-1%	405	491	10.58	10	221	100	48	181	92.6
Graphite Rich-0.05%	398	485	10.00	10	218	74.2	36	187	84.4
Neat APA-6	408	492	1.2	0	219	101	44	181	84.3
Pure NGP	-	412	97	-	-	-	-	-	-

\* Adjusted by weight fraction of NGPs. † No measureable difference from neat APA-6

DSC heat-cool plots were obtained for each sample type. The maxima of the melting and cooling heat flow peaks are recorded in Table 1 as T<sub>m</sub> and T<sub>c</sub>, respectively. The heat of melting was calculated by linear integration of the endothermic peak and is denoted as ΔH<sub>m</sub>. Percent crystallinity was calculated as shown in Equation (9) by adjusting for NGP concentration in the rich phases and is denoted as α. The graphite-poor phases were not adjusted since the NGP concentration could not be reliably determined with TGA analysis.

$$\alpha(\%) = 100 \times \frac{\Delta H_m}{(1 - C_{NGP})\Delta H_m^0}, \quad (9)$$

Crystallinity was normalized by the value for neat APA-6 and plotted in Figure 13. Heats of fusion ΔH<sub>c</sub> summarized in Table 1 were calculated from a linear integral of the cooling exotherm. The melting and cooling temperatures T<sub>m</sub> and T<sub>c</sub> are shown in Figure 14 with respect to nominal NGP concentration. The presence of NGPs showed no significant effect on the melt and solidification temperatures of the graphite poor regions making them comparable to neat APA-6. The result was somewhat contradictory to

literature.<sup>14, 26</sup> The presence of NGPs was expected to induce heterogeneous nucleation of the polymer during cooling thereby increasing the solidification temperature  $T_c$ .

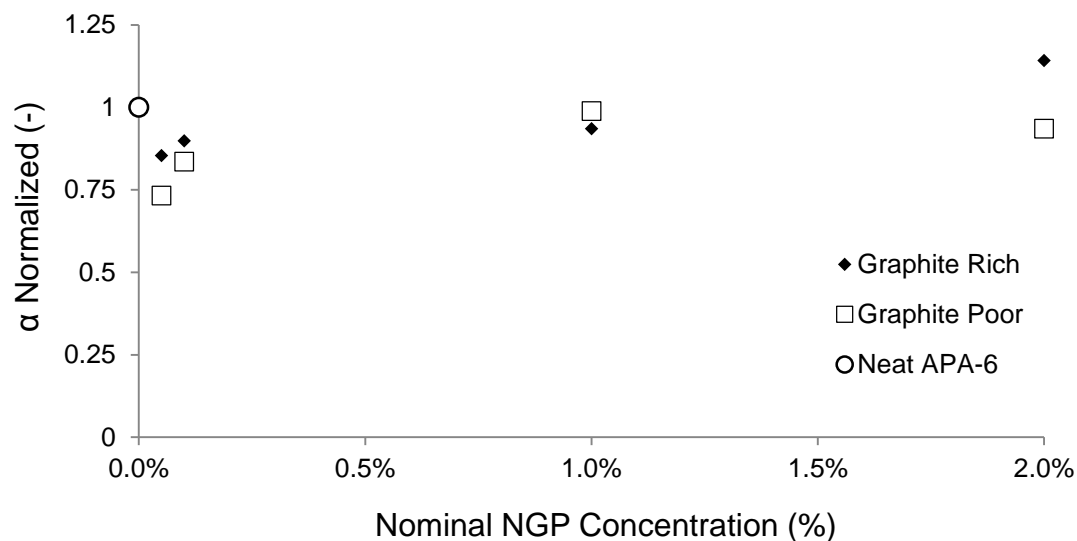


Figure 13. Crystallinity as measured by DSC, adjusted for NGP concentration and normalized by neat APA-6

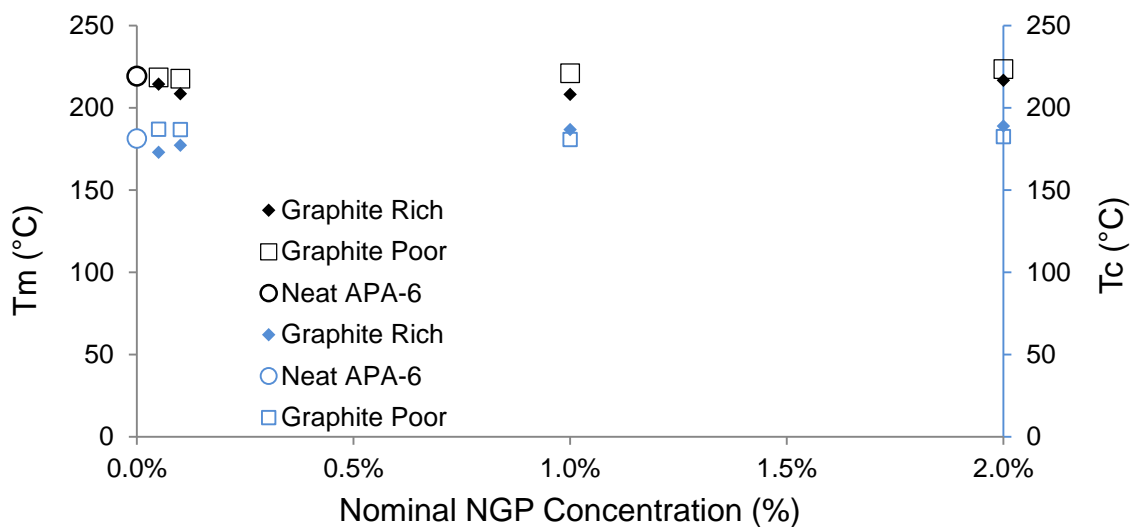


Figure 14. Temperatures of melting (black) and cooling (blue) as determined by local maxima of DSC peaks.

The analysis of the crystalline structure of the APA-6 was done using XRD. A metastable crystal phase of APA-6, denoted as  $\gamma$  in literature, has been shown to be

caused by MWCNTs embedded into PA-6.<sup>21</sup> No metastable  $\gamma$ -phase was observed for the NGP/APA-6 composites as shown in Figure 15.

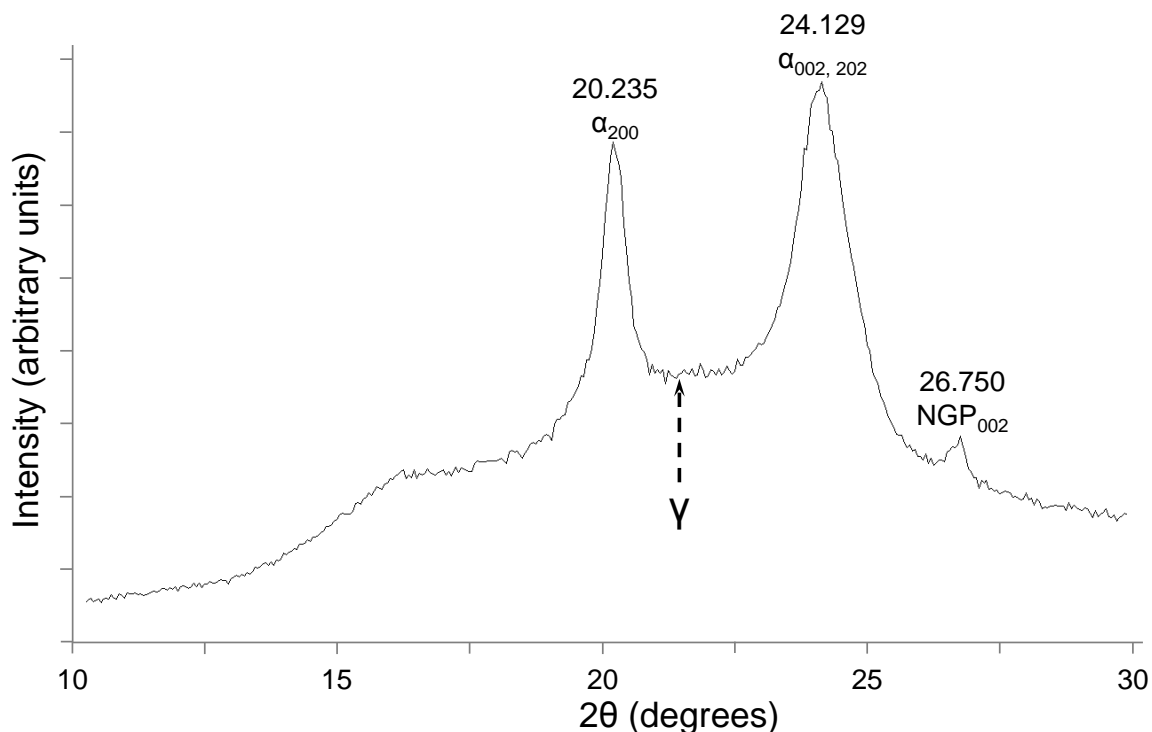


Figure 15. The X-ray diffraction pattern obtained from an NGP/APA-6 sample. The two primary peaks correspond to the  $\alpha$ -crystal structure of APA-6.<sup>21</sup> A small peak at 26.750 corresponds to the NGP 002 graphite peak.<sup>29</sup> The position of the metastable  $\gamma$ -crystal structure of APA-6 is marked with an arrow. No  $\gamma$  peak was observed.

### LAMINATE CHARACTERIZATION

The wet-out quality of the laminates at the inter-ply regions was evaluated with SEM images. The NGP concentration was highest in the immediate vicinity of the ply surfaces. Figure 16 shows the complete wet-out of the laminate at the interfaces.

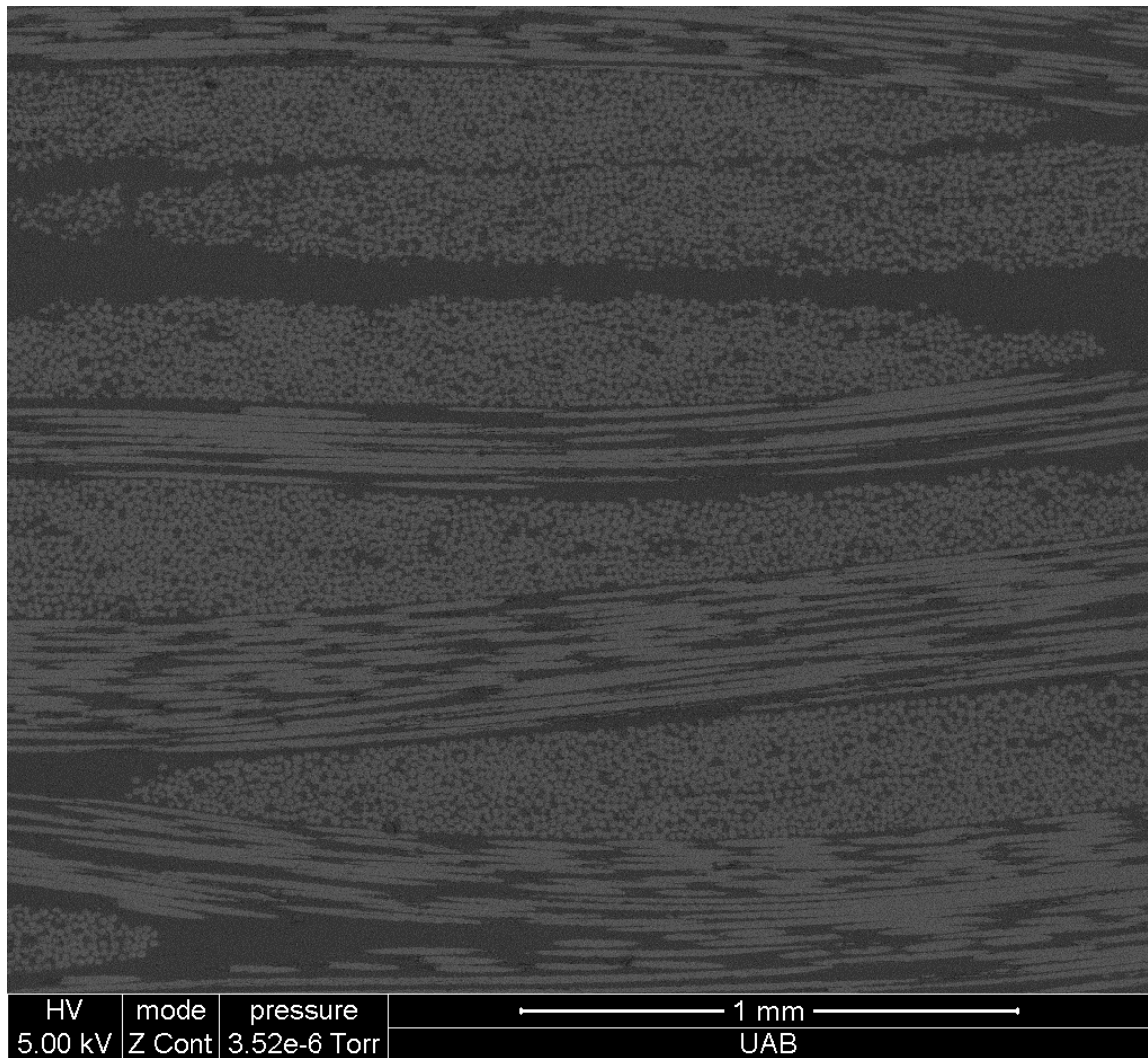


Figure 16. A GSED image of a 2.0 wt. % NGP laminate. The sample was cut in the y-z plane and polished. Infusion was uniform as can be observed from the lack of voids in the image.

### DYNAMIC VIBRATION RESPONSE

The validity of the half-power method at determining the damping ratio depends on a combination of factors. The sample was attached to the accelerometer using beeswax. The thickness of the beeswax had a profound effect on the shape of the output curve. Thick beeswax reduced the peak height, and thin wax increased the peak height. This test was therefore only valid on a comparative basis against a baseline dataset. An attempt was made to use a consistent quantity of beeswax and equal pressure to mount

each sample for repeatability of the test. In general, there was no discernable difference between neat and multiscale samples in terms of the damping ratio as is shown in Figure 17. Perhaps, if only slightly, the neat samples exhibited higher damping capacity than the multiscale samples.

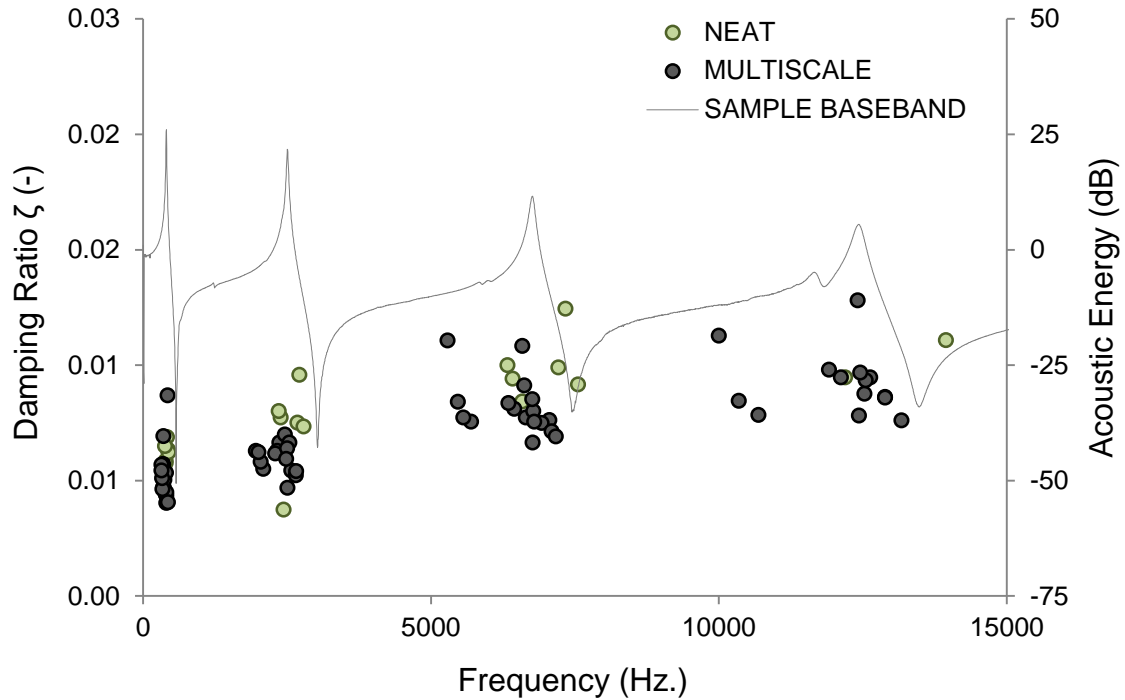


Figure 17. Damping ratio comparison for neat and multiscale  $0^{\circ}/90^{\circ}$  laminate samples.

### MECHANICAL RESPONSE

The short-beam strength was maximum at a nominal NGP content of 0.5 wt. %. Further addition of NGPs reduced the short-beam strength as can be observed in Figure 18 (left). The short-beam strength was determined to be largely independent of the fiber volume fraction after observing each data point plotted with respect to volume fraction shown in Figure 18 (right). The data points from each concentration were grouped and independent of the volume fraction. The short-beam strength of a composite is a matrix-dominated property. Since NGPs were added specifically to enhance the matrix

properties, the results were expected to be the most dramatic for short-beam tests. The failure mode for all tests was identical. First, the top layers failed under compression. Second, inter-ply delamination was observed near the mid-plane of the sample. Finally, tensile failure occurred on the bottom plies.

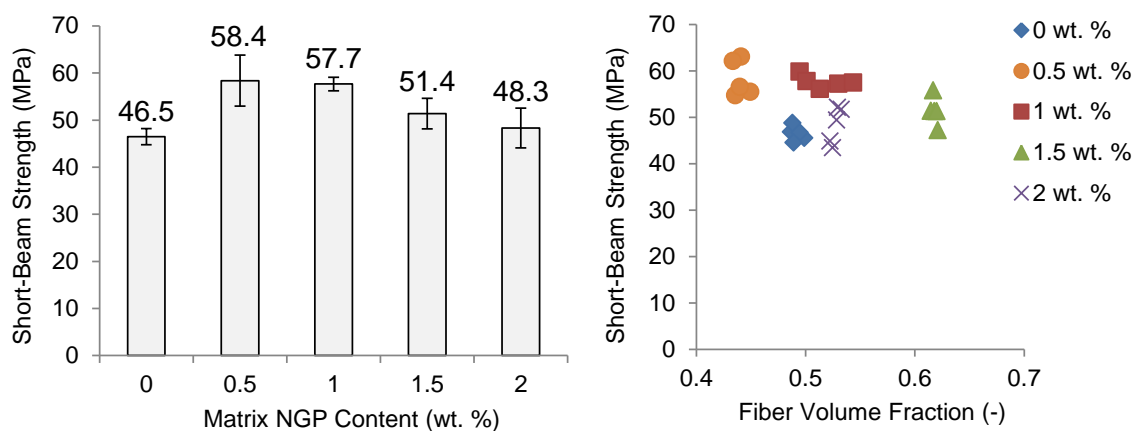


Figure 18. (Left) Short beam shear strength with nominal matrix NGP concentration. (Right) Short beam shear strength with respect to glass fiber volume fraction. The improvement in short-beam strength was determined to be solely dependent on NGP concentration and independent of volume fraction variation caused by thickness variations between the samples.

Flexural strength data obtained is summarized in Figure 19. The average flexural strength was not statistically independent. NPG concentration had little effect on the flexural data, as had been observed in previous work.<sup>30</sup> Sample variability was reduced slightly with NGP concentration above 1.0 wt. %. The effect could be evidence of a refined spherulite structure following literature.<sup>26</sup> Flexural modulus data is summarized in Figure 20.

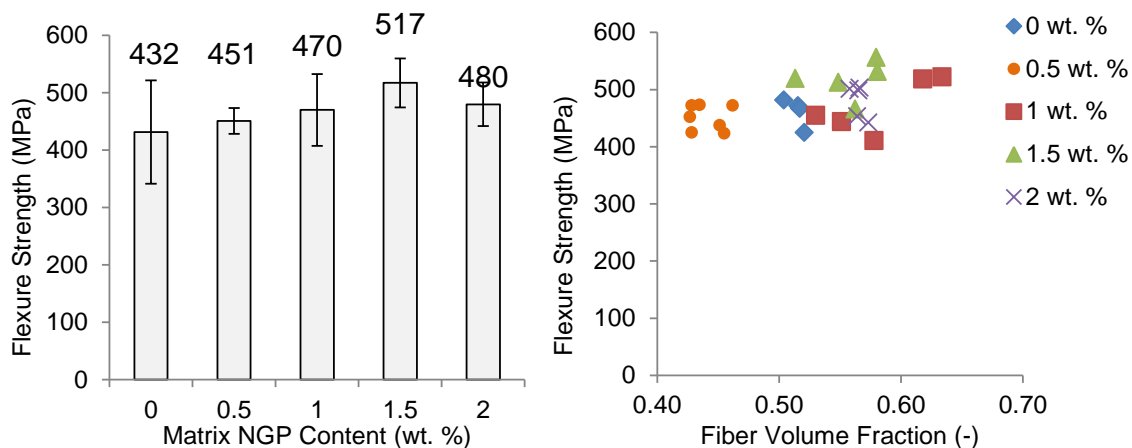


Figure 19. Flexural strength results. Variability tended to decrease with NGP concentration. However, with only 5 samples tested of each, no statistical difference can be concluded. On the right, the flexural strength is shown with respect to volume fraction.

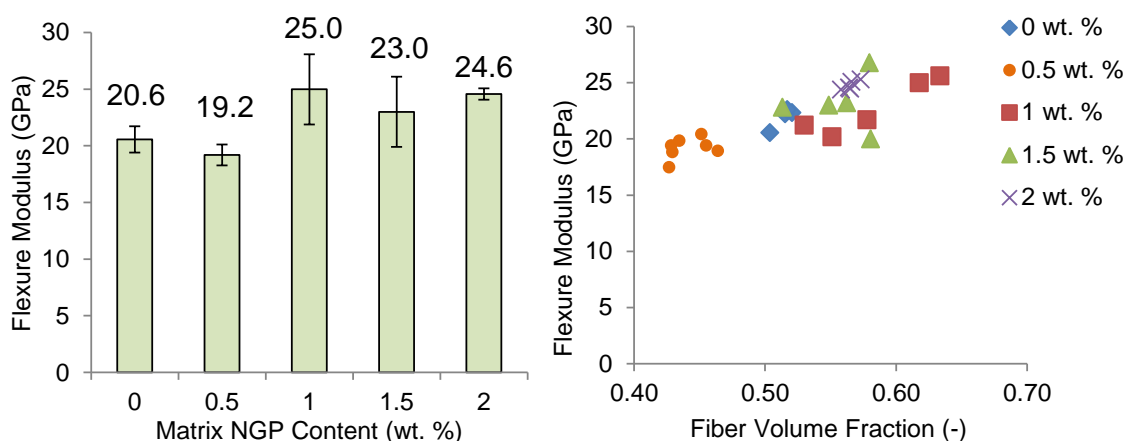


Figure 20. Flexural modulus showed no correlation with NGP concentration. However, when comparing the modulus with calculated fiber volume fraction from Equation (6), the dominant effect of volume fraction is evident.

## THERMAL CONDUCTIVITY

Conductivity results are shown in Figure 21. The through-thickness conductivity showed little dependence on concentration up to 2 wt. %, where a sudden change in conductivity was measured. The interpretation of the result was that the platelets were approaching the percolation limit and beginning to form a continuous network of NGPs to provide a through-thickness thermal conduction path. The variability between samples

at 2 wt. % NGP appears to be greater than the other concentrations. The possible explanation is that the percolation threshold is close to 2 wt. %. Additional tests at higher nominal NGP contents could confirm the result more explicitly.

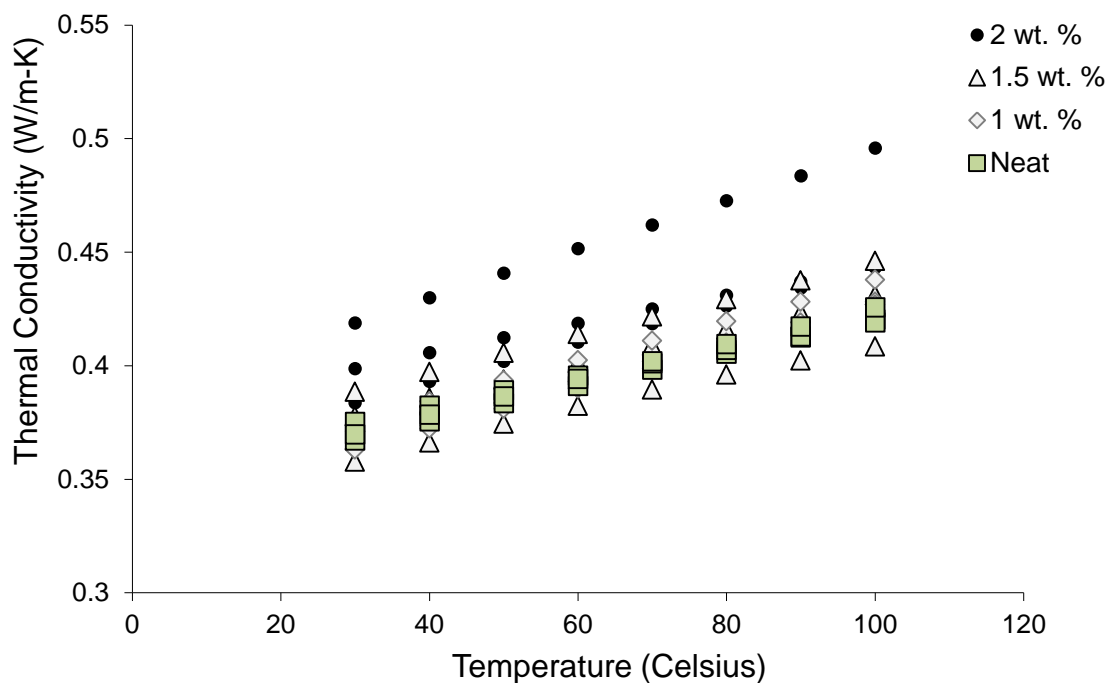


Figure 21. Thermal conductivity results as measured by the Fox50 instrument.

## CONCLUSIONS

A direct and indirect method to measure the induction time of APA-6 polymerization was demonstrated. No change in induction time was observed for the NGP concentration range from 0–2.0 wt. % tested in the study. The results were in concurrence with a simple kinetic model. Further study at higher concentrations of NGPs is required to determine whether or not the NGPs catalyze the APA-6 reaction.

Cast samples of varying nominal NGP concentrations tended to separate into two distinct phases: one graphite-rich and one graphite-poor. The graphite-rich phase had a concentration of approximately 9 wt. % as measured by TGA analysis and was

independent of the initial NGP concentration. Graphite concentration in the graphite-poor phase was not measurable with thermogravimetric analysis. However, the graphite-poor phase was grey in color with higher initial concentrations appearing darker. The presence of NGPs had no effect on the thermal stability of APA-6 for the measured concentrations up to 9 wt. %. Other thermal properties such as crystallinity and melting behavior were unaffected. XRD analysis showed that NGPs did not induce the metastable  $\gamma$  crystal structure of the APA-6 polymer.

Micrographs of APA-6 films showed a visibly refined spherulite structure for samples containing 0.1 wt. % NGPs, in agreement with literature.<sup>17, 26</sup> The initial viscosity of the monomer solution was not noticeably affected by NGP concentration for the measured range of 0–2.0 wt. %. Wettability of the fiber tows was also confirmed using SEM micrographs.

The addition of NGPs to APA-6 caused a maximum of 25.6 % increase in short-beam strength at a concentration of 0.5 wt. %. The samples failed first under compression, followed by mid-plane delamination, and finally tensile failure. The failure mode was unaffected by the presence of NGPs indicating that the compressive strength of the laminate was probably not improved. Flexural strength and modulus were unaffected by NGP concentration except that the sample to sample variability may have been reduced due to spherulite refinement. The flexural properties were shown to be primarily a function of the volume fraction of the laminate due to thickness variation from processing. The vibration damping capacity of the composite was not changed appreciably by the presence of NGPs except to possibly reduce the damping capacity slightly over the neat samples. Thermal conductivity of the composite was consistent for

the chosen temperature range, except that the 2.0 wt. % samples showed a larger variability between samples. One possible interpretation is that the percolation threshold to provide a substantial thermal conduction path could be close to 2.0 wt. %.

#### ACKNOWLEDGEMENTS

The support provided by National Science Foundation NSF RII program from the Alabama Center for Nanostructured Materials, Graduate Research Scholarship Program (GRSP) is gratefully acknowledged. Many thanks to PPG Industries Inc. for their financial support and for donating materials. Special thanks go to the UAB SEM Laboratory for help with acquiring micrographs.

#### REFERENCES

1. Schinner G, Brandt J and Richter H. Recycling Carbon-Fiber-Reinforced Thermoplastic Composites, *Journal of Thermoplastic Composite Materials* 1996; 9: 239-45.
2. Parton H and Verpoest I. In situ polymerization of thermoplastic composites based on cyclic oligomers, *Polym Composite* 2005; 26: 60-5.
3. Goettler LA and Neff WJ. Mechanical performance of various nylon 6 composites formed by in-situ polymerization of caprolactam, *Polym Composite* 1986; 7: 383-94.
4. Otaigbe JU and Harland WG. Studies in the properties of nylon 6 glass fiber composites, *Journal of Applied Polymer Science* 1988; 36: 165-75.
5. Van Rijswijk K, Teuwen JJE, Bersee HEN and Beukers A. Textile fiber-reinforced anionic polyamide-6 composites. Part I: The vacuum infusion process, *Composites Part A: Applied Science and Manufacturing* 2009; 40: 1-10.
6. Pillay S, Vaidya UK and Janowski GM. Liquid Molding of Carbon Fabric-reinforced Nylon Matrix Composite Laminates, *Journal of Thermoplastic Composite Materials* 2005; 18: 509-27.
7. Moller E, Bailey DM and Berghahn M. Camisma -- new composites for lighter cars. In: *SAMPE tech* (eds Charleston, SC, 22-25 October, 2012).
8. Wichterle O. On caprolactam polymerization, *Die Makromolekulare Chemie* 1960; 35: 174-82.

9. Van Rijswijk K, Bersee HEN, Beukers A, Picken SJ and van Geenen AA. Optimisation of anionic polyamide-6 for vacuum infusion of thermoplastic composites: Influence of polymerisation temperature on matrix properties, *Polymer Testing* 2006; 25: 392-404.
10. Barfknecht PW, Pillay B and Vaidya UK. Multiscale anionic polyamide-6 composites with selective incorporation of nanoparticles. *International SAMPE Technical Conference*. 2013.
11. Šebenda JAN. Lactam Polymerization, *Journal of Macromolecular Science: Part A - Chemistry* 1972; 6: 1145-99.
12. Sibal PW, Camargo RE and W. MC. Designing nylon-6 polymerization systems for RIM. In: *2nd International Conference on Reactive Polymer Processing* (eds Pittsburgh, PA, November, Nov. 1982, pp.97-145.
13. Van Rijswijk K, Bersee HEN, Jager WF and Picken SJ. Optimisation of anionic polyamide-6 for vacuum infusion of thermoplastic composites: Choice of activator and initiator, *Composites Part A: Applied Science and Manufacturing* 2006; 37: 949-56.
14. Weng WG, Chen GH and Wu DJ. Crystallization kinetics and melting behaviors of nylon 6/foiled graphite nanocomposites, *Polymer* 2003; 44: 8119-32.
15. Malkin AY, Frolov VG, Ivanova AN and Andrianova ZS. The nonisothermal anionic polymerization of caprolactam, *Polymer Science USSR* 1979; 21: 691-700.
16. Malkin AY, Ivanova SL, Frolov VG, Ivanova AN and Andrianova ZS. Kinetics of anionic polymerization of lactams. (Solution of non-isothermal kinetic problems by the inverse method), *Polymer* 1982; 23: 1791-800.
17. Rusu G and Rusu E. In situ nylon 6/graphite composites. Physico-mechanical properties, *J Optoelectron Adv M* 2007; 9: 2102-9.
18. Yang M, Gao Y, Li H and Adronov A. Functionalization of multiwalled carbon nanotubes with polyamide 6 by anionic ring-opening polymerization, *Carbon* 2007; 45: 2327-33.
19. Yan D and Yang G. Synthesis and properties of homogeneously dispersed polyamide 6/MWNTs nanocomposites via simultaneous in situ anionic ring-opening polymerization and compatibilization, *Journal of Applied Polymer Science* 2009; 112: 3620-6.
20. Bansal D, Pillay S and Vaidya U. Nanographite-reinforced carbon/carbon composites, *Carbon* 2013; 55: 233-44.

21. Jose MV, Steinert BW, Thomas V, et al. Morphology and mechanical properties of Nylon 6/MWNT nanofibers, *Polymer* 2007; 48: 1096-104.
22. Nashif AD, Jones DIG and Henderson JP. *Vibration damping*. New York: Wiley, 1985, 453 p.
23. Advani SG. *Flow and rheology in polymer composites manufacturing*. Amsterdam, New York: Elsevier, 1994, 608 p.
24. ASTM D7264M-07, Standard Test Method for Flexural Properties of Polymer Matrix Composite Materials, ASTM International, West Conshohocken, PA, 2007, [www.astm.org](http://www.astm.org)
25. ASTM D2344 / D2344M - 00e1, Standard Test Method for Short-Beam Strength of Polymer Matrix Composite Materials and Their Laminates, ASTM International, West Conshohocken, PA, 2010, [www.astm.org](http://www.astm.org)
26. Frunze TM, Shleifman RB, Zhirova LV, Kurashev VV and Zaitsev VI. Study of the structure and properties of poly- $\epsilon$ -caproamide formed during anionic polymerization of  $\epsilon$ -caprolactam in the presence of artificial structure-forming nuclei, *Polymer Science USSR* 1972; 14: 3115-22.
27. Kohan MI. *SPE monographs : nylon plastics*. New York: John Wiley & Sons, Inc., 1973, 683 p.
28. Bansal D, Pillay S and Vaidya U. Processing and characterization of nanographene platelets modified phenolic resin as a precursor to carbon/carbon composites—part I, *Journal of Reinforced Plastics and Composites* 2013; 32: 585-92.
29. Bansal D, Pillay S and Vaidya U. Processing and characterization of nanographene platelets modified phenolic resin as a precursor to carbon/carbon composites (part II), *Journal of Reinforced Plastics and Composites* 2013; 32: 955-63.
30. Barfknecht P, Pillay SB and Vaidya UK. Multiscale anionic polyamide-6 composites with selective incorporation of nanoparticles. In: *SAMPE Tech* (eds Wichita, KS, October 21-24, 2013).

SINGLE-STREAM PROCESSING TECHNIQUE FOR *IN-SITU* POLYMERIZATION  
OF GLASS FIBER/POLYAMIDE-6 LAMINATES

by

PETER W. BARFKNECHT, JUSTIN MARTIN, BRIAN (SELVUM) PILLAY, UDAY  
K. VAIDYA, AND GARY M. GRAY

In preparation for *Journal of Thermoplastic Composite Materials*

Format adapted for dissertation

## ABSTRACT

Anionic ring opening polymerization of anionic polyamide 6 (APA-6) requires both an activator and an initiator for the reaction to occur. Typical processing techniques for liquid-molded thermoplastic composite laminates involve infusion of the reinforcement with a pre-mixed monomer solution containing both activator and initiator species. The technique described here is a step toward simplification and automation of the *in-situ* polymerization process for composite laminates. By depositing the initiation functional group onto the reinforcement, infusion of a single stream of inert monomer solution is possible. The technique simplifies the processing equipment required and reduces the risk of contamination. Two separate methodologies derived from a silane and a diisocyanate respectively were investigated. The soluble diisocyanate (SDI) method was used to successfully demonstrate the single-stream processing technique. Glass fiber surface-initiated polymerization was also demonstrated. The findings represent the first steps toward a new processing paradigm of APA-6 composites.

## INTRODUCTION

Thermoplastic composites possess mechanical properties that are optimal for current automotive, transportation, and energy industry needs. A thermoplastic composite with high specific properties of strength and stiffness, end-of-life recyclability, facile reparability, impact energy absorption, and good vibration damping must also be rapidly producible. The preceding requirements are best met when the reinforcing phase consists of continuous fibers in a near-net shape with minimal processing steps. The liquid molding of anionic polyamide 6 (APA-6) laminates has proved to be one of very few processes that can meet all requirements at once as studied by several authors.<sup>1-4</sup>

Liquid molding of thermoplastic composites is possible when the polymer is formed *in-situ*. The technology has tremendous potential, yet the technique has only achieved limited industrial adoption. Current applications are limited to continuous carbon fiber reinforced polyamide-12 tapes<sup>5</sup> and glass fiber reinforced polyamide-6 brake pedals.<sup>6</sup> Wide-scale industrial adoption of APA-6 processing has been met with obstacles related to the stringent processing conditions of temperature, chemical activity, and contamination.

One significant challenge of *in-situ* polymerized anionic polyamide-6 (APA-6) laminates is the reactivity of the monomer stream. Typically, two separate monomer solutions are prepared. One stream contains a small concentration of chemical activator, produced when the monomer, *ε-caprolactam*, is reacted with an alkali metal or similar species. The other stream contains a small concentration of initiator to start anionic ring-opening polymerization. When the two solutions are combined and heated above the reaction temperature of approximately 150 °C, polymerization proceeds quickly. Typical processing windows can range from several minutes to several seconds. Once mixed, the induction time, the period of low solution viscosity appropriate for infusion, is limited, and excess monomer must be purged from the system. The gelation issue can be solved using a sophisticated metering system and mix head, which adds to the capital cost of production. The goal of the following work is to eliminate the difficulties in processing and equipment complexity of a two-stream system. By depositing the initiation species onto the reinforcement preform, a single stream of activated monomer may be used. Complex metering equipment becomes unnecessary. Successful application of the technology has widespread implications for developing a new processing paradigm for

rapid reaction injection molding (RRIM) and new markets of continuous APA-6 products.

For reinforcements with weak interaction with thermoplastics, such as glass fibers, sizing greatly improves the mechanical performance. Typical sizing chemistries for bonding glass to amides have amine groups that interact with the matrix through secondary bonds. Improved matrix adhesion and moisture resistance were demonstrated by Goettler and Otaigbe with the use of *γ-aminopropyltriethoxysilane*.<sup>1,7</sup> Surface initiated polymerization, however, has the added advantage of a stronger covalent bond with the reinforcement which could prove to be more effective.

With a similar processing goal in mind, Yan and Yang reacted hydroxylated multi-walled carbon nanotubes (MWCNTs) with *toluene diisocyanate* (TDI) to initiate surface polymerization.<sup>8</sup> The effect was a more homogeneously dispersed composite. Yan and Yang did not seize the opportunity to use the nanotubes solely to initiate polymerization. In another study by Yang et al., isocyanate functionalized MWCNTs were confirmed to be APA-6 initiation sites.<sup>9</sup> Both studies demonstrated the viability of chemical sizing with APA-6 initiation capability.

When considering the length scales of typical woven fabric reinforcement, surface initiation alone does not provide a sufficiently uniform distribution of starting points for complete polymerization of the matrix. To completely convert all monomer into polymer in a uniform fashion, the initiation species must also be capable of diffusing into the monomer solution. Typical cast nylon chemistries are based on this principle, with initiator reagents pre-dissolved in monomer pellets that are melted and pre-mixed with the activated monomer solution. To completely isolate the initiator and place it

temporarily onto the fiber reinforcement, the initiation chemistry must be resistant to deactivation in the ambient air.

The variety of chemical initiators available for the anionic polymerization of polyamides is diverse.<sup>10</sup> The subset of initiators based on diisocyanates was chosen for this study due to its relatively high effectiveness.<sup>11, 12</sup> Also, isocyanates are easily 'blocked' with other chemical species to inhibit their reactivity prior to use. Isocyanates blocked with  $\epsilon$ -caprolactam, for example, are resistant to hydrolysis by ambient moisture, which prevents the formation of unfavorable chemical groups when exposed to air. Isocyanates blocked with  $\epsilon$ -caprolactam are coincidentally an initiation moiety for APA-6, which can be seen in Figure 1. When combined with a silane denoted as "R" in the figure, the initiator becomes a glass fiber sizing.

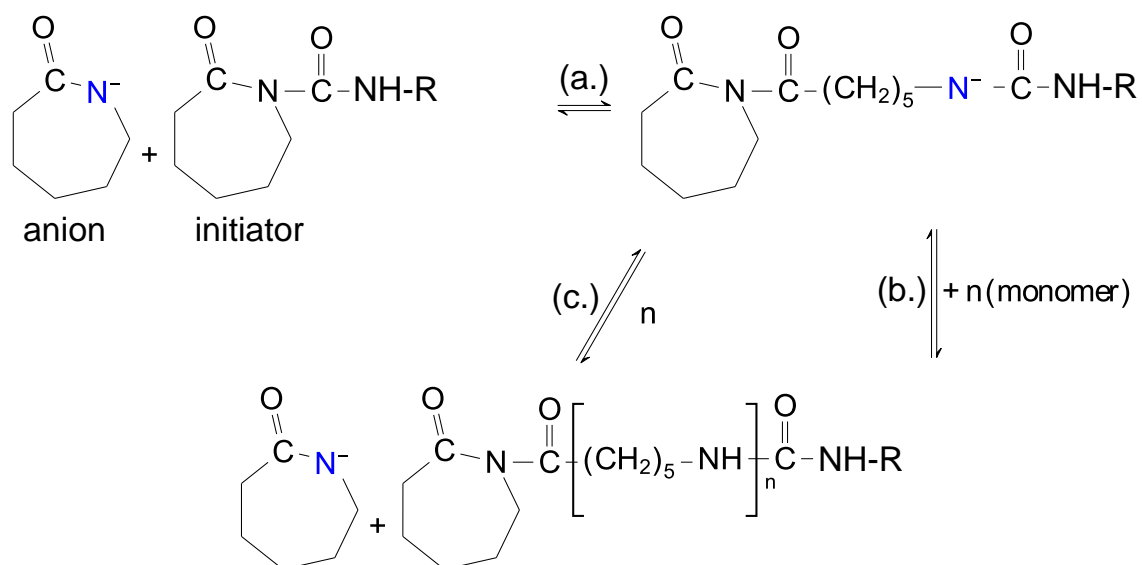


Figure 1. The "co-activated" anionic initiation and propagation reaction steps. An anion reacts with the initiator followed by a ring-opening step. The regenerated anion reacts with the  $\epsilon$ -caprolactam monomer and the ring-opening process continues.

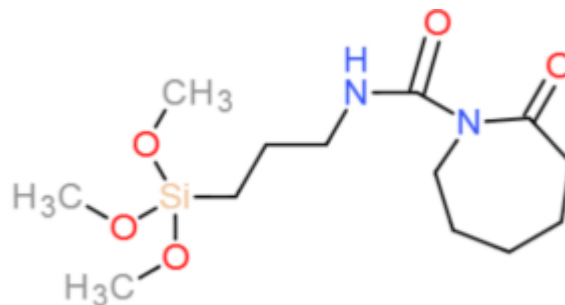


Figure 2. The APA-6 initiating silane molecule showing functionality for both glass fiber and APA (CAS: 106996-32-1).

## MATERIALS

E-glass fabric (588 g m<sup>-2</sup> plain weave with proprietary sizing) was provided by PPG Industries Inc. A commercially available anionic polyamide-6 (APA-6) system consisting of an activator, *caprolactam magnesium bromide* (Nyrim C1); an initiator, *hexamethylene-1,6-dicarba-moylcaprolactam* (Bruggolen C20); and the monomer,  $\epsilon$ -*caprolactam* was supplied by Brüggemann Chemical. The diisocyanate chosen for the work was *4,4'-methylene diphenyl diisocyanate* 98% (MDI) from Acros Organics. The experimental fiber sizing initiator was *N-[5-(trimethoxysilyl)-2-aza-1-oxopentyl]caprolactam* 95%, CAS 106996-32-1, abbreviated hereafter as (MOSCL), from Gelest Inc.. Lab purity *methanol* was from Fisher Chemical. The solvent used for synthesis of the soluble initiator was *toluene* 99.5% from Fisher Chemical. The *toluene* was dried with 3A molecular sieves prior to use. All other materials were used as-received. Distilled water was produced using a common lab distiller. Relevant molecular weight information is provided in Table 1.

Table 1. Useful data to calculate concentrations required for a target APA-6 molecular weight of 53,000 g mol<sup>-1</sup>.

Chemical	Abbreviation	Molecular Weight
<i>N</i> -[5-(trimethoxysilyl)-2-aza-1-oxopentyl]caprolactam	MOSCL	318.44 g mol <sup>-1</sup>
<i>N,N'</i> -(Methylenedi- <i>p</i> -phenylene)bis[hexahydro-2-oxo-1 <i>H</i> -azepine-1-carboxamide]	SDI	476.58 g mol <sup>-1</sup>
4,4'-methylene diphenyl diisocyanate	MDI	250.25 g mol <sup>-1</sup>
$\epsilon$ -caprolactam	-	113.16 g mol <sup>-1</sup>

## PROCESSING

### CALCULATION OF STOICHIOMETRIC QUANTITIES

The final goal of the process is to produce APA-6 with a number average molecular weight  $M_n$  of 53,000 g mol<sup>-1</sup> to closely match the baseline Bruggolen resin system which had been studied previously.<sup>13, 14</sup> Molecular weight is calculated from the degree of polymerization, DP, and the mass of the monomer as follows:

$$M_w = f \cdot DP \cdot M_{\text{monomer}} \quad (1)$$

The functionality  $f$  of the initiator must be recognized to accurately include the proper content of initiator. MOSCL has a functionality of 1 in terms of the number of APA-6 initiation groups. Using the details in Table 1 to determine the required degree of polymerization, it was found that the ratio of  $\epsilon$ -caprolactam to initiator is 468:1. Thus each growing chain will have a nominal molecular weight of 53,000 g mol<sup>-1</sup>.

$$DP = 468 = \frac{M_{\epsilon\text{-caprolactam}}}{M_{\text{MOSCL}}} \therefore M_{\text{MOSCL}} = \frac{1}{DP} = 2.137 \times 10^{-3} \text{ mol.} \quad (2)$$

The mass fraction  $X_{\text{MOSCL}}$  of MOSCL must account for the molar mass of each species  $W_i$  as well as the functionality  $f$  as:

$$X_{\text{MOSCL}} = \frac{1/f(M_{\text{MOSCL}})W_{\text{MOSCL}}}{W_{\varepsilon\text{-caprolactam}}} = \frac{1/1(2.137 \times 10^{-3})318.44}{113.16} = 6.0 \times 10^{-3} \text{ g/g} . \quad (3)$$

Thus, the mass fraction of MOSCL required for polymerization is 0.60 wt. % to obtain the comparable molecular weight of 53,000 g mol<sup>-1</sup>. A similar calculation is done for the MDI-based initiator. MDI has a functionality of 2, with two NCO groups per molecule. Using the details in Table 1 to determine the required degree of polymerization, we find that the ratio of  $\varepsilon$ -caprolactam to NCO is 234 for a difunctional initiator. Each growing chain will have a molecular weight of 26,500 g mol<sup>-1</sup> with a total molecule weight of 53,000 g mol<sup>-1</sup>. The baseline initiator, Bruggolen C20P, also has a functionality of 2. The molar ratio of NCO to  $\varepsilon$ -caprolactam is equivalent to the DP and is calculated:

$$\text{DP} = 234 = \frac{M_{\varepsilon\text{-caprolactam}}}{M_{\text{NCO}}} \therefore M_{\text{NCO}} = \frac{1}{\text{DP}} = 4.27 \times 10^{-3} \text{ mol} . \quad (4)$$

The mass fraction  $X_{\text{SDI}}$  of SDI must account for the molar mass of each species  $W_i$  as well as the functionality  $f$  as:

$$X_{\text{MDI}} = \frac{1/f(M_{\text{NCO}})W_{\text{SDI}}}{W_{\varepsilon\text{-caprolactam}}} = \frac{1/2(4.27 \times 10^{-3})476.58}{113.16} = 8.99 \times 10^{-3} \text{ g/g} . \quad (5)$$

Thus, the concentration of SDI required is 0.899 wt. % to obtain the comparable polymer molecular weight of 53,000 g mol<sup>-1</sup>.

#### SYNTHESIS OF SOLUBLE DIISOCYANATE INITIATOR (SDI)

A 1L two-neck round-bottom flask equipped with a reflux condenser was rinsed with organic solvents and flame dried under high vacuum. The reaction vessel was then moved to an oxygen-free, dry nitrogen glove box where 5.0 g of solid MDI, 10.0 g of  $\varepsilon$ -caprolactam, and 500 mL of anhydrous toluene were added. The molar ratio of  $\varepsilon$ -caprolactam to NCO was in excess of 2:1, such that the self-reaction of MDI was

minimized. The flask was removed from the glove box under positive nitrogen pressure and placed into an oil bath. The mixture was then heated to 80 °C and was maintained at this temperature under positive nitrogen pressure for approximately 38 hours. Figure 3 shows the Fourier transform infrared (FTIR) spectrum recorded on a Bruker ALPHA FT-IR Spectrometer in attenuated total reflectance (ATR) mode of an aliquot taken at 0 hours (grey) and 28 hours (black). The black spectrum in Figure 3 shows that the NCO peak (2270  $\text{cm}^{-1}$ ) was no longer detected after 28 hours. The reaction was continued for an additional 10 hours. The peak at 1713  $\text{cm}^{-1}$  that appeared after 28 hours corresponds to the newly formed carbonyl peak between  $\epsilon$ -caprolactam and the isocyanate group.

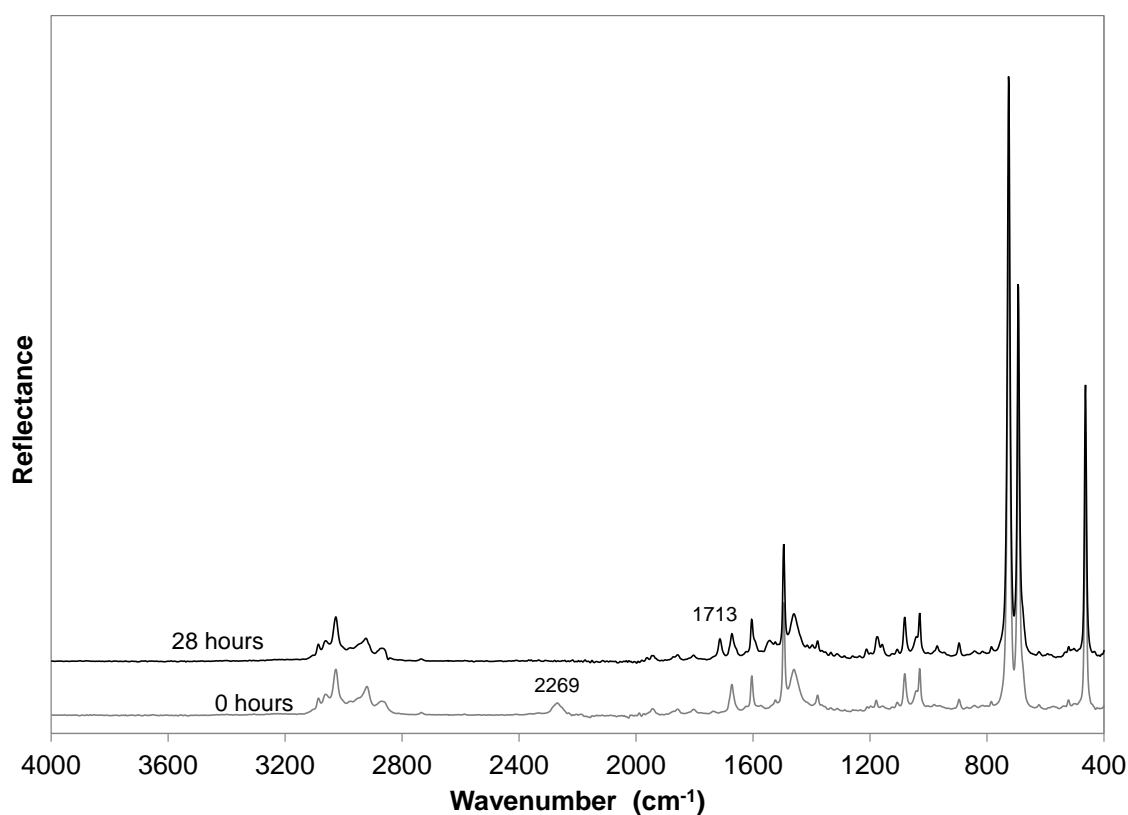


Figure 3. FTIR spectra of the solution over 28 hours of reaction showing a complete disappearance of the NCO peak at wavenumber 2269  $\text{cm}^{-1}$ . A new C=O peak appeared at 1713  $\text{cm}^{-1}$  when the NCO reacted with the  $\epsilon$ -caprolactam.

After 38 hours the solvent was reduced to 10 % of its original volume via rotary evaporation, at which time a white precipitate appeared. The solid was vacuum filtered through a 300 mL sintered glass funnel and washed three times with *methanol*. The remaining solution was decanted to remove the excess  $\epsilon$ -*caprolactam*. Subsequent proton nuclear magnetic resonance ( $^1\text{H}$  NMR) of the white fluffy solid confirmed the presence of the amine proton, indicated by the far downfield broad singlet at 11.456 ppm shown in Figure 6. The newly formed initiator, the structure of which is shown in overlay in Figure 6, was then allowed to stir in methanol for an additional 48 hours to remove any remaining  $\epsilon$ -*caprolactam*. For a final purification step to remove any remaining  $\epsilon$ -*caprolactam*, the filtered white powder was re-dissolved in *toluene* and diluted with *methanol* 5:1. The dissolved SDI crystallized out of solution and was collected after 24 hours and dried in vacuum at 120 °C overnight.



Figure 4. (Left) Precipitate formed from the solution by transferring the concentrated products into *methanol* and filtering. (Right) Precipitate following crystallization from saturated solution in *methanol*. Images are not to scale

A comparison of the as-produced and crystallized SDI was done via differential scanning calorimetry (DSC) using a TA Instruments DSC and a TA Q100 Controller equipped with a refrigerated cooling system (RCS). The heating rate was a standard ramp of  $10\text{ }^{\circ}\text{C min}^{-1}$ . The plot is shown in Figure 5. The DSC curve confirmed that the crystallized SDI was indeed crystalline and thus of a higher purity than the as-produced amorphous SDI. Additionally, the de-blocking temperature was determined to be  $184\text{ }^{\circ}\text{C}$  and well above typical RTM mold temperature range of  $150\text{--}160\text{ }^{\circ}\text{C}$ .

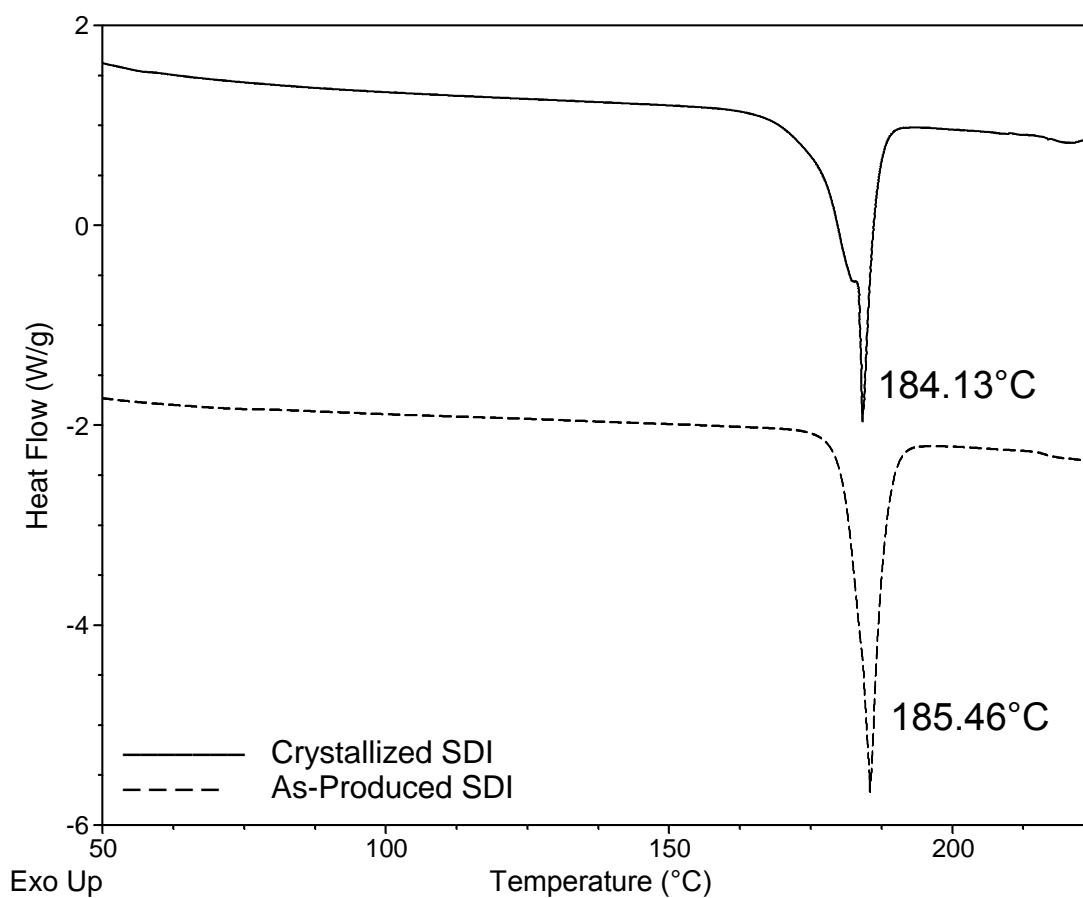


Figure 5. Crystallized SDI (solid) and as-produced SDI (dashed) DSC curves shown offset. The crystalline SDI exhibited a melting peak coinciding with the  $\epsilon$ -caprolactam de-blocking reaction which occurred at  $184\text{ }^{\circ}\text{C}$ . The as-produced SDI was amorphous and only showed a de-blocking reaction at  $185\text{ }^{\circ}\text{C}$ . The typical pre-drying temperature range associated with the APA-6 reaction of  $150\text{--}160\text{ }^{\circ}\text{C}$  was confirmed to be safe for the SDI.

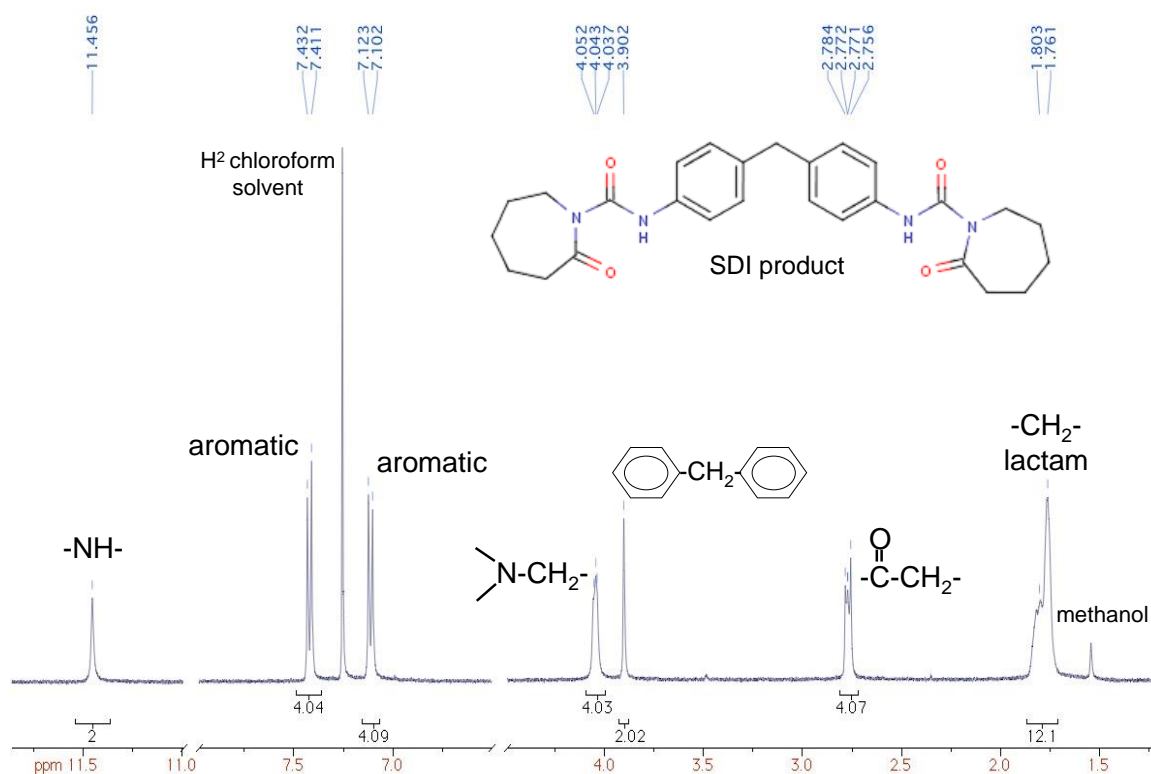


Figure 6. Proton nuclear magnetic resonance (NMR) output of the as-produced precipitate. The integration label below each peak corresponds with the number of protons of each bond type that matches the assumed structure exactly. The sum of the normalized integration adds to 32, which is the number of protons in the SDI structure. Excess unreacted  $\epsilon$ -caprolactam, for example, would have offset the lactam integration from 12 protons. Thus, the crystallized product was determined to be mostly pure.

## GLASS FABRIC PRE-TREATMENT

Woven E-glass was heated to 600 °C for 1 hour to remove any organic sizing present on the fibers. Although heating above 400 °C most certainly degraded the mechanical performance of the fibers, 600 °C was determined to be necessary to completely remove any trace organics, as shown in a thermogravimetric analysis (TGA) plot in Figure 7.

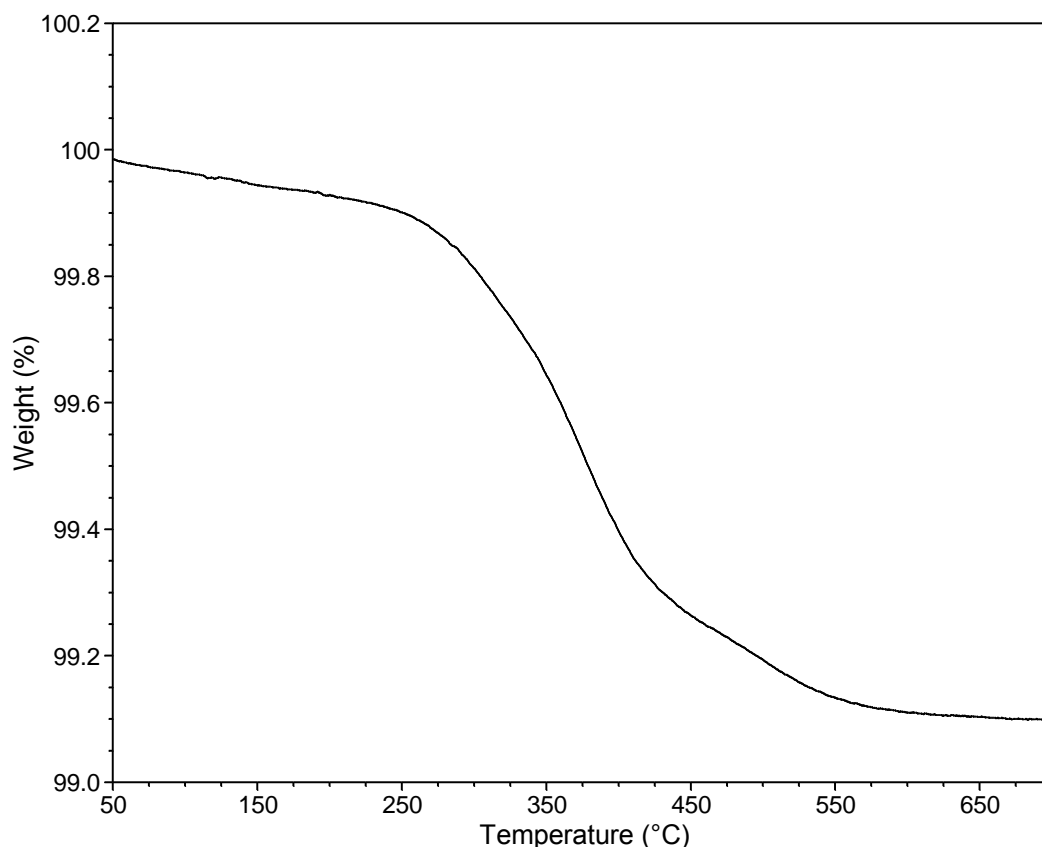


Figure 7. Thermogravimetric determination of minimum temperature required to completely remove organic sizing from test E-glass fabric.

#### INCORPORATION OF SDI ONTO FIBER PREFORM

The appropriate number of glass fabric layers were cut and weighed. The stoichiometric quantity of initiator was calculated based on a fiber fraction of 60 wt. % using Equation (5). For 4 layers of glass fabric, 1.92 g of SDI was combined with 300 ml of *toluene*. The solution was gently heated and stirred using a magnetic stir bar and hotplate until the solution became clear. The glass fabric layers were placed into a flat bottom tray and the solution was poured over the top. Individual layers were removed one at a time and placed onto wire mesh to dry in air in a fume-hood. The fabric preform after SDI incorporation is shown in Figure 8.

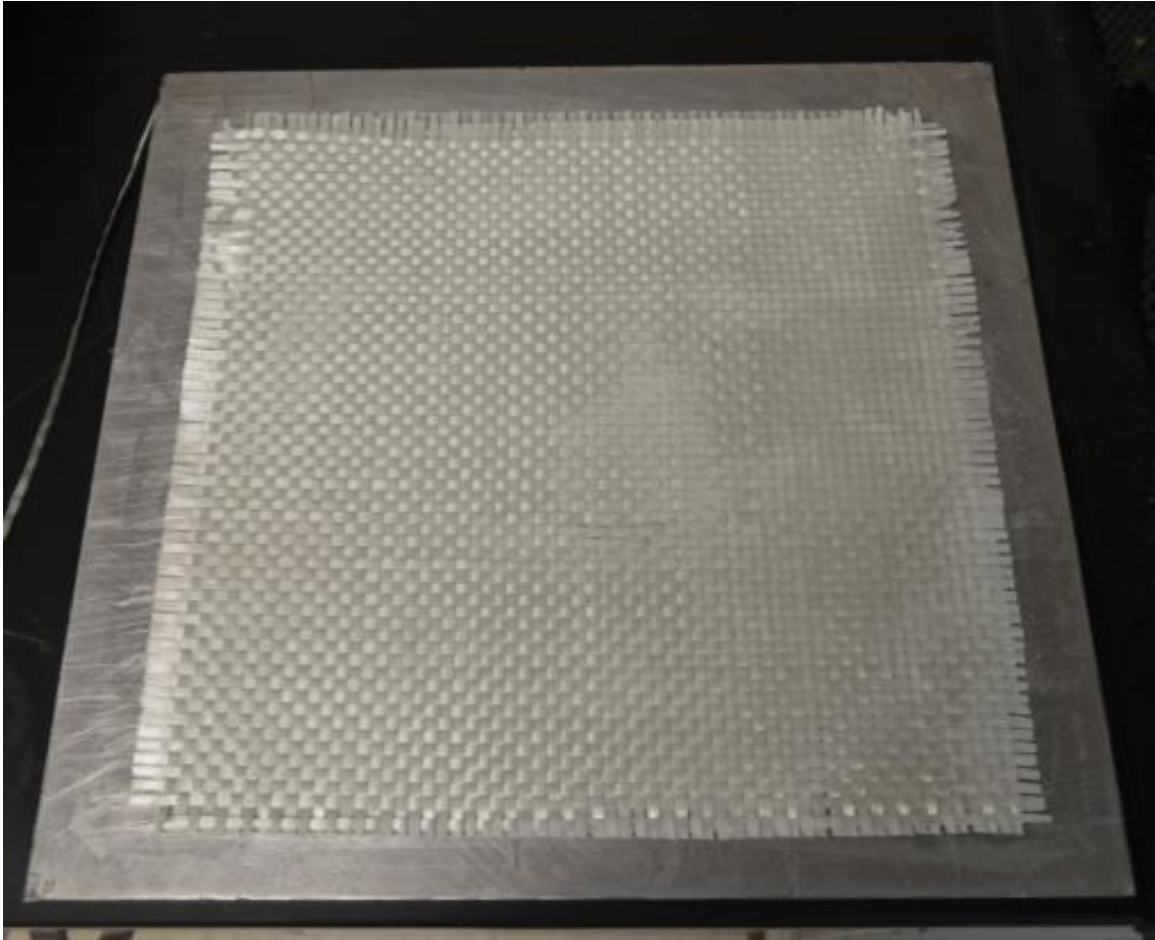


Figure 8. Appearance of glass fiber fabric after incorporation of the soluble diisocyanate initiator (SDI). The glass fabric was approximately 12 inches per side.

#### PROCESSING UN-SIZED SDI TEST PANEL

Once dried, the preform was placed into a resin transfer mold (RTM) and sealed under vacuum. The mold was heated to 160 °C in a circulating air oven and held for 2 hours to equilibrate in temperature. The infusion was done with a 5 % Nyrin® C1 by weight of  $\epsilon$ -caprolactam activated monomer solution at 120 °C prepared under dry nitrogen. After infusion, the sample was held at temperature for 60 minutes. Once polymerization was ensured, the entire RTM was removed from the convection oven to cool. The as-produced un-sized SDI single stream panel is shown in Figure 9.

Although the flow was not injected under high pressure, the degree of SDI wash due to the incoming monomer solution was inferred by the approximate degree of conversion of the matrix polymer. Square samples 19 mm on a side were cut with a band saw from the panel in a line directly through the center along the fiber 0° direction. The samples were weighed immediately to avoid any additional mass caused by ambient moisture absorption. The squares were placed in hot distilled water at approximately 60 °C and allowed to soak for 72 hours. The samples were then removed from the water and dried in a vacuum oven at 130 °C for 8 hours. The samples were weighed again, and the weight loss and remaining mass were recorded. The samples were then ‘burned-off’ in a furnace at 550 °C for 1 hr. to calculate the weight fraction of the fiber. The degree of conversion was calculated and is shown in Figure 10. The SDI washout and dilution by the incoming activated monomer stream is apparent by the dip in conversion at the center of the panel. However, nearly complete polymerization was observed along the perimeter of the panel. Polymerization was verified via DSC analysis as shown in Figure 11.

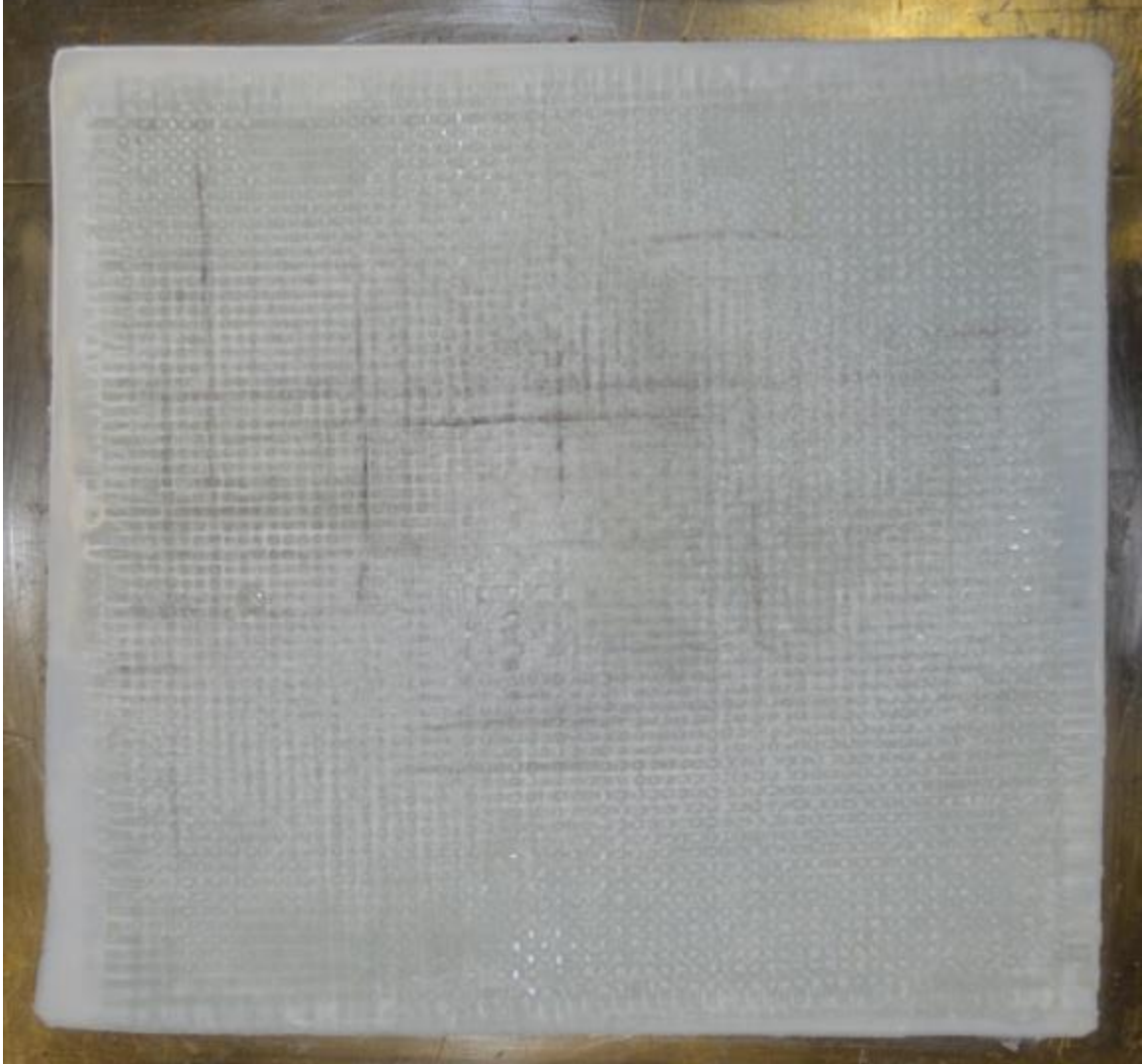


Figure 9. The as-produced un-sized SDI single-stream panel. Brown line discolorations were caused by sizing residue left over from the fabric pre-treatment. The otherwise non-uniform coloration was likely a result of an inhomogeneous concentration of SDI after infusion. The panel was filled from the center outward.

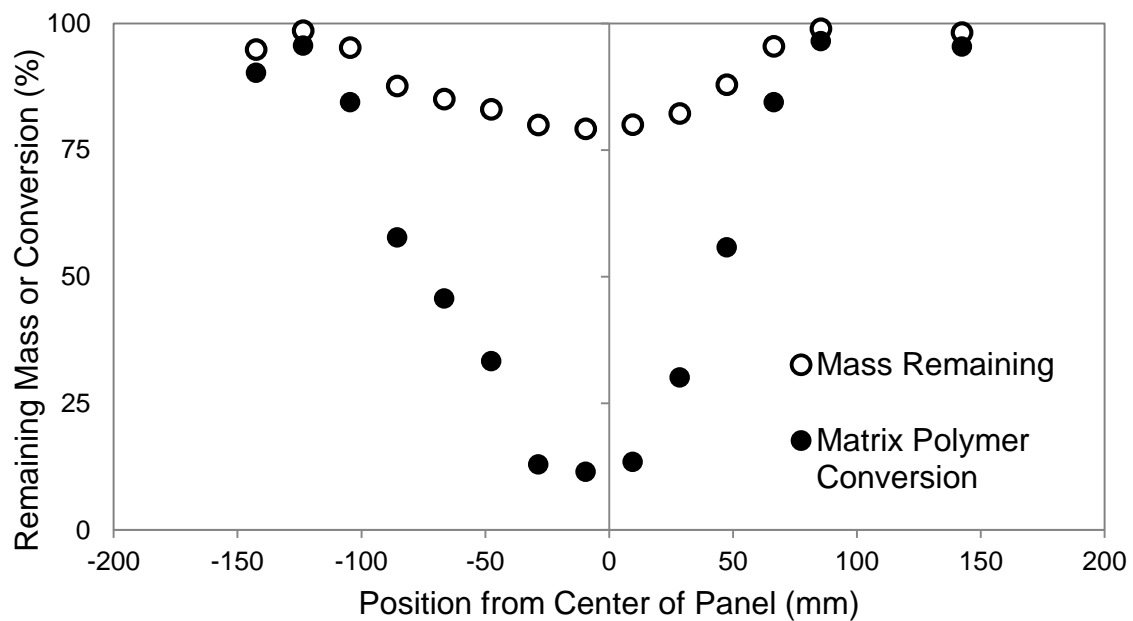


Figure 10. Remaining mass after soaking in distilled water (open circle). Approximate matrix polymer conversion (filled circle) with respect to position from the centerline of the panel along the  $0^\circ$  direction was calculated assuming a fiber content of 60 wt. %.

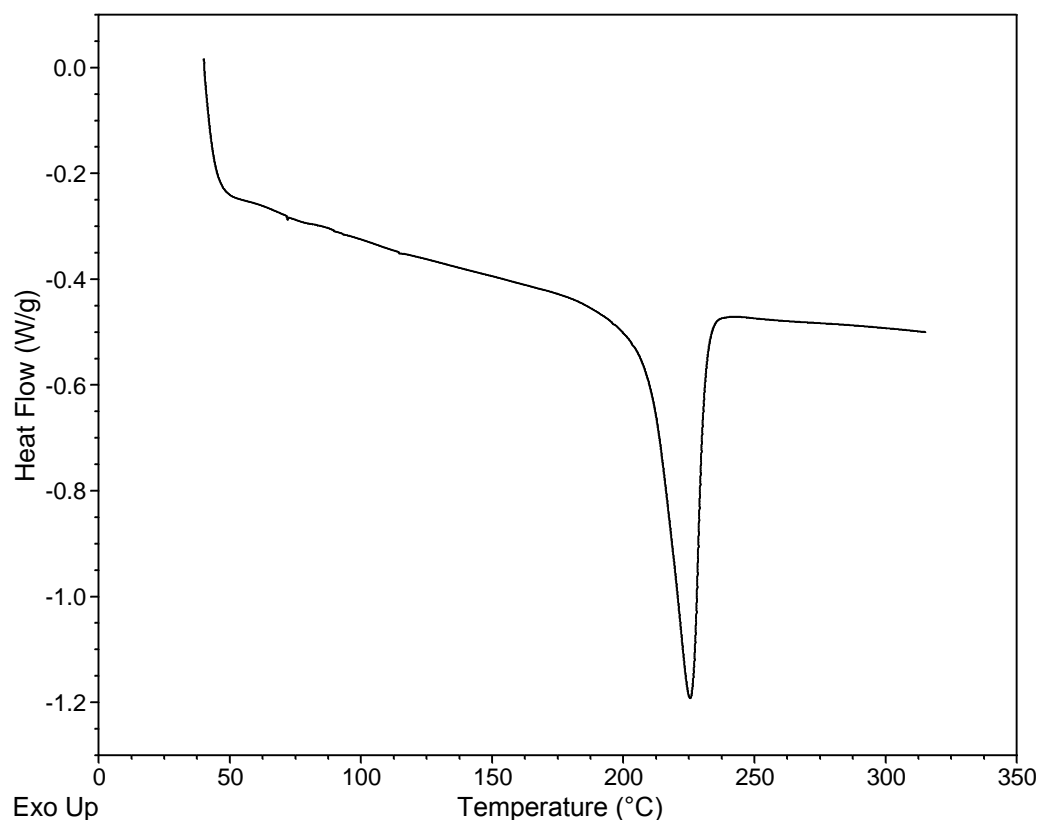


Figure 11. A DSC curve of a sample from the perimeter of the un-sized SDI panel. A large endothermic peak characteristic of APA-6 is shown near 225 °C. For incomplete polymerization, residual monomer would appear around 68 °C and/or the endothermic melting peak would become broad. The analysis confirms that near the perimeter of the panel, polymerization was successful.

### SILANIZATION PROCEDURE

The procedure for silanization of the glass fabric used in the study was modeled after work done by Stenger et al.<sup>15</sup> and Hickman,<sup>16</sup> omitting the initial cleaning steps to instead use the fabric as-pyrolyzed. A solution was prepared with each concentration on a by-volume basis. Lab grade *methanol* (94 %) was combined with 5.0 % distilled water and 1.0 % MOSCL. A stoichiometric quantity of solution was combined with woven glass fabric based on a nominal weight fraction of 60 % fiber. The glass fabric was placed in a large flat basin and covered with the solution. The silanization was allowed to continue for 30 minutes to ensure even distribution throughout the fiber tows.

Afterward, the fabric was removed from the solution and rinsed once in *methanol*. The fabric was then left to dry in air in a fume hood.

### SURFACE CHARACTERIZATION

The effectiveness of the MOSCL sizing as a surface polymerization initiator was tested using a similar procedure to the single-stream process but with a small fabric tow sample. A short section of MOSCL silanized glass tow was placed into a glass vial and dried under vacuum at 130 °C for an hour. The furnace was back-filled with air first passed through a canister of silica gel. The furnace was opened and the glass vial was quickly capped. Approximately 10 g of  $\epsilon$ -*caprolactam* and 0.5 g of Bruggolen C1, both in dry flake form, were added to the vial in a dry glove box. The vial was sealed and placed into a convection oven at 165 °C for 2 hours and removed. The content of the vial was dissolved in water to remove the unreacted  $\epsilon$ -*caprolactam*. The fiber tow was recovered and placed in acetone and further washed in a Cole-Parmer 8852 ultrasonic cleaner for 30 minutes. The fiber tow was then removed from the acetone and dried in a vacuum furnace at 130 °C for 1 hour.

Surface characterization was done by comparing the as-pyrolyzed glass and the MOSCL silanized glass fibers to the surface polymerization sample. SEM images were acquired with a Quanta FEG 650 Scanning Electron Microscope under low vacuum. A low pressure of water vapor, approximately 80 Pa, was used to create the conduction path ordinarily provided by Au-Pd coating. A gaseous secondary electron detector (GSED) was used. An accelerating voltage of 5kV was used for imaging. A comparison of the surface characteristics of the as-pyrolyzed, MOSCL sized, and surface polymerized APA-6 fiber is shown in Figure 12. The fibers appeared to be clean after both the pyrolysis

and after MOSCL sizing. Not until after surface polymerization was any noticeable change in surface roughness observed. The content of polymer was minimal, but present.

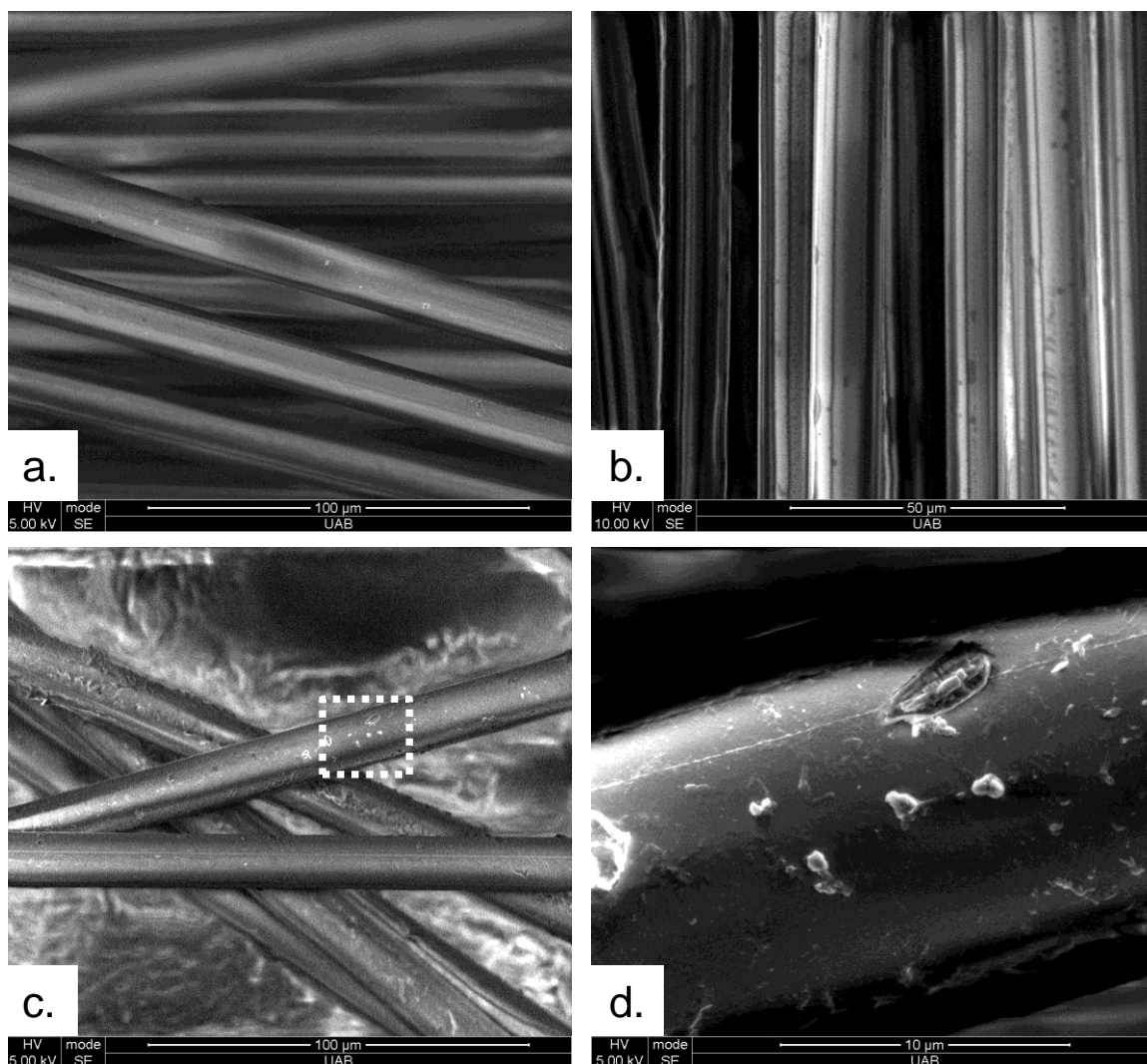


Figure 12. (a.) E-glass fibers are shown in the as-pyrolyzed condition. (b.) The pyrolyzed fiber is shown after MOSCL silanization. (c.) The fibers after surface-initiated polymerization of APA-6 are shown with an area of interest within the white dashed rectangle. (d.) An expanded view of the fiber from within the rectangle in (c.). The fiber surface shows evidence of polymerization occurring at several locations rather than a continuous monolayer of polymer.

## CONCLUSIONS

The synthesis of SDI established a baseline process by which other isocyanate-derived APA-6 initiators may be produced. Further investigations of various other forms

of isocyanates could be studied to determine the advantages and disadvantages of each. The source of initiation species besides isocyanates could be investigated.

This work demonstrated the viability of the single-stream processing technique for APA-6. To the knowledge of the authors, the work represents the only such instance of the single-stream APA-6 process.

During the infusion process, the SDI initiator was washed by the incoming monomer stream. An undesirable concentration gradient of initiators resulted in incomplete conversion at the center of the panel. Despite the washing effect, APA-6 was produced around the perimeter of the sample panel. A more detailed study of the method by which the initiator is applied to the fiber preform, or the chemical characteristics of alternative initiator chemistry could alleviate the wash-out problem.

Glass fiber surface-initiated polymerization of APA-6 was demonstrated using the MOSCL sizing. A relatively small quantity of polymer was observed compared to the expected content from the stoichiometry of the starting materials. The low content could have been the result of the pyrolysis pre-treatment of the glass. Application of MOSCL during glass fiber production should be done to give a more realistic feasibility of the performance of the sizing. Further study to determine the degree to which the MOSCL sizing affects the interface between the glass fiber and the matrix needs to be studied.

#### ACKNOWLEDGEMENTS

This work would not have been possible without the gracious support of Dr. Gary Gray and Justin Martin from the UAB Department of Chemistry and the use of their facilities and expertise. Support from PPG Industries Inc. in supplying fabric materials and technical advice is also greatly appreciated. Funding provided by the ALEPSCoR

Graduate Research Scholars Program Rounds 7 & 8 was instrumental. Special thanks go to the UAB SEM Laboratory for help with acquiring micrographs.

#### REFERENCES

1. Goettler LA and Neff WJ. Mechanical performance of various nylon 6 composites formed by in-situ polymerization of caprolactam, *Polym Composite* 1986; 7: 383-94.
2. Otaigbe JU and Harland WG. Studies in the properties of nylon 6–glass fiber composites, *Journal of Applied Polymer Science* 1988; 36: 165-75.
3. Van Rijswijk K, Bersee HEN, Beukers A, Picken SJ and van Geenen AA. Optimisation of anionic polyamide-6 for vacuum infusion of thermoplastic composites: Influence of polymerisation temperature on matrix properties, *Polymer Testing* 2006; 25: 392-404.
4. Pillay S, Vaidya UK and Janowski GM. Liquid Molding of Carbon Fabric-reinforced Nylon Matrix Composite Laminates, *Journal of Thermoplastic Composite Materials* 2005; 18: 509-27.
5. Moller E, Bailey DM and Berghahn M. Camisma -- new composites for lighter cars. In: *SAMPE tech* (eds Charleston, SC, 22-25 October, 2012).
6. Bäck G, Egger P., Berg, L. F. Combining Polymerization and Molding within a Single Machine. *Kunststoffe International*. Kunststoffe international, 2012, p. 102-5.
7. Otaigbe JU. Effect of coupling agent and absorbed moisture on the tensile properties of a thermoplastic RRIM composite, *Journal of Applied Polymer Science* 1992; 45: 1213-21.
8. Yan D and Yang G. Synthesis and properties of homogeneously dispersed polyamide 6/MWNTs nanocomposites via simultaneous in situ anionic ring-opening polymerization and compatibilization, *Journal of Applied Polymer Science* 2009; 112: 3620-6.
9. Yang M, Gao Y, Li H and Adronov A. Functionalization of multiwalled carbon nanotubes with polyamide 6 by anionic ring-opening polymerization, *Carbon* 2007; 45: 2327-33.
10. Kohan MI. *SPE monographs : nylon plastics*. New York: John Wiley & Sons, Inc., 1973, 683 p.
11. Wichterle O. On caprolactam polymerization, *Die Makromolekulare Chemie* 1960; 35: 174-82.

12. Allport DC, Brenner KS, Chapman JF, et al. Supporting Sciences. In: Allport DC, Gilbert DS and Outterside SM, (eds.). *MDI and TDI: Safety, Health and the Environment: a source book and practical guide*. New York: John Wiley & Sons, Ltd, 2003, pp.277-430.
13. Barfknecht P, Pillay SB and Vaidya UK. Effect of nanographite on thermal properties of liquid molded polyamide-6 laminates. In: *19th International Conference on Composite Materials* (eds Hoa SV and Hubert P), Montréal, Canada, July 28, - August, 2, 2013, pp.463-71. Curran Associates, Inc.
14. Barfknecht P, Pillay SB and Vaidya UK. Multiscale anionic polyamide-6 composites with selective incorporation of nanoparticles. In: *SAMPE Tech* Wichita, KS, October 21-24, 2013.
15. Stenger DA, Georger JH, Dulcey CS, et al. Coplanar molecular assemblies of amino- and perfluorinated alkylsilanes: characterization and geometric definition of mammalian cell adhesion and growth, *Journal of the American Chemical Society* 1992; 114: 8435-42.
16. Hickman JJ, Bhatia SK, Quong JN, et al. Rational pattern design for invitro cellular networks using surface photochemistry, *Journal of Vacuum Science & Technology A* 1994; 12: 607-16.

FUNCTIONALIZED NANOGRAFITE OXIDE PLATELETS FOR ANIONIC  
POLYAMIDE-6 INITIATION FROM BALL-MILLED GRAPHITE

by

PETER W. BARFKNECHT, JUSTIN MARTIN, BRIAN (SELVUM) PILLAY, UDAY  
K. VAIDYA, AND GARY M. GRAY

In preparation for *Carbon*

Format adapted for dissertation

## ABSTRACT

The growing interest of thermoplastic nanocomposites necessitates the development of industrially-scalable processes to create functionalized nanoparticles. In the following work, a planetary ball-mill process was modeled and optimized for the exfoliation of graphite into nanoplatelets. Nanographite oxide platelets (NGOPs) were successfully produced by reacting bulk graphite flake GR with *carbon dioxide* gas. Platelets were observed with lateral dimensions  $< 1 \mu\text{m}$  and thicknesses  $\ll 1 \mu\text{m}$ . X-ray diffractometry confirmed the NGOPs to be graphitic with no intercalation. A functionalization reaction to covalently bond anionic *polyamide-6* (APA-6) initiator chemistry to the NGOPs was identified. The presence of the initiator was inferred via thermogravimetric analysis (TGA), nuclear magnetic resonance (NMR), and Fourier-transform infrared spectroscopy (FTIR). However, the functionalized nanographite platelets, (FNGPs) were unable to initiate surface polymerization of APA-6, possibly due to steric hindrance of the initiator being adsorbed to the graphite surface rather than covalently bonded and projected outward. A catalyst was identified to improve the carboxyl/diisocyanate functionalization reaction.

## INTRODUCTION

The scale-up of nanoparticle production processes has been a barrier to industrial application of nanocomposites and multiscale composite materials. Candidate processes are only viable if the production rate is high and if the particles have optimal chemical compatibility with the composite matrix. The ever-increasing market of thermoplastic nanocomposites usually requires some form of chemical compatibility for good dispersion and mechanical property enhancement. Recent attention has identified

graphene oxide (GO) as a candidate nanoparticle for a variety of applications. Typically, GO is used due to its C-O-C, C=C, and C-OH defects,<sup>1-3</sup> which provide reaction sites for the addition of functional groups.

The production methods of GO are traditionally chemical treatments based on Staudenmeier's Method<sup>4</sup>, Hummer's method,<sup>5</sup> and other variations such as the Improved Hummer's Method by Marcano.<sup>6</sup> However, to support large-scale markets such as the automotive and transportation industries, the process must be scalable and have a minimal environmental impact. Recently, mechanical alloying techniques have been adapted to produce nanographite oxide platelets (NGOPs) from bulk graphite sources. Yan et al. produced *hydroxylated* NGOPs by reacting graphite with *potassium hydroxide* using a planetary ball-mill in the solid state.<sup>7</sup> Jeon et al. produced NGOPs by reacting graphite with *carbon dioxide*<sup>8</sup> and with other mixtures of gases<sup>9</sup> with a planetary ball mill process.

Although the planetary ball-mill has been shown to be a viable processing technique, commercially available machines may not be specifically optimized for the exfoliation of NGOPs. A process which induces primarily normal impacts between the milling spheres and the vial wall will tend to dynamically fracture the powder into small sizes.<sup>10</sup> For exfoliation of NGOPs from graphite, an oblique impact with a shear fracture is preferred since the lateral dimensions of the platelets are better conserved.

First, this work builds upon kinetic models of planetary ball mill processes by Lu et al.<sup>11</sup> and Chattopadhyay<sup>12</sup> to optimize and build a planetary ball-mill for NGOP production. Second, the NGOPs produced by the custom planetary ball-mill are

characterized. Finally, a technique to produce functionalized NGOPs (FNGPs) with initiator groups for anionic polyamide 6 (APA-6) is carried out and characterized.

#### MODELING MOTION IN A PLANETARY BALL-MILL

A planetary ball mill grinds substances through self-impact between the grinding spheres and through impact of the sphere with the grinding vial wall. The possible kinetic energy of a planetary ball mill is greater than a horizontal ball-mill since the centripetal acceleration directed radially outward from a rotating disc can be several times higher than that of gravity. The resulting particle size and milling time are both significantly reduced.<sup>10</sup>

The grinding action of the mill is achieved by a combination of normal impact and oblique, shearing impact. The design and operating parameters of the mill can be optimized to favor either dominant type of impact. Two thorough mathematical models of the motion of milling spheres within a counter-rotating planetary ball mill were presented by Lu et al.<sup>11</sup> and Chattopadhyay et al.<sup>12</sup> Extensive work predicting the behavior of mechanically alloyed powders using a planetary ball mill was done by Maurice and Courtney and others.<sup>10, 13, 14</sup> Given the basic geometry of the ball-mill, the nature of the impacts occurring within the milling jar may be predicted. The name “planetary” likens the motion of the vial to the motion of a planet orbiting a sun. A schematic of a simplified planetary ball-mill is shown in Figure 1.

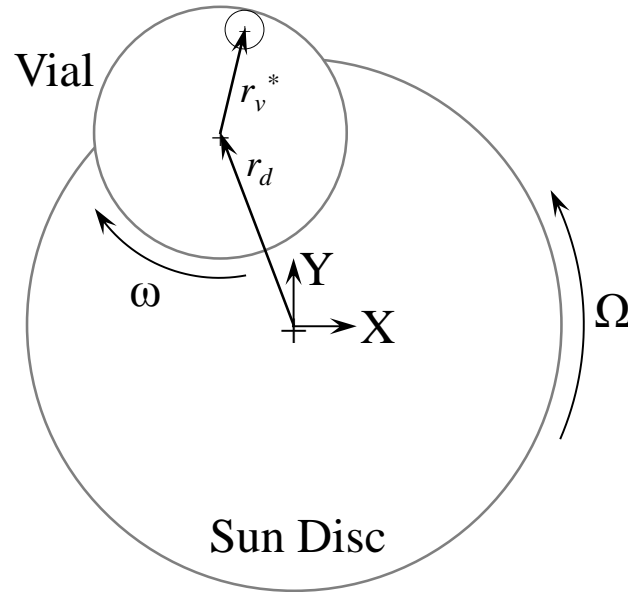


Figure 1. A schematic of the primary dimensions required for kinetic modeling of a planetary ball mill.

The grinding vial is mounted to a “sun disc” which rotates at an angular frequency of  $\Omega$ . The vial is located at a radius  $r_d$  from the center. The vial itself typically counter-rotates at a frequency  $\omega$  at 1.0 – 2.0 times higher than the sun disc frequency. The grinding vial internal radius  $r_v$  and vial angular frequency  $\omega$  are chosen such that the angular acceleration generated by the sun disc is slightly higher than the internal angular acceleration of the vial. Therefore, the grinding spheres temporarily leave the wall of the vial and follow a “D”-shaped path within the vial. The path of the spheres within the vial and the subsequent impact with the vial wall depends primarily on the frequency ratio  $\omega: \Omega$  for a given geometry. A slight reduction of the vial radius  $r_v^*$  from Shen et al. has been made to account for the radius of the milling spheres  $r_s$ . The spheres are still considered as point masses without rotation or slip between the vial walls.

Starting with the milling sphere arbitrarily at the furthest radius from the sun disc center and aligned along the global  $\mathbf{X}$  direction, the position of a single milling sphere is defined in global Cartesian coordinates as follows:

$$X(t) = r_d \cos \Omega t + r_v^* \cos(\Omega - \omega) t, \quad 0 < t < t_1, \quad (1)$$

$$Y(t) = r_d \sin \Omega t + r_v^* \sin(\Omega - \omega) t, \quad 0 < t < t_1. \quad (2)$$

An illustration of the motion of a milling sphere in global coordinates during the time period:  $0 < t < t_2$  is shown in Figure 2. The time  $t_1$  at which the milling ball leaves the vial wall is defined by the following expression:

$$t_1 = \frac{1}{\omega} \cos^{-1} \left( -\frac{r_v^*(\Omega - \omega)^2}{r_d \Omega^2} \right) = \frac{\phi_1}{\omega}. \quad (3)$$

The initial angle swept by the sun disc at  $t = t_1$  is denoted as  $\phi_1$  for simplicity as shown in Figure 2.

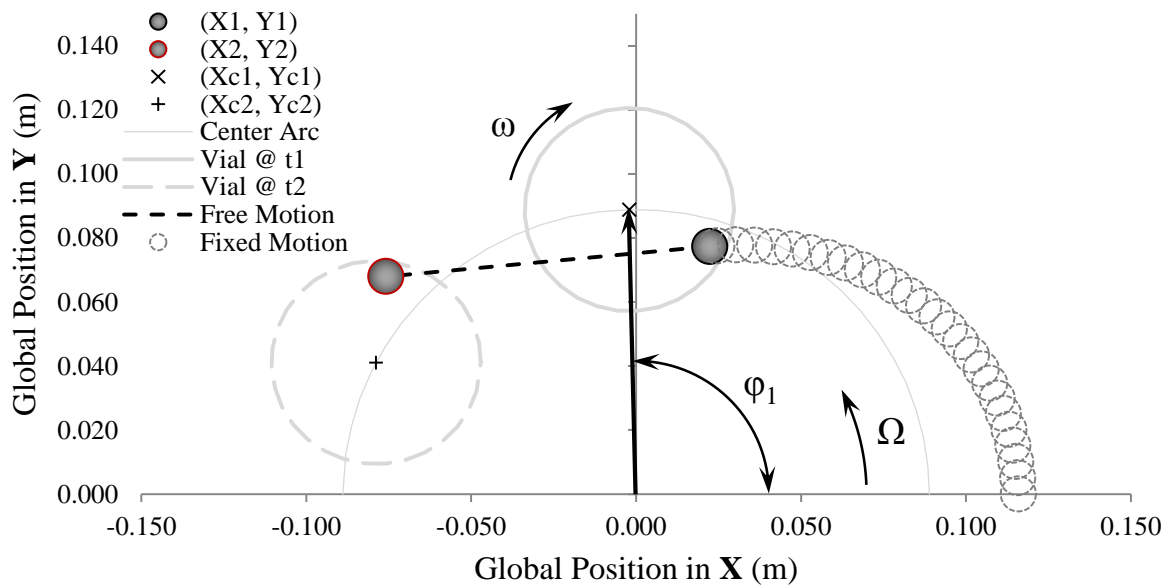


Figure 2. The path of the milling sphere while in contact with the milling vial wall is shown as dashed circles. At the point of take-off, the sphere, shown as shaded grey, follows the direct path along the black dashed line until its impact with the vial.

The global Cartesian coordinates  $(X_c, Y_c)$  of the center of the vial at a given time are useful to calculate the point of collision of the milling sphere with the vial wall and are expressed:

$$X_c(t) = r_d \cos \Omega t, \quad (4)$$

$$Y_c(t) = r_d \sin \Omega t. \quad (5)$$

At time  $t_1$ , the sphere moves in a straight line free from the wall of the vial. The velocity vector components  $v_x$  and  $v_y$  are obtained by simply substituting  $t_1$  into the time derivatives of Equations (1) and (2) as follows:

$$v_x = \dot{X}(t) = -r_d \Omega \sin \Omega t - (\Omega - \omega) r_v^* \sin(\Omega - \omega) t, \quad 0 < t < t_1, \quad (6)$$

$$v_y = \dot{Y}(t) = r_d \Omega \cos \Omega t + (\Omega - \omega) r_v^* \cos(\Omega - \omega) t, \quad 0 < t < t_1. \quad (7)$$

The position of the sphere from its coordinates at  $t = t_1$  or  $(X_1, Y_1)$  to the point of impact with the vial wall  $(X_2, Y_2)$  at  $t = t_2$  for  $t_1 < t < t_2$ , is expressed:

$$X(t) = X_1 + v_x(t - t_1), \quad t_1 < t < t_2 \quad (8)$$

$$Y(t) = Y_1 + v_y(t - t_1), \quad t_1 < t < t_2 \quad (9)$$

The time  $t_2$  at which the radial distance between the vial center and the milling sphere is equal to  $r_v^*$  can be determined by numerically solving Equations (4)-(9) with the following expression:

$$(X_2 - X_{c2})^2 + (Y_2 - Y_{c2})^2 - (X_1 - X_{c1})^2 - (Y_1 - Y_{c1})^2 = 0 \quad (10)$$

For illustrative purposes, a rotational transformation may be done to visualize the path of the milling sphere within the vial. The radial-transverse (**R**, **T**) coordinate axes remain fixed at the center of the milling vial with the radial direction **R** aligned with the radius of the sun disc  $r_d$ . The view would be analogous to observing the Earth from above the North Pole with the sun always directly behind the observer, although in this case, the Earth would be spinning in the opposite direction. The coordinate axes are

illustrated in Figure 3. To transform a global coordinate to the radial-transverse coordinates, a rotational transformation matrix may be used as follows:

$$\begin{bmatrix} T \\ R \end{bmatrix} = \begin{bmatrix} \cos(\Omega t) & \sin(\Omega t) \\ -\sin(\Omega t) & \cos(\Omega t) \end{bmatrix} \begin{bmatrix} X \\ Y \end{bmatrix}. \quad (11)$$

Similarly, the  $(\mathbf{R}, \mathbf{T})$  coordinates may be transformed to the vial-local coordinate system, which rotates at the same frequency,  $\omega$ . The observer this time would be inside the vial looking downward and spinning with the vial. Spheres would remain at rest until spontaneously moving freely across the vial to come at rest once again. The transformation has the opposite sign since the rotation direction is reversed:

$$\begin{bmatrix} x \\ y \end{bmatrix} = \begin{bmatrix} \cos(\omega t) & -\sin(\omega t) \\ \sin(\omega t) & \cos(\omega t) \end{bmatrix} \begin{bmatrix} T \\ R \end{bmatrix}. \quad (12)$$

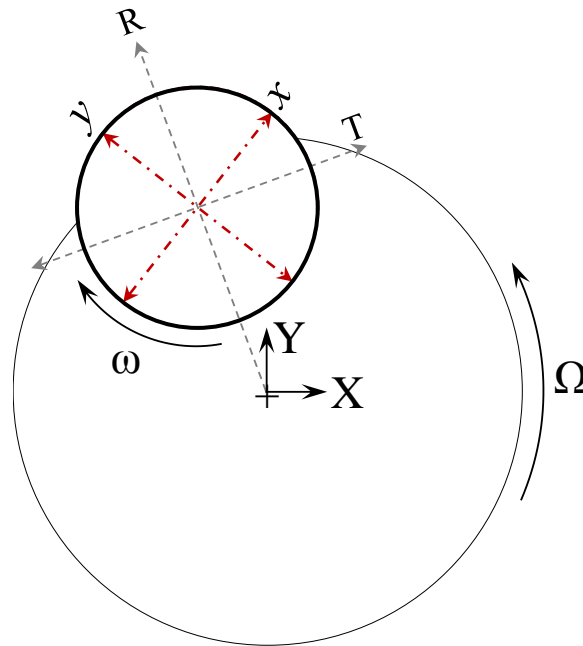


Figure 3. The radial-transverse coordinate axes  $(\mathbf{R}, \mathbf{T})$  and the vial-local coordinate axes  $(\mathbf{x}, \mathbf{y})$  are shown in comparison to the global  $(\mathbf{X}, \mathbf{Y})$  coordinates.

Lu et al. used the cumulative time  $t_2$  as the total cycle time. Depending on the shape of the path followed by the spheres inside the vial, this assumption can either be an

over or under estimate. A different method for calculating the cycle time of a single milling sphere is presented in this work. The total cycle time is best illustrated in the  $(\mathbf{R}, \mathbf{T})$  coordinate system. A single cycle is broken into two parts: ‘free motion’ and ‘return motion’. The free motion time  $t_f$  is simply:

$$t_f = t_2 - t_1 \quad (13)$$

The return motion time is the time required for the milling ball to return from the point of impact to the point of take-off. The two cycle parts are shown graphically in Figure 4.

The return time  $t_r$  period is expressed as follows:

$$t_r = (\theta_1 + \theta_2)/\omega. \quad (14)$$

The angles  $\theta_1$  and  $\theta_2$  may be found by transforming the global Cartesian coordinates of the milling sphere at times  $t = t_1$  and  $t = t_2$  using Equation (11) above and with the following expressions:

$$\theta_1 = \tan^{-1} \frac{R_1}{T_1}, \quad (15)$$

$$\theta_2 = \tan^{-1} \frac{R_2}{T_2}. \quad (16)$$

Care must be taken into account for the equivalent angle solutions to the inverse tangent function depending on the quadrant of the measured angle.

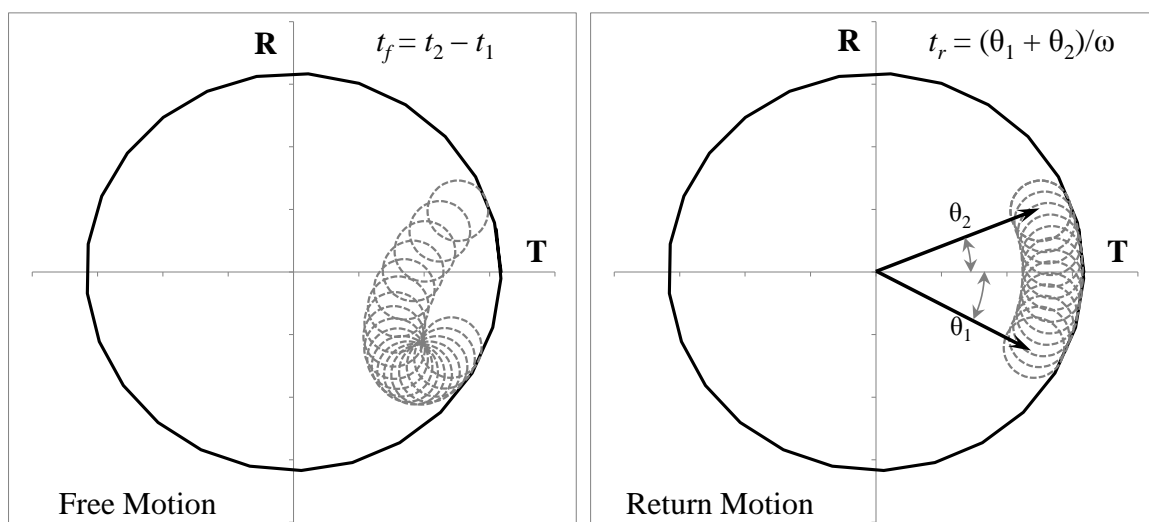


Figure 4. The free motion time period (left) and the return motion time period (right), with the sphere travel path shown as dashed circles.

The actual path of multiple milling spheres certainly differs from the theoretical path of a single sphere for several reasons. First, the impact is assumed to be perfectly plastic. The spheres rebound within the jar after impact. Second, collisions between the milling spheres occur frequently which further complicates the success of predictive models. Finally, viscous effects of motion through a pressurized gas or fluid contained within the vial are not considered. Thus, the model shown above serves as a qualitative estimation of the true impact conditions within the vial.

#### PLANETARY BALL-MILL DESIGN OPTIMIZATION

The goal of the design optimization is to maximize the lateral dimension of the nanographite platelets while minimizing their thickness. For exfoliation of layered structures such as flake graphite into nanographite platelets, oblique impact with high shear is preferable. The shape of the path taken by the milling spheres has a profound effect on the energy and characteristic of the grinding action of the mill. The design parameter of the ball mill with the strongest effect on the impact is the relative rotation

rate of the milling vial with respect to the sun disc. An illustrative comparison of the effect of the rotational speed ratio  $\omega: \Omega$  on the path of a single milling sphere is shown in Figure 5. For higher speed ratios, the milling sphere path results in an impact with a strong normal component and minimal shear with the vial wall. For relatively low frequency ratios, the path of the milling ball tends to intersect with itself causing a higher frequency of oblique ball-to-ball impacts. During the milling process, the spheres become coated with the ground substance forming layers.<sup>10</sup> It was assumed that the graphite flakes would tend to coat the spheres with the layers aligned tangentially. Thus, for exfoliation processes, oblique impact is preferable to normal impact for preserving the lateral dimension of the platelets.

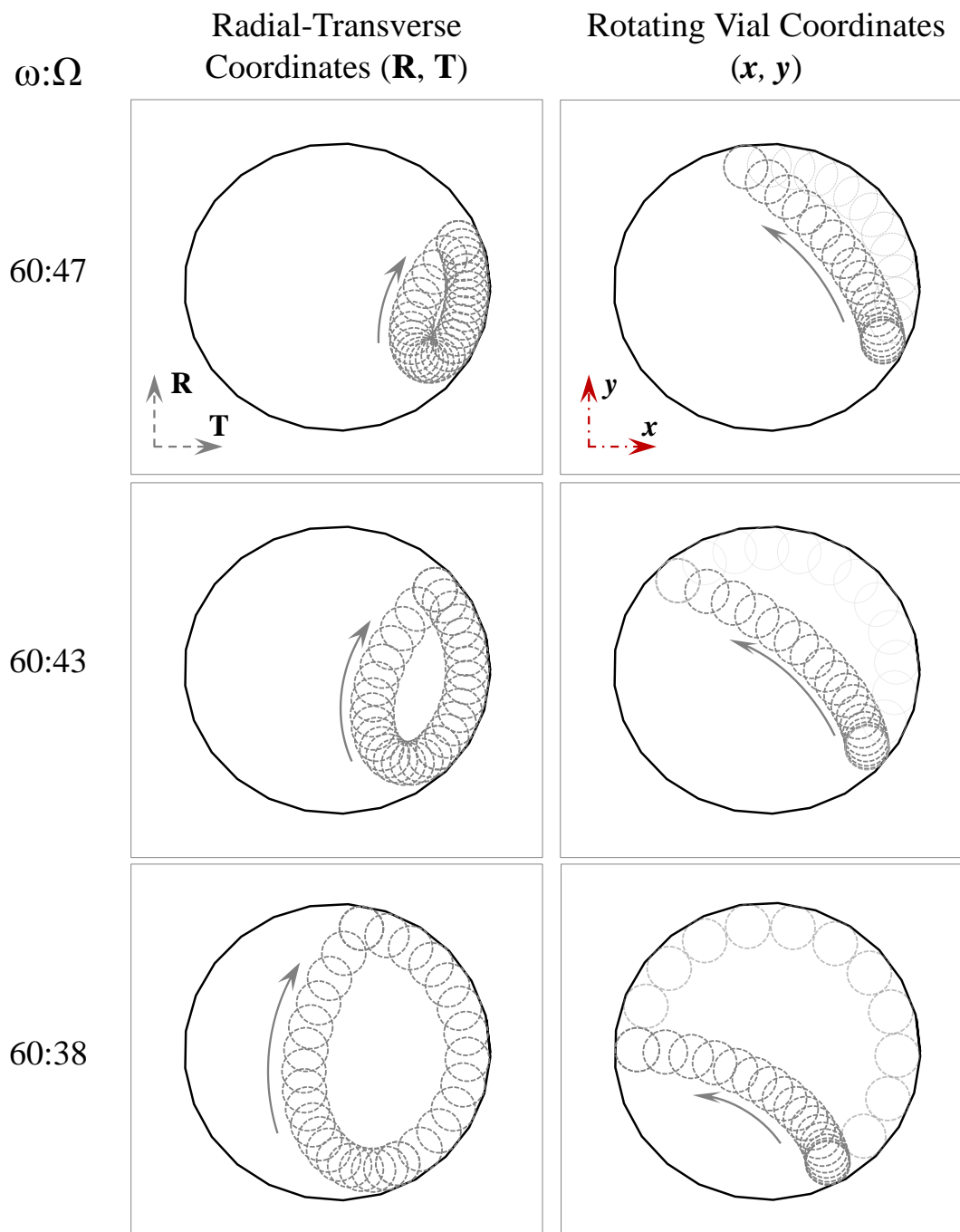


Figure 5. A comparison of the path of a single milling sphere for different rotation speed ratios. The left column shows the continuous loop motion that would be observed for the ( $\mathbf{R}, \mathbf{T}$ ) coordinate system viewer. The right column shows the dynamic path of a single milling sphere in dark grey dashed circles as viewed in the local ( $\mathbf{x}, \mathbf{y}$ ) coordinate system. The light dashed circles are shown for reference to represent the portion of the vial wall occupied by fixed, apparently-motionless, spheres at a given instant in time.

## GRINDING ENERGY MODEL

The energy supplied to the ground substance is a result of the kinetic energy transfer between the milling ball and either another ball or the vial wall. For simplicity, only the impact of a grinding ball and the vial are considered. The first step is to calculate the relative velocity of the ball and its point of contact with the vial. An illustration of the relevant vectors, coordinates, and angles is shown in Figure 6. The vector between the vial center and the coordinates of the sphere at the instant of its impact with the vial wall forms an angle  $\beta$  from global  $\mathbf{X}$  direction. The instant at  $t_2$  is used from previous calculations for simplicity as follows:

$$\beta = \tan^{-1} \left( \frac{Y_2 - Y_{c2}}{X_2 - X_{c2}} \right). \quad (17)$$

Again, careful attention to the quadrant of the inverse tangent function is necessary. The coordinates of the impact of the sphere against the vial wall ( $X_2^*$ ,  $Y_2^*$ ) are calculated as follows:

$$X_2^* = X_{c2} + r_v \cos \beta, \quad (18)$$

$$Y_2^* = Y_{c2} + r_v \sin \beta. \quad (19)$$

The vector  $r_2^*$  between the sun disc center and the point of impact forms an angle  $\gamma$  with the global  $\mathbf{X}$  direction and is calculated as follows:

$$\gamma = \tan^{-1} \frac{Y_2^*}{X_2^*}. \quad (20)$$

$$|r_2^*| = \sqrt{(X_2^*)^2 + (Y_2^*)^2} \quad (21)$$

The components of the velocity vector of the vial wall at the point of impact are expressed:

$$v_{x2}^* = -r_2^* \Omega \sin \gamma + r_v \omega \sin \beta, \quad (22)$$

$$v_{y2}^* = r_2^* \Omega \cos \gamma - r_v \omega \cos \beta. \quad (23)$$

Finally, the magnitude of the resultant velocity of the impact  $v_r$  is calculated using the velocity of the milling sphere during its free motion:

$$v_r = \sqrt{(v_x - v_{x2}^*)^2 + (v_y - v_{y2}^*)^2}. \quad (24)$$

The resultant velocity of the impact is not instantaneous and is composed of tangential and normal components. The angle  $\delta$  between the resultant velocity vector and the  $\mathbf{X}$  axis is defined as:

$$\delta = \tan^{-1} \left( \frac{v_y - v_{y2}^*}{v_x - v_{x2}^*} \right). \quad (25)$$

The components of velocity  $v_n$  and  $v_t$  in the normal and tangential directions respectively are expressed as follows:

$$v_n = v_r \cos(\delta - \beta) \quad (26)$$

$$v_t = v_r \sin(\delta - \beta) \quad (27)$$

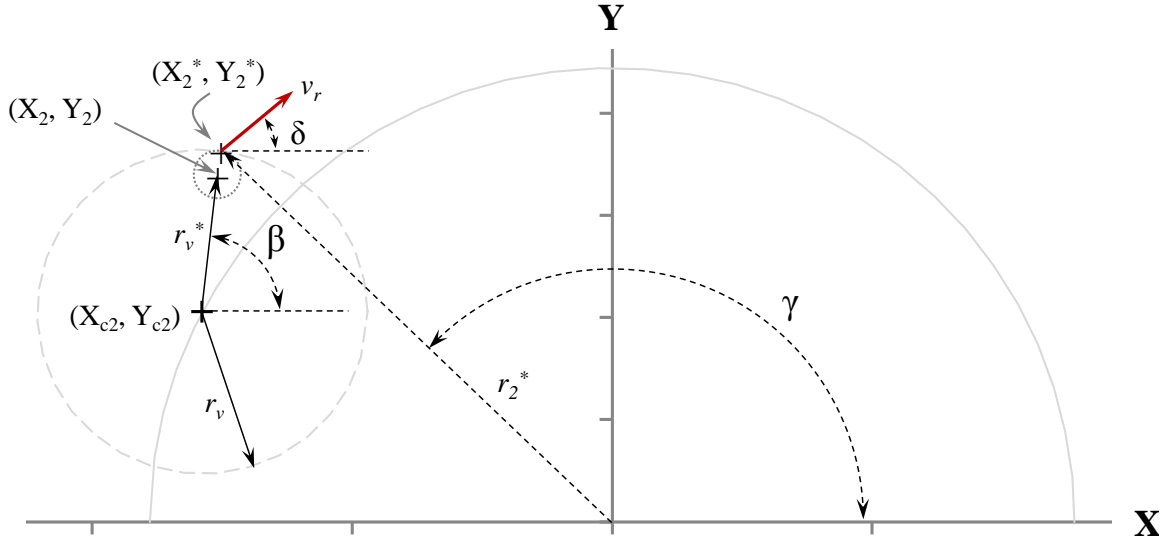


Figure 6. The relevant vectors, coordinates, and angles required to determine the relative velocity of impact between a milling sphere and the vial wall.

To calculate the energy  $U$  of the impact conditions in terms of normal and shear components, the impact is assumed to be perfectly plastic, such that the relative velocity of the sphere to the wall goes to zero. This assumption is for simplicity only, since the coefficient of restitution of the impact is certainly nonzero. However, it gives a point of comparison between different configurations. The maximum available kinetic energy available for the impact is defined as follows:

$$U_n = \frac{1}{2} m_s v_n^2, \quad (28)$$

$$U_s = \frac{1}{2} m_s v_t^2. \quad (29)$$

The mass of the sphere is  $m_s$ . To calculate the power of the impact components  $W$ , the impact time duration  $\tau$  must be known. The following expressions are based on Hertzian contact theory as adapted for planetary ball-mill systems by Maurice<sup>10</sup> and Lu:<sup>11</sup>

$$\tau = g_\tau v_n^{-0.2} \left( \frac{\rho_s}{E_{eff}} \right)^{0.4} r_b, \quad (30)$$

The time of normal impact is related to the density of the sphere  $\rho_s$  and the effective modulus of the sphere and the other colliding body  $E_{eff}$ . When the two impacting materials have the same modulus, Young's elastic modulus may be used. When the modulus differs, the average value is used. A geometric scaling factor  $g_r$  is used to account for the relative curvature of the impacting bodies. The average power of the impact is as follows:

$$W_n = U_n/\tau, \quad (31)$$

$$W_s = U_s/\tau. \quad (32)$$

The Hertzian contact radius is defined as follows:

$$r_n = g_r v_n^{0.4} \left( \frac{\rho_s}{E_{eff}} \right)^{0.2} r_b. \quad (33)$$

Another geometric scaling factor is introduced,  $g_r$ . A summary of geometric scaling factors is shown in Table 1. The total deflection  $\epsilon_{max}$  of the contact surface of the sphere is defined:

$$\epsilon_{max} = r_n^2/2r_b. \quad (34)$$

The pressure between the impacting bodies is expressed with a third scaling factor,  $g_p$ .

$$P_n = g_p v_n^{0.4} \left( \frac{\rho_s}{E_{eff}} \right)^{0.2} E_{eff}, \quad (35)$$

Table 1. Geometrical scaling factors from Hertzian contact adapted from Maurice and Courtney<sup>10</sup>.

Collision Type	$g_t$	$g_r$	$g_p$
Sphere-Sphere $r = r, E = E$	5.5744	0.9731	0.4646
Sphere-Plane	6.4034	1.4750	0.3521
Sphere-Cylinder*	$6.4034(k-1/k)^{0.2}$	$1.4750(k/k-1)^{0.4}$	$0.3521(k-1/k)$

\*For the case of a sphere within a cylinder such as a ball-mill,  $k = -r_v / r_s$ .

Note: From “The Physics of Mechanical Alloying: A First Report” by D. R. Maurice and T. H. Courtney, 1990, *Metallurgical Transactions*, 21A, p. 292. Copyright 1990 by Springer Science. Adapted with permission.

To calculate the temperature rise of the local impact, the volume of material trapped between the impacting media must be approximated. A first order estimation assumes that the milled powder coats the spheres and the cylindrical vial wall evenly throughout in a thin layer with thickness  $h_p$  as follows:

$$h_p = \left( \frac{m_p / \rho_p}{4\pi N_s r_s^2 + \pi r_v (h_v)} \right). \quad (36)$$

The mass and density of the milled powder are  $m_p$  and  $\rho_p$ , respectively. The thickness of the layer is assumed to be such that curvature is negligible. The number of spheres is  $N_s$ . The internal height of the vial  $h_v$  is the total height of the vial, since the internal corners generally have a radius to allow for full contact with the milling spheres. The volume of material between the spheres is approximated as a cylinder with radius  $r_n$  and height  $2h_p$ .

Without detailed supporting research specific to the material being milled, the fraction of total impact energy converted to heat is unknown. Maurice and Courtney used an expression for the flow stress of ductile metals and the peak rate of strain to calculate the heat release.<sup>10</sup> In a calorimetric study, Kwon and colleagues determined that the heat production was on the order of 80 % of the total input energy. For mill containing only milling spheres, the equilibrium internal vial temperature was 600 °C. Increasing the pressure of gas within the vial tended to limit the steady-state temperature.<sup>13</sup> A scaling factor  $C_1$  has been introduced for this work to account for the

fraction of instantaneous kinetic energy transfer that is converted to heat. The value of  $C_1$  must be determined experimentally. The local temperature rise  $\Delta T$  of the entrapped powder with heat capacity  $C_p$  is thus calculated:

$$\Delta T = C_1(U_n + U_s)/C_p\rho_p\pi r_n^2 2h_p \quad (37)$$

It is apparent from Equation (37) that the quantity of powder in the vial has a direct effect on the temperature rise expected, and consequently, the potential for reactivity within the vial.

### OXIDATION KINETICS

The oxidation reaction of graphite into NGOP was assumed to be a form of the Boudouard reaction between graphite and *carbon dioxide* with an intermediate level of anisotropy following the model by Calo and Perkins.<sup>15</sup> For high pressures of *carbon dioxide*, the formation of a stable oxide was expected to be favorable over the reverse reaction of reduction by *carbon monoxide*. The impact of the ball-mill creates new active sites that are empty of adsorbed molecules. The temperature of the impact allows for the surface oxide complex to be formed. This topic was not directly studied in this work. Instead, verification of the success of the oxidation reaction was done using nuclear magnetic resonance (NMR) analysis.

### FUNCTIONALIZATION STRATEGY OF NANOGRAPHITE OXIDE PLATELETS

The ball-mill process under an atmosphere of carbon dioxide is intended to introduce *hydroxyl* and *carboxyl* defects along the perimeter of the platelet.<sup>8</sup> The defects become active sites for covalently bonding functional molecules. For the purposes of producing an initiator species for anionic polyamide, *toluene 2,4-diisocyanate* TDI has

been shown to react with such defects on the surfaces of carbon nanotubes by Yan<sup>16</sup> and by Yang independently.<sup>17</sup> A schematic of the proposed reaction is shown in Figure 7.

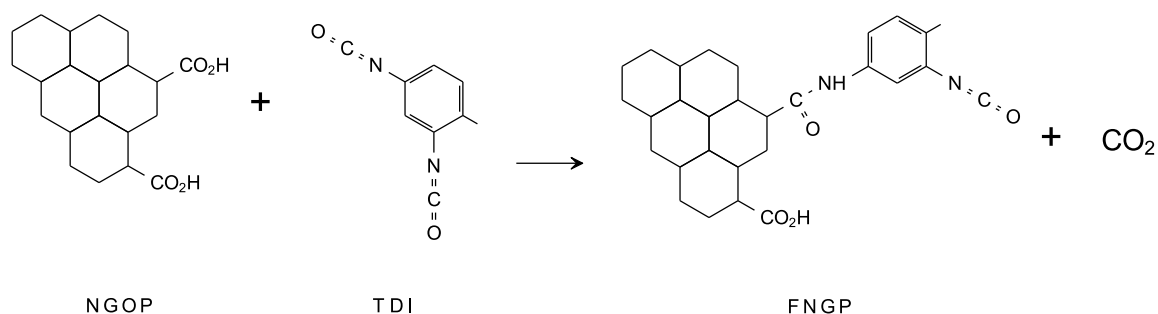


Figure 7. The prototypical reaction of a diisocyanate with the NGOP carboxyl functional groups is shown.

Introducing the nanoparticles into an excess of diisocyanate allows one NCO group to react with the surface defects while leaving the other functional group unreacted. The particles are then introduced into a solution of  $\epsilon$ -caprolactam which “blocks” the isocyanate, rendering it chemically stable. Simultaneously, the blocked isocyanate group becomes an effective initiator for APA-6. An illustration of the initiation and propagation reaction of APA-6 using the TDI functionality as an initiator is shown in Figure 8.

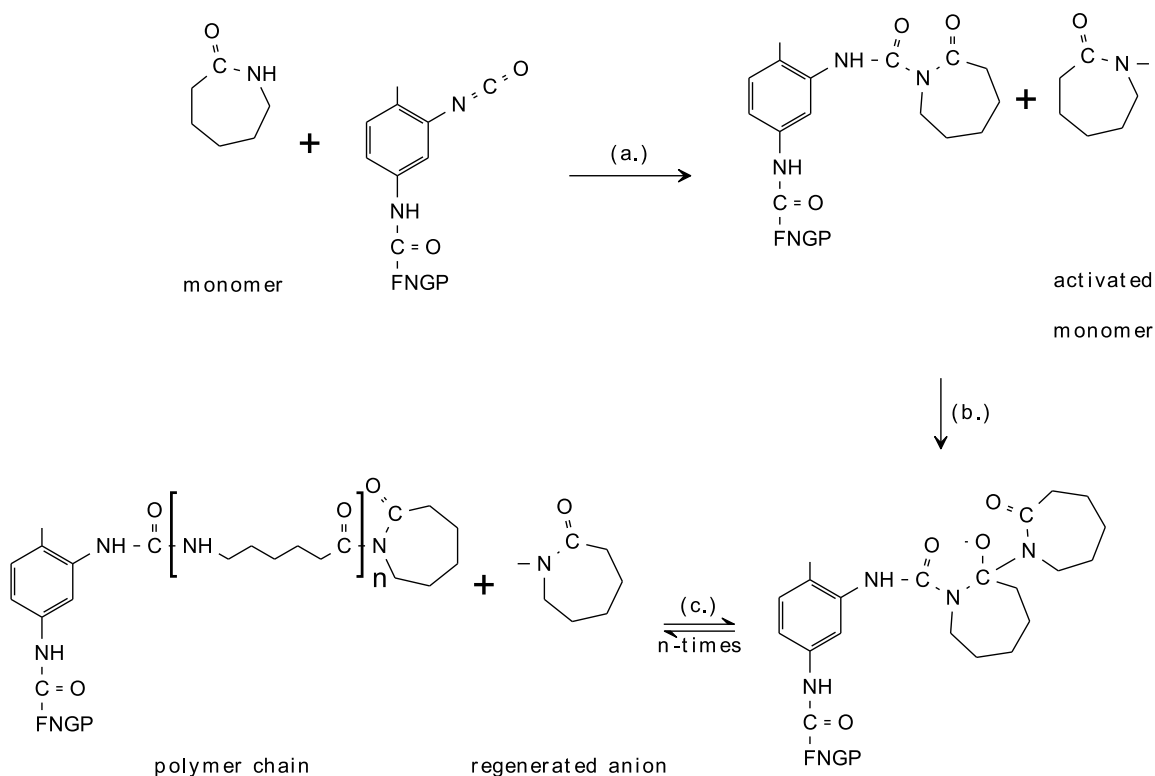


Figure 8. Activated monomer and FNGPs are placed into a solution of molten  $\epsilon$ -caprolactam. (a.) The isocyanate functional group reacts with a  $\epsilon$ -caprolactam molecule producing the initiator species required for APA-6 polymerization. (b.) An activated  $\epsilon$ -caprolactam anion reacts with the initiator at the C=O group of the lactam ring. (c.) The lactam ring opens while simultaneously regenerating the anion from another monomer molecule. Step (c.) repeats n-times until the monomer is consumed or the chain is terminated.

## MATERIALS

Natural flake graphite (85-98 % carbon) CAS#7782-42-5 was supplied by Asbury Carbons. Standard grade dry ice was used to produce the *carbon dioxide* atmosphere within the milling vial. The diisocyanate for functionalization was *4,4'-methylene diphenyl diisocyanate* 98% (MDI) from Acros Organics. The reaction solvent, *toluene* 99.5 % from Fisher Chemical, was dried over 3A molecular sieves prior to use. The anionic polymerization grade monomer  $\epsilon$ -caprolactam, commercially available activators, *caprolactam magnesium bromide* (Nyrim C1) and *sodium caprolactam* (Bruggolen C10), and an initiator, *hexamethylene-1,6-dicarba-moylcaprolactam*

(Bruggolen C20) were supplied from Brüggemann Chemical. Concentrated *nitric acid* (65 % w/w) and laboratory grade methanol were supplied by Fisher Chemical. Polar nanographite platelets (N008-100-P-10) were supplied by Angstrom Materials, Inc. Distilled water was produced using a standard laboratory distiller.

## METHODS

### PLANETARY BALL-MILL DESIGN

A planetary ball-mill (UAB Ball-Mill) was constructed for this study. The baseline  $\omega: \Omega$  ratio of 60: 47 was used. The vial radius  $r_v$  of 31.8 mm combined with a sphere radius of 4.76 mm produced a virtual vial radius  $r_v^*$  of 27.0 mm. The sun disc radius  $r_d$  to the center of the vial was 88.9 mm. The vial was capable of pressurization up to 1.72 MPa using a spring actuated pressure relief valve. A section view of the computer-aided design model and a photograph of the final build are shown in Figure 9. The results of the kinetic analysis of the design are summarized in Table 2. Also included in the table are comparative results obtained by analyzing the operation conditions of the Fritsch Pulverisette 6 used by Jeon et al. to produce nanographite oxide platelets.<sup>8</sup> The kinetic energy available during impact from the UAB Ball-Mill is at least an order of magnitude higher than the calculated energy of the Pulverisette 6, which was shown to be adequate for NGOP production. Consequently, the milling time of the UAB Ball-Mill was approximately an order of magnitude shorter. The normal and shear components of impact for the UAB Ball-Mill are approximately equal. The Pulverisette 6 showed a dominantly normal component of impact.

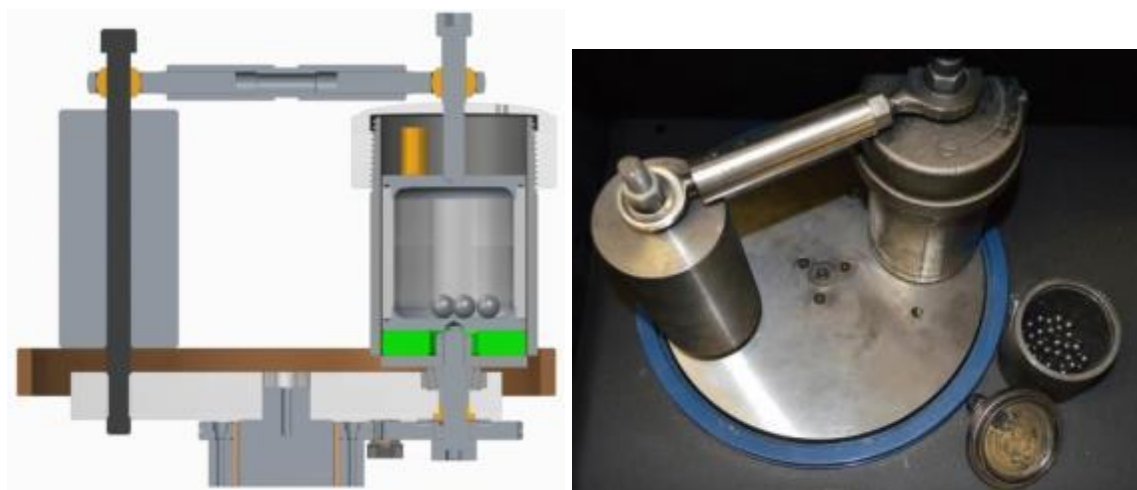


Figure 9. (left) A section view of the planetary ball mill design. The milling vial is shown inside its casing. A steel counterbalance mass is shown opposite. The two masses are connected at the top with a turnbuckle linkage to prevent significant radial deflection. (right) A photograph of the actual build is shown with the open milling jar on the right.

Table 2. A summary of parameters for comparison between planetary mills used to make nanographite oxide

Mill	$\Omega$ (rpm)	$ \omega/\Omega $ (-)	$r_d$ (mm)	$r_v$ (mm)	$\tau$ ( $10^{-5}$ s)	$(t_f + t_r)^{-1}$ (Hz.)	$U_n$ (mJ)	$U_s$ (mJ)	$\Delta T$ (K)
UAB	600	1.28	89	32	2.9	36.5	29	32	440
Jeon <sup>8</sup>	500	1.82	61	30*	1.5	16.2	2.4	0.56	40**

\*Estimated from photographs

\*\*Based on reported operation procedure and an estimated 200 spheres

## BALL-MILLING

The procedure outlined by Jeon et al.<sup>8</sup> to produce nanographite oxide platelets (NGOPs) was used as a baseline procedure. The stainless steel milling jar was loaded with 2.0 g of bulk graphite flakes, 50 hardened stainless steel spheres (9 mm diameter), and approximately 20 g of dry ice. The internal pressure of the jar was maintained at 1720 kPa (250 psi) using a spring-actuated pressure relief valve. The contents were milled at a speed of  $\Omega=600$  rpm for 6 hours.

## FUNCTIONALIZATION

The as-milled NGOPs contained iron contamination from the milling process. To remove the iron, an acid pre-treatment was done. Ball-milled graphite from three

separate milling runs totaling 6.7 g was dispersed in 150 ml of *methanol* in a sonication bath for 5 minutes. Then, 50 ml of concentrated 65 % w/w *nitric acid* was added. The platelets were left for 18 hours in a fume hood. The strength of the *Nital* solution undoubtedly increased as the methanol was allowed to evaporate. The platelets were recovered by vacuum-filtering the solution with a 5.0  $\mu\text{m}$  polycarbonate membrane filter. The platelets were subsequently rinsed several times with a total of 1.5 L of distilled water. The NGOP powder was then dried in an oven in air at 300 °C for 30 minutes to remove any traces of the nitric acid. A total of 2.38 g of NGOP was recovered.

This functionalization reaction was adapted from works done by Yan<sup>16</sup> and Yang<sup>17</sup> for functionalizing carbon nanotubes with TDI for APA-6 initiation. Although several other isocyanate forms were shown to be reactive with graphene oxide by Stankovich<sup>18</sup> thus supporting the interchangeable nature of isocyanates. The isocyanate used for this study MDI has been shown to be compatible with graphene oxide for *in-situ* polyurethane polymerization by Li et al.<sup>19</sup> However, the relative reactivity of isocyanates and carboxyl groups was expected to be lower than with the hydroxyl groups present on graphene oxide derived from chemical methods.<sup>20</sup> A catalyst, *magnesium perchlorate*  $\text{Mg}(\text{ClO}_4)_2$  was identified from literature to increase the isocyanate/carboxyl reaction.<sup>20</sup>

A 1 L, two-neck round-bottom flask equipped with a reflux condenser was solvent rinsed and flame dried under vacuum 3 times. The flask was then back-filled with dry nitrogen. A 2.0 g portion of the NGPO recovered from the acidification step was placed into the flask and flame dried under vacuum and back-filled with dry nitrogen a final time. Next, the entire flask was moved to an oxygen-free nitrogen glove box, and 5.0 g of MDI and 500 ml of anhydrous *toluene* were added. The reaction vessel was

moved to a heated oil bath at 80 °C and stirred vigorously for approximately 8 hours under dry nitrogen. To complete the reaction, an excess of 2:1 molar ratio of  $\epsilon$ -*caprolactam* to diisocyanate was added to block the NCO groups. The reaction was allowed to continue for an additional 30 hours to ensure all NCO groups were consumed for safe handling under normal laboratory procedures.

The solution was rotary evaporated until a concentrated 200 ml solution was obtained. The NGPs were isolated with a 5.0  $\mu\text{m}$  polycarbonate filter. The filtrate solution was recovered and diluted 5:1 with *methanol* to precipitate crystalline  $\epsilon$ -*caprolactam*-blocked MDI over several days. The NGPs were washed with 300 ml of *toluene* followed with 1.0 L of *methanol* to completely remove any excess caprolactam. The functionalized nanographite oxide platelets (FNGPs) were dried under vacuum at 120 °C for 3 days prior to use.

#### FNGP SURFACE POLYMERIZATION TESTS

The ability of the FNGPs to initiate surface APA-6 polymerization was tested in two ways. First a bulk sample of 1.5 wt. % Bruggolen® C10 activator, 10.0 wt. % FNGPs, and 5 g  $\epsilon$ -*caprolactam* was placed into a circulating air oven at 160 °C. The only initiator present in the bulk sample would be provided by the FNGPs. Second, thin film APA-6 samples were prepared for microscopy. A mixture of 1.5 wt. % Bruggolen® C10 activator, 1.0 wt. % FNGPs, and 5 g  $\epsilon$ -*caprolactam* was ground with a mortar and pestle within a glove box with a relative humidity < 10 %. Powder samples were placed between glass slides and heated with a hotplate set to 180 °C for 30 minutes. The samples were removed and observed under transmitted cross-polarized light with a Zeiss

Axioplan 2. The presence of surface polymerization would be observed as spherulite domains emanating from the FNGP surfaces.

A control sample of powder containing 1.0 wt. % FNGPs, 2.5 wt. % of the commercial initiator, Bruggolen® C20, and 5.0 wt. % Nyrin® C1 activator, was used to make a cast sample and for thin-film microscopy. The purpose of the control sample was to determine if the FNGPs themselves had a negative effect on the polymerization by introducing them into the commercial resin system. Inhibition of the polymer would be observed as leftover monomer after bulk polymerization or as regions of poor polymerization surrounding the FNGPs in the thin-film samples.

## CHARACTERIZATION

### PARTICLE SIZE AND MORPHOLOGY

Scanning electron microscopy (SEM) images were acquired with a Quanta FEG 650 SEM under high vacuum. Platelets were adhered to an aluminum stage using a thin adhesive film. The proximity of the platelets to the base negated the necessity for sputter-coating of the platelets to prevent charging. An accelerating voltage of 5–10 kV was used depending on the level of magnification. Secondary electron images were taken for determining platelet morphology. Back-scatter electron (BSE) images were used to determine the presence of metallic particle impurities.

### NUCLEAR MAGNETIC RESONANCE (NMR) <sup>1</sup>H SPECTROSCOPY

Dried samples of NGOP and FNGP were dissolved in deuterated *chloroform* under a stream of N<sub>2</sub>. <sup>1</sup>H NMR spectra were recorded on a Bruker DRX-400 NMR spectrometer. The test was carried out at room temperature, 300 K. The <sup>1</sup>H NMR spectra were referenced to internal SiMe<sub>4</sub> (TMS).

### THERMOGRAVIMETRIC ANALYSIS (TGA)

The success of the ball-mill process at converting graphite to nanographite oxide can be qualitatively determined through the thermal stability of the platelets. Graphene oxide undergoes thermal decarboxylation reactions at temperatures close to 300 °C.<sup>21</sup> A Du Pont Instruments Thermogravimetric Analyzer (TGA 2950) was used to determine the relative reactivity of the NGOPs and FNGPs compared to the neat GR flake source material. Powder samples were ramped to 600 °C at 20 °C min<sup>-1</sup> in nitrogen.

### FOURIER-TRANSFORM INFRARED SPECTROSCOPY (FTIR)

Functional group analysis was done using a Bruker ALPHA FTIR Spectrometer in attenuated total reflectance (ATR) mode. Powder samples of NGOP and FNGP were compared against the pure diisocyanate initiator *N,N'*-(Methylenedi-*p*-phenylene) bis[hexahydro-2-oxo-1*H*-azepine-1-carboxamide] CAS 54112-23-1 (SDI) produced simultaneously from excess MDI during the functionalization reaction.

### DIFFERENTIAL SCANNING CALORIMETRY (DSC)

Thermal properties of the polymer samples were measured using a TA Instruments DSC equipped with a TA Q100 Controller and refrigerated cooling system. The samples were heated from 40–320 °C at 10 °C min<sup>-1</sup>. The melting endotherm was integrated using TA Instruments Universal Analysis V4.5A software. The reference enthalpy of melting of APA-6 for crystallinity measurements was 230 J g<sup>-1</sup>, as per the ATHAS database.<sup>22</sup>

### X-RAY DIFFRACTOMETRY (XRD)

X-ray diffraction analysis was performed on a Siemens D500 PC Diffraction System. Powder samples were placed onto the goniometer and scanned from 2θ angle of

( $5^{\circ} - 35^{\circ}$ ) with a step of  $0.1^{\circ}$  and a dwell time of 10 s. The source was Cu  $k\alpha$  with a wavelength  $\lambda=1.54056$  nm.

## RESULTS AND DISCUSSION

### NGOP PARTICLE MORPHOLOGY

The as-received graphite flake is shown in Figure 10. The flake graphite was milled for 2 hours and observed again as shown in Figure 11. The milling process had not completely converted the flake graphite to NGOPs but platelets with sub-micron thickness were observed.

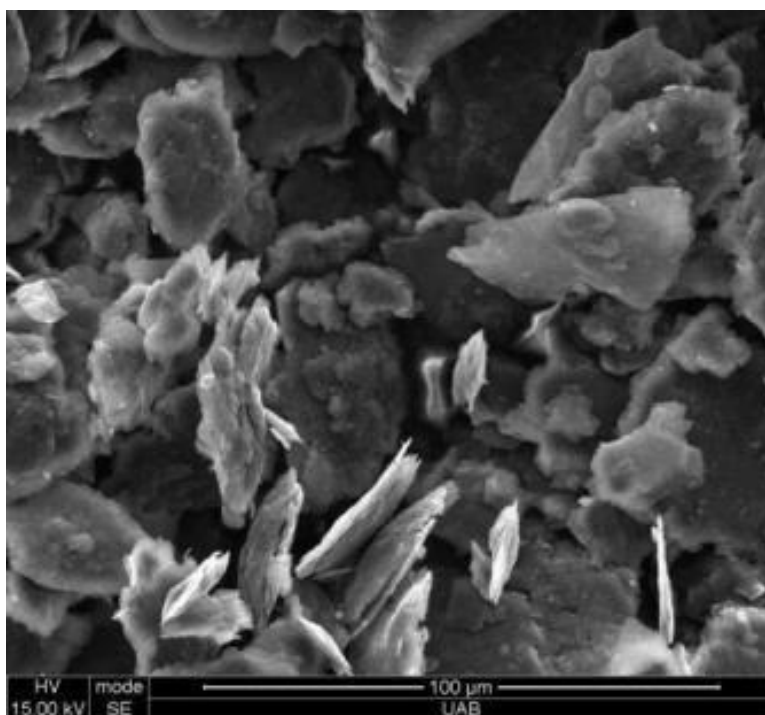


Figure 10. The as-received GR flake. Approximate platelet size was on the order of 10-100  $\mu\text{m}$  with thicknesses of several  $\mu\text{m}$ .

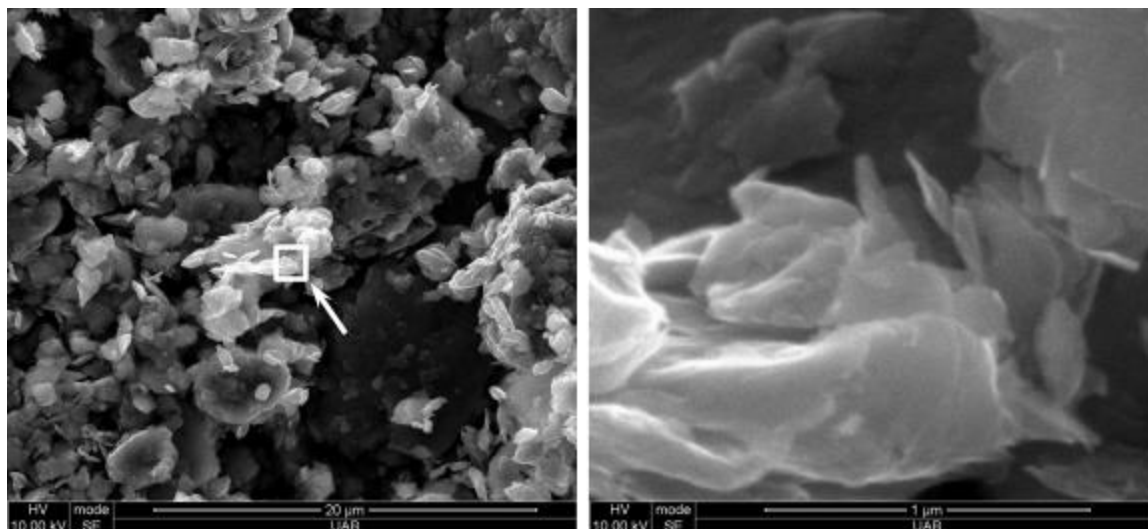


Figure 11. (left) NGOPs after 2 hours of milling. Variation in platelet size is shown with maximum lateral dimensions of approximately 5-10  $\mu\text{m}$ . (right) A detailed view from the marked area shows partially exfoliated platelets with lateral dimensions  $< 1 \mu\text{m}$  and thicknesses  $\ll 1 \mu\text{m}$ .

#### XRD ANALYSIS

The XRD pattern obtained for the NGOPs is shown in Figure 12. A single peak corresponding to the inter-gallery spacing of graphene layers in solid graphite (002) at 0.34 nm was observed. A broad peak near 23.8 was not observed which would have indicated a high degree of edge expansion from the carboxyl groups as observed by Jeon et al.<sup>8</sup> The produced NGOPs were, therefore, primarily graphitic in nature.

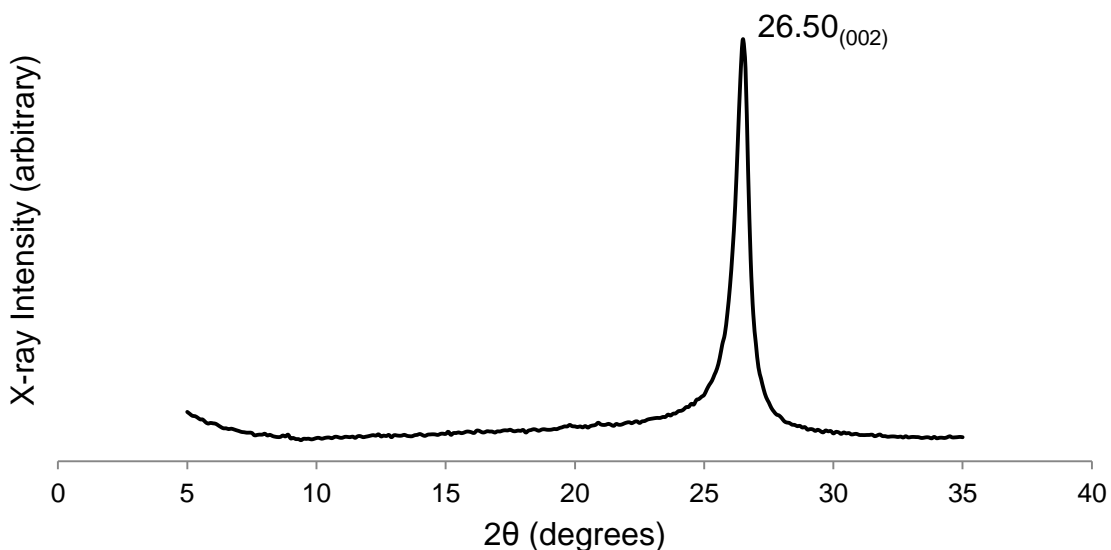


Figure 12. The X-ray diffraction pattern obtained from the NGOPs. The only peak observed was the 002 peak of graphite. No evidence of intercalation of the graphene layers was observed.

#### NGOP CHEMICAL PROPERTIES

The full  $^1\text{H}$  NMR spectrum of the NGOP analysis is shown in Figure 13. The dominant peaks correspond to carboxyl groups as expected. Other forms of graphene oxide such as those produced via Hummer's method<sup>5</sup> are expected to be nearly free of carboxylic acid groups as shown by He et al.<sup>2</sup> and Mermoux et al.<sup>1</sup> This is an advantage of the ball-milling process since carboxylic groups are sometimes a preferred functionality. For the FNGPs, a third peak appeared between the two original carboxyl peaks as shown in Figure 14. Although the spectra show differences between the NGOP and the FNGP, the cause of the difference is undetermined. The diisocyanate initiator molecules could either be covalently bonded to the carboxyl groups or the initiator could simply be adsorbed onto the surfaces.

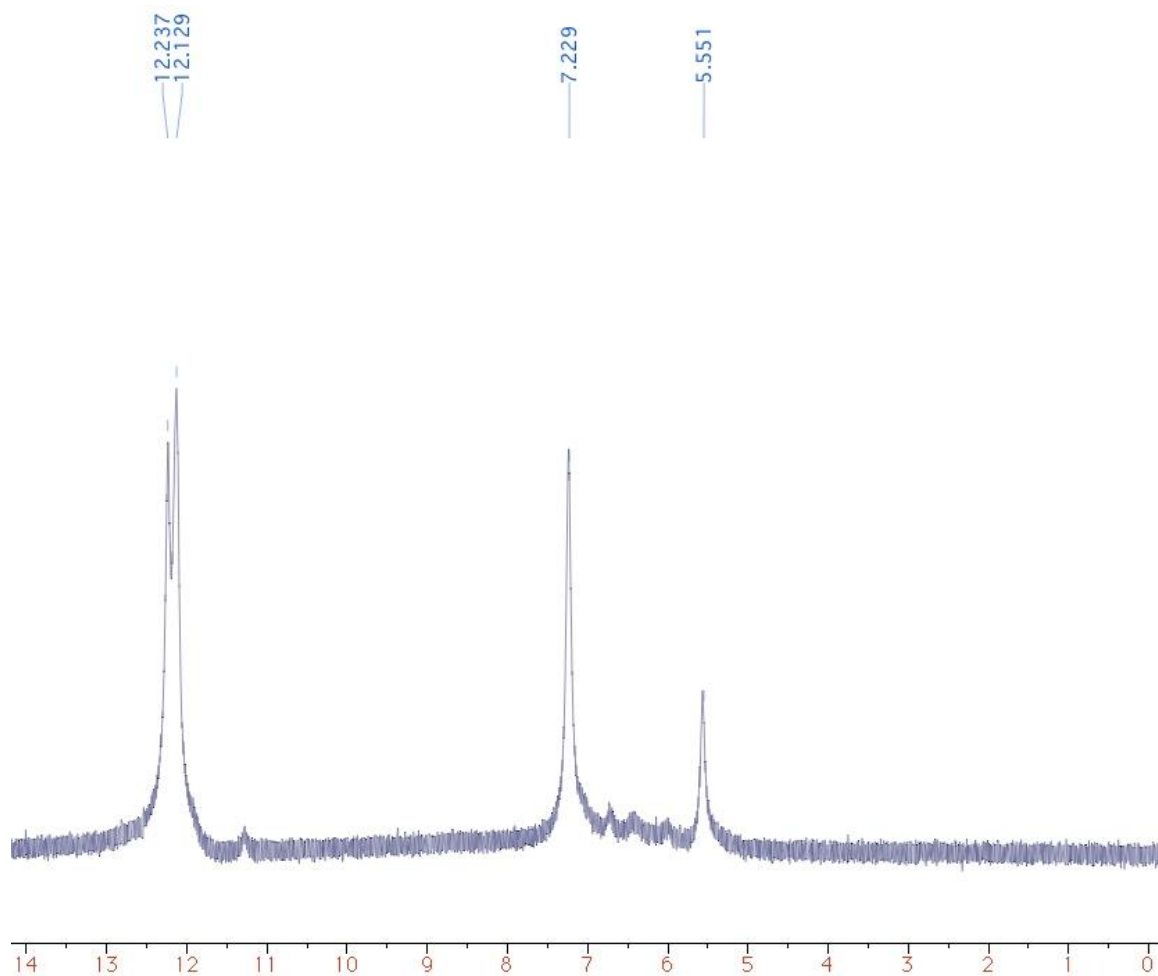


Figure 13. The full spectrum integration of NGOP. The dominant peaks at 12.129 and 12.237 ppm represent carboxylic protons. The peak at 7.229 ppm corresponds to the solvent *chloroform*. The third peak at 5.551 ppm was likely an amide group formed from a side reaction with nitrogen.

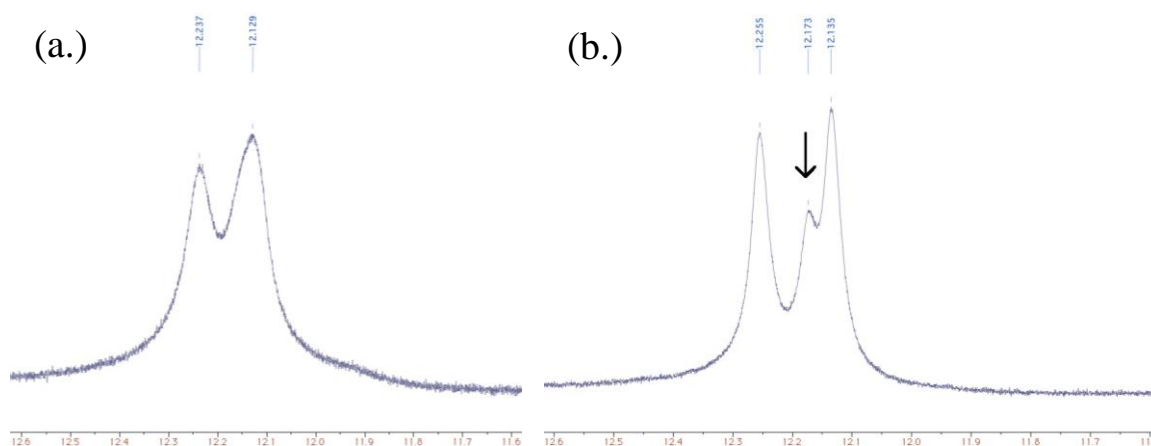


Figure 14. Detailed views of the <sup>1</sup>H NMR spectrum carboxyl peaks from (a.) NGOP and (b.) FNGP. The appearance of a third peak at 12.173 ppm could possibly indicate a covalent bond between the isocyanate and carboxyl groups for the FNGPs. Alternately, the diisocyanate initiator could be adsorbed to the FNGP surface and weakly interacting with the carboxyl groups without a covalent bond.

Thermogravimetric analysis was done in nitrogen to compare the thermal stability of the NGOPs and FNGPs to the source GR flake material. TGA analysis of the pure *diisocyanate* initiator is shown in Figure 15 for reference. An overlay of the TGA plots is shown in Figure 16. The two separate degradation temperatures of the FNGP correspond to those of the SDI.

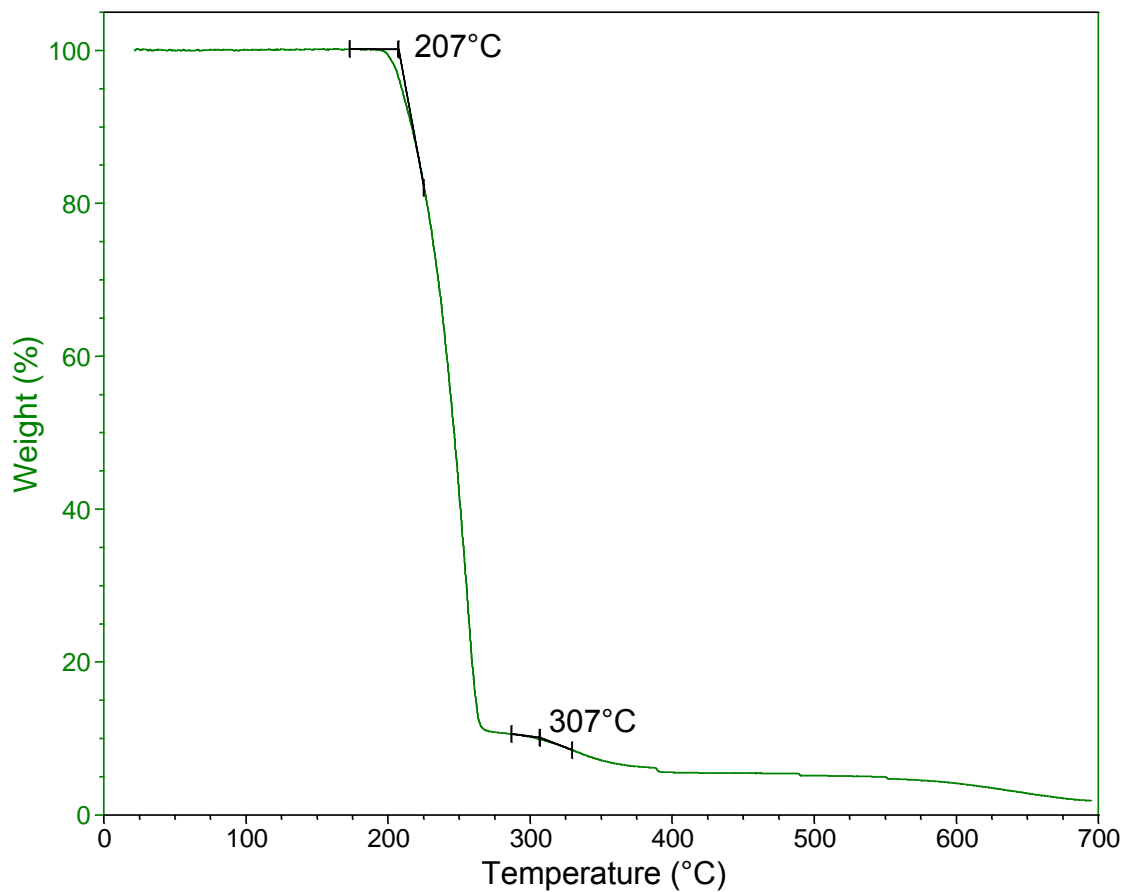


Figure 15. Thermogravimetric analysis of the pure diisocyanate initiator. Two distinct degradation temperatures at 216 °C and 306 °C are shown. The first transition corresponds to the de-blocking in which the  $\epsilon$ -caprolactam is released from the NCO groups.

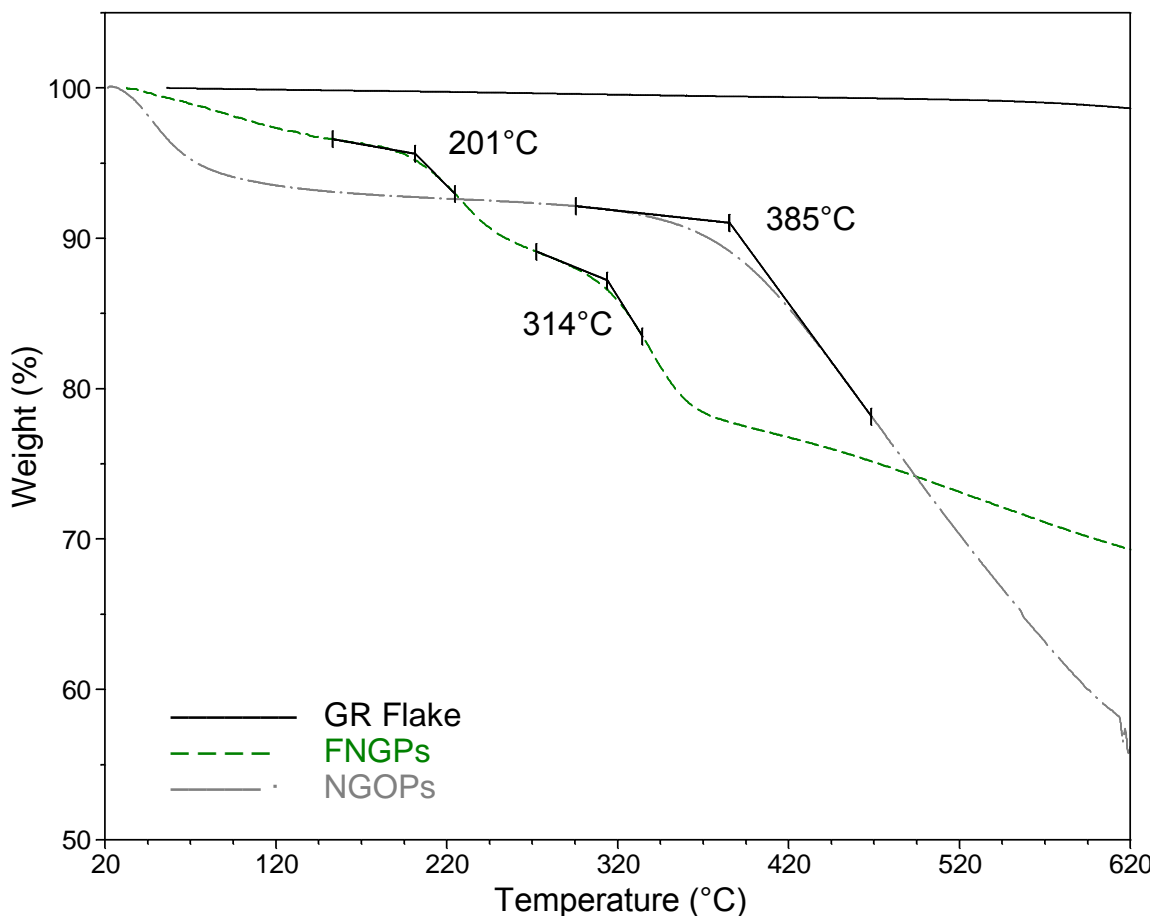


Figure 16. The thermal degradation of NGPOs (grey dash-dot) and FNGPs (green dash) are shown in comparison to the source bulk graphite flake (black solid). Two separate degradation temperatures are observed at 201 °C and 314 °C for the FNGPs, which correlate with the degradations of the pure SDI. The main degradation temperature of 385 °C of the NGOPs was not observed explicitly for the functionalized platelets.

The FTIR spectra of FNGPs and SDI are overlaid in Figure 17. The curves are shown after baseline correction and with a 5-point moving average and are shifted vertically for clarity. The ‘fingerprint’ region for wave numbers  $< 2000 \text{ cm}^{-1}$  appeared to match the SDI. The signal attenuation of the graphite was high thereby limiting the sensitivity of the FTIR in the ATR mode.

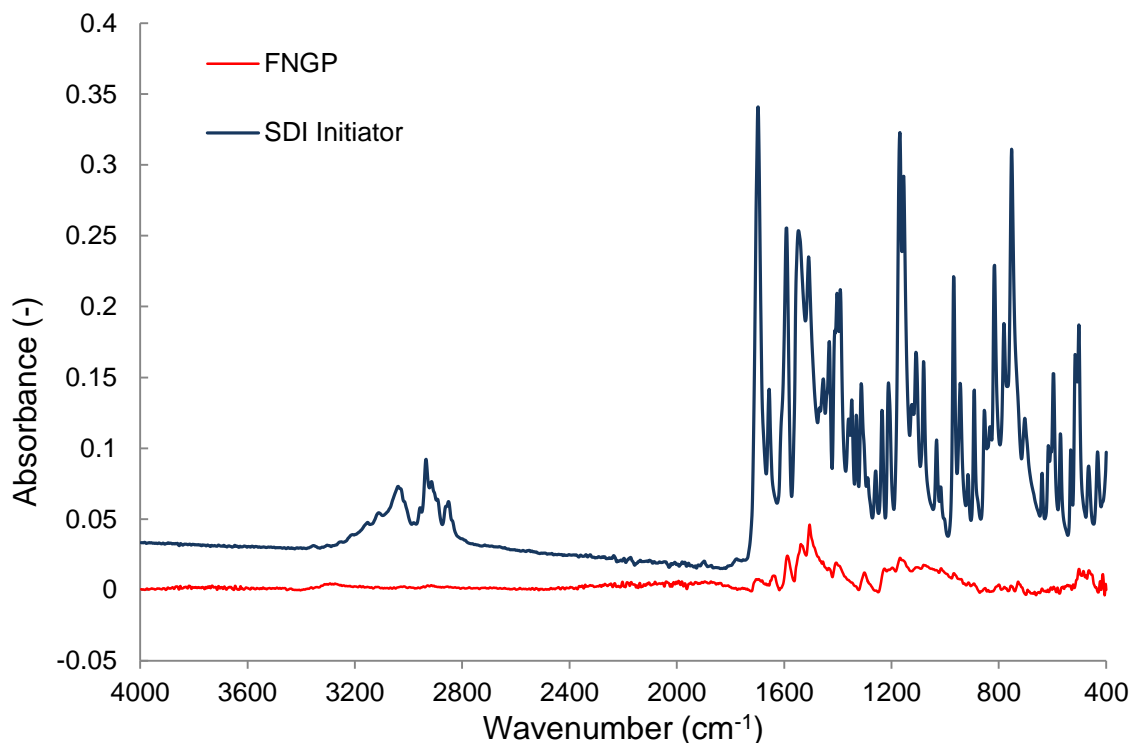


Figure 17. The FTIR spectra in total reflectance mode of pure diisocyanate initiator (black) and FNGPs (grey), as 5 point moving averages. Shifted vertically for clarity.

### SURFACE POLYMERIZATION TESTS

Surface polymerization was attempted with bulk polymerization samples and with thin film samples. After 60 minutes in the circulating air oven, the bulk powder sample showed no visible sign of polymerization. The control powder sample polymerized fully, but the FNGPs settled to the bottom of the vial. A plot of the heat flow from a DSC measurement of the cast control FNGP sample is shown in Figure 18. The lack of a monomer melting endotherm confirmed that the FNGPs did not inhibit the polymerization reaction. Crystallinity was calculated to be approximately 30.9 % which follows typical crystallinity percentages obtained in previous work.<sup>23</sup>

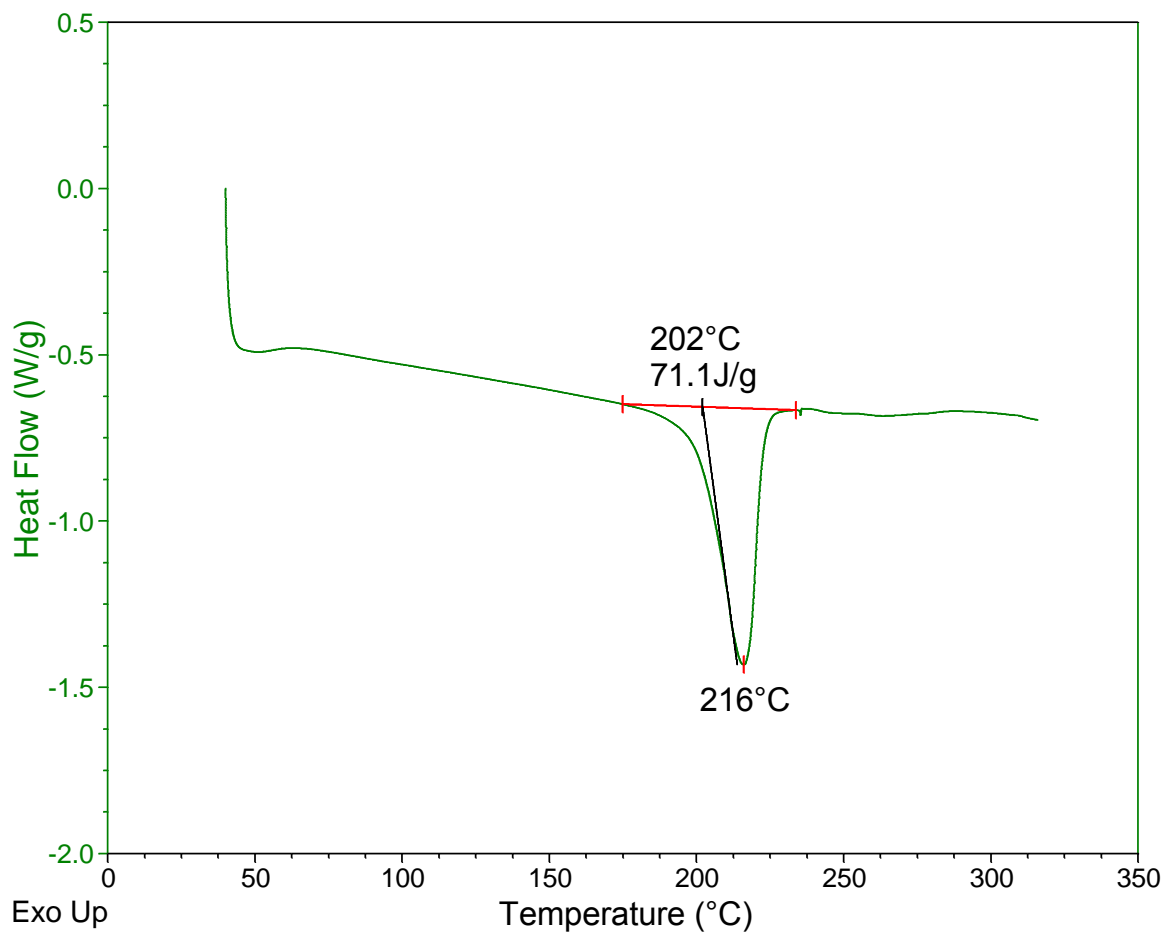


Figure 18. The melting endotherm of the control FNGP/APA-6 cast sample. A monomer melt endotherm was not observed, indicating uninhibited polymerization.

A comparison of thin-film cross-polarized micrographs is shown in Figure 19.

The FNGPs showed no evidence of surface-initiated polymerization. The micrograph in Figure 19 (a.) shows the FNGPs evenly distributed in the monomer even after the solution solidified. The control sample shown in Figure 19 (b.) contained added initiator and clearly shows a granular spherulite structure. Contrary to the non-polymerized sample, the FNGPs were agglomerated. The evidence suggests that the polymerization reaction tended to concentrate the FNGPs rather than separate them.

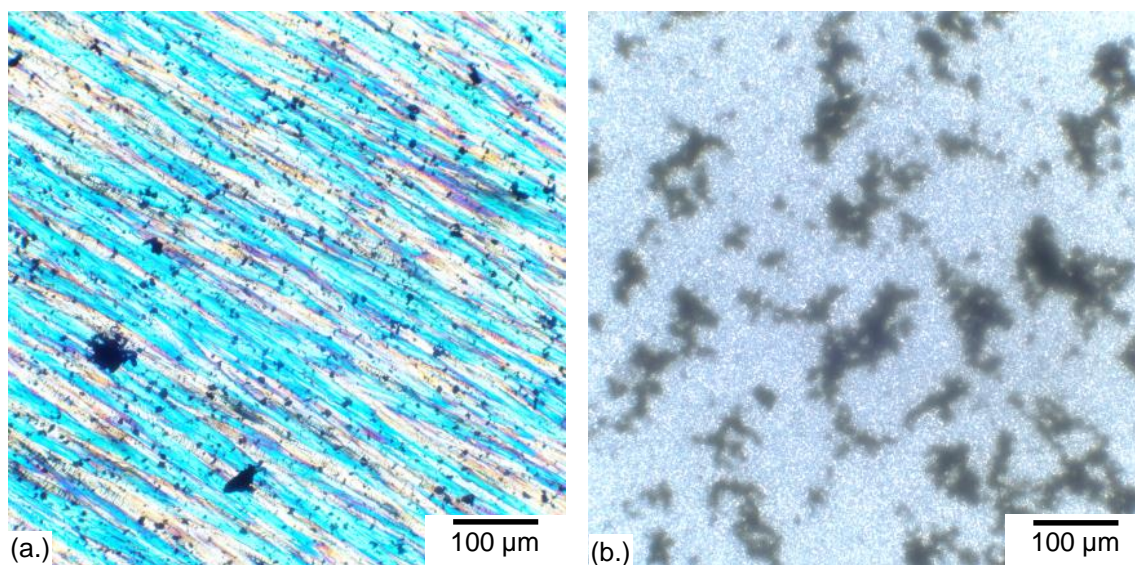


Figure 19. (a.) A micrograph of FNGPs dispersed uniformly in activated monomer, after 30 minutes of heating with no evidence of polymerization. The colors are caused by the crystalline structure of  $\epsilon$ -caprolactam after cooling. Dark spots are the FNGPs shown with some clumps. (b.) The control sample of FNGPs dispersed in co-activated monomer solution shows a granular spherulite structure with agglomerated FNGPs. No evidence of inhibited polymerization could be observed.

## CONCLUSIONS

NGOPs with sub-micron thickness were produced from GR flake as verified with SEM images. The ball-mill designed using the kinetic model was verified to produce carboxylated NGOPs as verified directly by  $^1\text{H}$  NMR analysis. The reactivity of the NGOPs was significantly increased over GR flake as observed with TGA analysis.

The non-catalyzed carboxyl/isocyanate functionalization route was tested. Two separate degradation temperatures of the FNGPs were observed which matched the SDI thermal behavior. The amidation reaction between the isocyanate and carboxyl groups, however, was not conclusively verified. FTIR analysis showed a match in the ‘fingerprint region’ between the FNGPs and the SDI. The  $^1\text{H}$  NMR spectrum of the FNGPs showed a separate peak between the two carboxyl group peaks at 12.173 ppm.

However, the SDI initiator was possibly adsorbed to the platelets rather than covalently bonded.

Although the SDI initiator was detected on the FNGPs, surface-initiated APA-6 polymerization was not observed. However, the FNGPs did not adversely affect the APA-6 polymerization reaction. The initiation functional groups may have been sterically inaccessible to the anion to initiate ring-opening polymerization. Successful amidation reaction between the isocyanate and carboxyl groups is possibly a requirement to make the FNGPs functionally viable for APA-6 initiation.

#### ACKNOWLEDGEMENTS

This work would not have been possible without the gracious support of the UAB Department of Chemistry, including the use of their facilities. Funding provided by the ALEPSCoR Graduate Research Scholars Program Rounds 7 & 8 was greatly appreciated. Special thanks go to the UAB SEM Laboratory for help with acquiring micrographs.

#### REFERENCES

1. Mermoux M, Chabre Y and Rousseau A. FTIR and  $^{13}\text{C}$  NMR study of graphite oxide, *Carbon* 1991; 29: 469-74.
2. He H, Riedl T, Lerf A and Klinowski J. Solid-State NMR Studies of the Structure of Graphite Oxide, *The Journal of Physical Chemistry* 1996; 100: 19954-8.
3. Lerf A, He H, Riedl T, Forster M and Klinowski J.  $^{13}\text{C}$  and  $^1\text{H}$  MAS NMR studies of graphite oxide and its chemically modified derivatives, *Solid State Ionics* 1997; 101–103, Part 2: 857-62.
4. Staudenmaier L. Verfahren zur Darstellung der Graphitsäure, *Berichte der deutschen chemischen Gesellschaft* 1898; 31: 1481-7.
5. Hummers WS and Offeman RE. Preparation of Graphitic Oxide, *Journal of the American Chemical Society* 1958; 80: 1339-.
6. Marcano DC, Kosynkin DV, Berlin JM, et al. Improved Synthesis of Graphene Oxide, *ACS Nano* 2010; 4: 4806-14.

7. Yan L, Lin M, Zeng C, et al. Electroactive and biocompatible hydroxyl-functionalized graphene by ball milling, *Journal of Materials Chemistry* 2012; 22: 8367-71.
8. Jeon IY, Shin YR, Sohn GJ, et al. Edge-carboxylated graphene nanosheets via ball milling, *Proceedings of the National Academy of Sciences of the United States of America* 2012; 109: 5588-93.
9. Jeon I-Y, Choi H-J, Jung S-M, et al. Large-Scale Production of Edge-Selectively Functionalized Graphene Nanoplatelets via Ball Milling and Their Use as Metal-Free Electrocatalysts for Oxygen Reduction Reaction, *Journal of the American Chemical Society* 2012; 135: 1386-93.
10. Maurice DR and Courtney TH. The physics of mechanical alloying: A first report, *Metall and Mat Trans A* 1990; 21: 289-303.
11. Lu S-Y, Mao Q-J, Peng Z, Li X-D and Yan J-H. Simulation of ball motion and energy transfer in a planetary ball mill, *Chinese Physics B* 2012; 21: 078201.
12. Chattopadhyay PP, Manna I, Talapatra S and Pabi SK. A mathematical analysis of milling mechanics in a planetary ball mill, *Materials Chemistry and Physics* 2001; 68: 85-94.
13. Kwon Y-S, Gerasimov KB and Yoon S-K. Ball temperatures during mechanical alloying in planetary mills, *Journal of Alloys and Compounds* 2002; 346: 276-81.
14. Joardar J, Pabi SK and Murty BS. Estimation of entrapped powder temperature during mechanical alloying, *Scripta Materialia* 2004; 50: 1199-202.
15. Calo JM and Perkins MT. A heterogeneous surface model for the “steady-state” kinetics of the boudouard reaction, *Carbon* 1987; 25: 395-407.
16. Yan D and Yang G. Synthesis and properties of homogeneously dispersed polyamide 6/MWNTs nanocomposites via simultaneous in situ anionic ring-opening polymerization and compatibilization, *Journal of Applied Polymer Science* 2009; 112: 3620-6.
17. Yang M, Gao Y, Li H and Adronov A. Functionalization of multiwalled carbon nanotubes with polyamide 6 by anionic ring-opening polymerization, *Carbon* 2007; 45: 2327-33.
18. Stankovich S, Piner RD, Nguyen ST and Ruoff RS. Synthesis and exfoliation of isocyanate-treated graphene oxide nanoplatelets, *Carbon* 2006; 44: 3342-7.
19. Li Y, Pan D, Chen S, Wang Q, Pan G and Wang T. In situ polymerization and mechanical, thermal properties of polyurethane/graphene oxide/epoxy nanocomposites, *Materials & Design* 2013; 47: 850-6.

20. Gürtler C and Danielmeier K. A catalyst system for the reaction of carboxylic acids with aliphatic isocyanates, *Tetrahedron Letters* 2004; 45: 2515-21.
21. Aida T, Hiramana N and Tsutsumi Y. Thermal Behavior of Carboxylic Acid Functionality in Coal, 1997.
22. Gaur U, Lau Sf, Wunderlich BB and Wunderlich B. Heat Capacity and Other Thermodynamic Properties of Linear Macromolecules. VIII. Polyesters and Polyamides, *Journal of Physical and Chemical Reference Data* 1983; 12: 65-89.
23. Barfknecht P, Pillay SB and Vaidya UK. Effect of nanographite on thermal properties of liquid molded polyamide-6 laminates. In: *19th International Conference on Composite Materials* (eds Hoa SV and Hubert P), Montréal, Canada, July 28, - August, 2, 2013, pp.463-71. Curran Associates, Inc.

## OVERALL CONCLUSIONS

A method to produce multiscale APA-6 laminates enhanced with NGPs was successfully demonstrated. The NGPs did not adversely affect the polymerization reaction, or the mechanical properties of the laminate. The thermal conductivity was marginally enhanced for a 2 wt. % concentration of NGPs. A through-thickness thermal conduction path might not be easily attained using a sprayed-NGP technique, since it creates a thin layer on the interfaces of the fabric. Also, the dispersion of the NGPs into the matrix was not directly addressed. Further study of multi-scale laminates with functionalized nanographite platelets is the next logical step forward.

A successful demonstration of a single-stream *in-situ* polymerization process for APA-6 laminates was achieved by physical placement of initiator chemistry onto the fiber preform. During the infusion process, the initiator washed away from the inlet source leaving an essentially linear gradient in conversion efficiency. Ample opportunity for research exists to solve the initiator washout problem. Refining the behavior of the soluble initiators as well as the method of incorporation could mature the single-stream process into a viable commercial technology.

Surface-initiated polymerization was demonstrated using a specialized silane sizing MOSCL, which contained the APA-6 polymerization moiety. Further research involving other sources of initiator chemistries could enhance the surface-initiation

capability, opening a second market of continuously impregnated precursor materials with exceptional interface properties.

A scalable process of NGOP production from GR flake and carbon dioxide was also modeled and implemented in the design of a planetary ball mill. The mill was used to produce NGOPs that were verified to be functionalized primarily with carboxyl groups. A functionalization reaction of the NGOPs with MDI and  $\epsilon$ -caprolactam was tested. However, the nature of the bond between the isocyanate and the carboxylated NGOPs was undetermined. FNGPs were unable to initiate surface APA-6 polymerization although the presence of the initiator SDI was indirectly verified by FTIR and TGA analyses. Further research with the use of a catalyst could improve the reactivity of the carboxyl groups on the NGOPs.

## FUTURE WORK

### GOAL 1: MECHANICAL CHARACTERIZATION

Further study of the effect of NGPs and FNGPs would be a valid research focus. First, the mechanical properties of NGP/APA-6 nanocomposites could be studied by employing methods to maintain nanoparticle dispersion in the monomer during the polymerization reaction. Either spin-casting or ultrasonic vibration could be used. With the dispersed nanocomposites, additional mechanical and thermal conductivity data could be obtained, and the percolation threshold concentration could also be determined. Additional testing of FNGP/APA-6 nanocomposites could evaluate potential advantages of chemical functionalization. One such possibility is enhanced dispersion of the nanoplatelets caused by the growing polymer chains. Also, mechanical performance might be improved including strength, modulus, and toughness, due to the covalent bond with the matrix. Complete dispersion, however, may suppress enhancement of the thermal conductivity by preventing the NGPs from forming interconnected networks to conduct heat.

### GOAL 2: SINGLE-STREAM PROCESS DEVELOPMENT

The work presented demonstrated the single-stream technology with mixed success. Further research could be conducted to prevent the initiator wash-out problem. For example, a chemical strategy using the blocking capability of isocyanates could be employed. The isocyanate could be temporarily bonded to the fiber by a chemical

species with a de-blocking temperature between 120 °C and 150 °C. The infusion process would occur at a temperature just below the de-blocking temperature of the isocyanate. After the laminate is infused, the temperature rise would cause the isocyanate to become active and diffuse into the monomer matrix. Initiation would then be uniformly distributed thereby producing uniform polymer throughout and effectively eliminating the washout problem.

The single-stream APA-6 processing technique has the potential to create a new processing paradigm for APA-6 composite materials. For example, further development of surface polymerization chemistry could enable continuous impregnation processes at the fiber level to produce precursor products such as tapes, pellets, and woven fabrics. The ability to control the resin content on the fiber level could alleviate a number of melt-processing issues with thermoplastics such as uniform wet-out. In combination with a soluble initiator, a continuous process to create reinforced fabric and unidirectional products could be devised.

### GOAL 3: SCALABLE FNGP PRODUCTION

The beginnings of a complete understanding of the mechanisms at work in a planetary ball-mill process have been modeled. Further basic research is required to fully understand the nature of the impact conditions on the milled material such as the temperature and forces involved. The information would be useful to understand the kinetics of the reaction of graphite with carbon dioxide modeled after the Boudouard reaction. Additionally, the presented research used a common source of graphite flake to negate the requirement of further refined and more expensive purified graphite products. The current work limited the functionalization strategy to one suitable for APA-6

polymerization. With an almost endless list of possible matrices for FNGP nanocomposites, there is an equally viable opportunity to research chemical functionalization schemes derived from NGOPs and other forms of graphite reacted with other materials using the planetary ball-mill process.

## GENERAL REFERENCES

1. Schulze M. CAMISMA - New composites for lighter cars. In: Evonik Industries, (ed.). 2011.
2. Bäck G, Egger P., Berg, L. F. Combining Polymerization and Molding within a Single Machine. *Kunststoffe International*. Kunststoffe international, 2012, p. 102-5.
3. Joyce RM, Ritter, David M. Process for making polymeric materials. United States: DUPont, 1941.
4. Wichterle O. On caprolactam polymerization, *Die Makromolekulare Chemie* 1960; 35: 174-82.
5. Sibal PW, Camargo RE and W. MC. Designing nylon-6 polymerization systems for RIM. In: *2nd International Conference on Reactive Polymer Processing* (eds Pittsburgh, PA, November, Nov. 1982, pp.97-145.
6. Hall HK. Structural Effects on the Polymerization of Lactams, *Journal of the American Chemical Society* 1958; 80: 6404-9.
7. Goettler LA and Neff WJ. Mechanical performance of various nylon 6 composites formed by in-situ polymerization of caprolactam, *Polym Composite* 1986; 7: 383-94.
8. Otaigbe JU and Harland WG. Studies in the properties of nylon 6 glass fiber composites, *Journal of Applied Polymer Science* 1988; 36: 165-75.
9. Otaigbe JU and Harland WG. Impact fracture behavior of continuous glass fiber-reinforced nylon 6, *Journal of Applied Polymer Science* 1989; 37: 77-89.
10. Otaigbe JU. Dynamic Mechanical Response of a Thermoplastic Sheet Molding Compound Glass-Fiber Composite, *Polym Eng Sci* 1991; 31: 104-9.
11. Otaigbe JU. Effect of coupling agent and absorbed moisture on the tensile properties of a thermoplastic RRIM composite, *Journal of Applied Polymer Science* 1992; 45: 1213-21.

12. Van Rijswijk K, Bersee HEN, Jager WF and Picken SJ. Optimisation of anionic polyamide-6 for vacuum infusion of thermoplastic composites: Choice of activator and initiator, *Composites Part A: Applied Science and Manufacturing* 2006; 37: 949-56.
13. Van Rijswijk K, Bersee HEN, Beukers A, Picken SJ and van Geenen AA. Optimisation of anionic polyamide-6 for vacuum infusion of thermoplastic composites: Influence of polymerisation temperature on matrix properties, *Polymer Testing* 2006; 25: 392-404.
14. Van Rijswijk K, Teuwen JJE, Bersee HEN and Beukers A. Textile fiber-reinforced anionic polyamide-6 composites. Part I: The vacuum infusion process, *Composites Part A: Applied Science and Manufacturing* 2009; 40: 1-10.
15. Van Rijswijk K, Lindstedt S and Bersee HEN. Reactively Processed Polyamide-6 Structural Composites for Automotive Applications. In: 2004.
16. Pillay S, Vaidya UK and Janowski GM. Liquid Molding of Carbon Fabric-reinforced Nylon Matrix Composite Laminates, *Journal of Thermoplastic Composite Materials* 2005; 18: 509-27.
17. Stevens MP. *Polymer chemistry : an introduction*. Third ed.: Oxford University Press, 1999, p.
18. Malkin AY, Frolov VG, Ivanova AN and Andrianova ZS. The nonisothermal anionic polymerization of caprolactam, *Polymer Science USSR* 1979; 21: 691-700.
19. Malkin AY, Ivanova SL, Frolov VG, Ivanova AN and Andrianova ZS. Kinetics of anionic polymerization of lactams. (Solution of non-isothermal kinetic problems by the inverse method), *Polymer* 1982; 23: 1791-800.
20. Yang M, Gao Y, Li H and Adronov A. Functionalization of multiwalled carbon nanotubes with polyamide 6 by anionic ring-opening polymerization, *Carbon* 2007; 45: 2327-33.
21. Yan D and Yang G. Synthesis and properties of homogeneously dispersed polyamide 6/MWNTs nanocomposites via simultaneous in situ anionic ring-opening polymerization and compatibilization, *Journal of Applied Polymer Science* 2009; 112: 3620-6.
22. Weng WG, Chen GH and Wu DJ. Crystallization kinetics and melting behaviors of nylon 6/foiliated graphite nanocomposites, *Polymer* 2003; 44: 8119-32.
23. Bansal D, Pillay S and Vaidya U. Nanographite-reinforced carbon/carbon composites, *Carbon* 2013; 55: 233-44.

24. Allport DC, Brenner KS, Chapman JF, et al. Supporting Sciences. In: Allport DC, Gilbert DS and Outterside SM, (eds.). *MDI and TDI: Safety, Health and the Environment: a source book and practical guide*. New York: John Wiley & Sons, Ltd, 2003, pp.277-430.
25. Maurice DR and Courtney TH. The physics of mechanical alloying: A first report, *Metallurgical Transactions A* 1990; 21: 289-303.
26. Lu S-Y, Mao Q-J, Peng Z, Li X-D and Yan J-H. Simulation of ball motion and energy transfer in a planetary ball mill, *Chinese Physics B* 2012; 21: 078201.
27. Chattopadhyay PP, Manna I, Talapatra S and Pabi SK. A mathematical analysis of milling mechanics in a planetary ball mill, *Materials Chemistry and Physics* 2001; 68: 85-94.
28. Jeon IY, Shin YR, Sohn GJ, et al. Edge-carboxylated graphene nanosheets via ball milling, *Proceedings of the National Academy of Sciences of the United States of America* 2012; 109: 5588-93.
29. Gaur U, Lau Sf, Wunderlich BB and Wunderlich B. Heat Capacity and Other Thermodynamic Properties of Linear Macromolecules. VIII. Polyesters and Polyamides, *Journal of Physical and Chemical Reference Data* 1983; 12: 65-89.
30. Jose MV, Steinert BW, Thomas V, et al. Morphology and mechanical properties of Nylon 6/MWNT nanofibers, *Polymer* 2007; 48: 1096-104.
31. ASTM D7264M-07, Standard Test Method for Flexural Properties of Polymer Matrix Composite Materials, ASTM International, West Conshohocken, PA, 2007, [www.astm.org](http://www.astm.org)
32. ASTM D2344 / D2344M - 00e1, Standard Test Method for Short-Beam Strength of Polymer Matrix Composite Materials and Their Laminates, ASTM International, West Conshohocken, PA, 2010, [www.astm.org](http://www.astm.org)
33. Nashif AD, Jones DIG and Henderson JP. *Vibration damping*. New York: Wiley, 1985, 453 p.